MESO-SCALE MODEL FOR SIMULATIONS OF CONCRETE SUBJECTED TO CRYOGENIC TEMPERATURES

A Thesis

by

NOOR AHMAD MASAD

Submitted to the Office of Graduate Studies of
Texas A&M University
in partial fulfillment of the requirements for the degree of

MASTER OF SCIENCE

Chair of Committee,	Dan Zollinger
Committee Members,	Harry Jones
	Mahmoud El-Halwagi
Head of Department,	Robin Autenrieth

August 2013

Major Subject: Civil Engineering

Copyright 2013

ABSTRACT

Liquefied natural gas (LNG) is stored at a cryogenic temperatures ≤ -160°C and around atmospheric pressure to insure the minimum storage volume in tanks. The demand for LNG has been increasing as a primary source of energy. Therefore, there is significant interest in the construction of LNG tanks to achieve low cost and safe storage. Three systems are typically used to store LNG: single containment, double containment, and full containment. Concrete is used in these containment systems, and consequently, understanding concrete behavior and properties at cryogenic temperatures is important.

The research documented in this thesis deals with computational analysis of the behavior of concrete subjected to cryogenic temperatures. The analysis focuses on the effect of aggregate sizes, coefficient of thermal expansion, volume fraction, and the shape of aggregate on damage of concrete subjected to cryogenic temperatures. The analysis is performed by developing a computational model using the finite element software ABAQUS. In this model, concrete is considered as a 3- phase composite material in a meso-scale structure: mortar matrix, aggregate, and interfacial transmission zone (ITZ). The Concrete Damage Plasticity model in ABAQUS is used to represent the mortar and ITZ phases of concrete. This model has the advantage of accounting for the effect of temperature on material properties. The aggregate phase is modeled as a linear-elastic material. The model parameters are selected based on comprehensive literature review of material properties at different temperatures. The finite element results provide very useful insight on the effects of concrete mixture design and properties on

resistance to damage. The most important factor that affected damage development was the difference in the coefficient of thermal expansion between the mortar and aggregates. Models in which the mortar and aggregate had close values of positive coefficients experienced less damage. The model with irregular shape particles experienced more localized damage than the model with circular shape particles. The model was successful in demonstrating the effect of using air entrained concrete in reducing damage. The damage results predicted by the model for air entrained and non-air entrained concrete are validated by comparing them with experimental data from the literature. The analysis validated the capabilities of the mode in simulating the effect of reduction in temperature on damage. The modeling results and the findings from the literature review were used to put forward recommendations regarding the characteristics of concrete used in LNG storage.

DEDICATION

I would like to dedicate this thesis to my parents in Jordan and my brother Eyad (Dr.Masad) for their support and encouragement.

ACKNOWLEDGEMENTS

I would like to thank my committee chair, Professor Dan Zollinger for his guidance and support throughout the course of this research. I also want to thank my committee members, Dr. Harry Jones and Dr. Mahmoud El-Halwagi, for their valuable comments on this thesis. I am grateful for Dr. Rashid Abu Al-Rub for his initial guidance on this study and for introducing me to continuum damage mechanics. I highly appreciate the support that I received from Dr. Sun Myung Kim during the development of the finite element model presented in this thesis.

Thanks also go to my friends and colleagues and the department faculty and staff for making my time at Texas A&M University a great experience. Finally, thanks to my brother Dr. Masad for his encouragement, advice, and fruitful discussions. I thank Dr. John Niedzwecki and the Zachry Department of Civil Engineering for giving me this great opportunity to study in a top-class university. I am proud to be the third female Aggie in my family.

TABLE OF CONTENTS

Page

Page

LIST OF FIGURES

FIGURE Page

FIGURE Page

FIGURE Page

FIGURE Page

FIGURE Page

FIGURE Page

FIGURE Page

LIST OF TABLES

TABLE Page

TABLE Page

CHAPTER I

INTRODUCTION

1.1 Background

Liquefied natural gas (LNG) is stored at cryogenic temperatures and around the atmospheric pressure to insure safe and minimum storage volume in tanks. The demand for LNG has been increasing as a primary source of energy, which led to the increase in the construction of LNG tanks. The economical and safe storage of LNG in concrete tanks would decrease the cost of the construction of these tanks which would impact positively the economy of the gas producing companies and countries.

A typical LNG tank utilizes 9% Ni steel walls and floor for the inner containment tank; this construction method and materials are expensive. An alternative construction method that is currently being considered utilizes concrete walls with normal carbon steel liners or concrete alone without the steel liner.

In an LNG tank system, the concrete inner containment is in direct contact with LNG. There is a critical need to understand concrete behavior at cryogenic temperatures ($T \leq -160°C$) because the properties of concrete materials and mixture design influence the values of internal stresses in concrete which could be responsible for crack development.

The concrete mechanical properties change with a decrease in temperature. For example, tensile strength, compressive strength, and modulus of elasticity increase with a decrease in temperature.

1.2 Problem Statement

Concrete is the most widely used construction material in the world. Concrete is a composite material that consists primarily of cement, coarse aggregate, fine aggregate, and water. Concrete mechanical properties and durability have been studied extensively under ambient temperatures. However, there are limited studies on concrete behavior subjected to cryogenic temperatures. More specifically, there are no studies that evaluate the internal damage of concrete, based on computational modeling, subjected to these low cryogenic temperatures. The need for such studies has increased because of the demand for the safe use of concrete in containment of LNG.

The primary objective of this study is the development of a computational, meso-scale model to characterize and understand the potential damage growth in concrete at cryogenic temperatures down to -160°C. The analysis includes the effect of aggregate sizes, volume faction of aggregates, aggregate shape, and CTEs of mortar and aggregate on concrete damage. The analysis involves the use of meso-scale models that include either idealized, circular aggregate particles or irregular shape aggregate particles.

1.3 Scope and Objectives

The primary objectives of this thesis are to:

1. Develop a meso-scale, computational model for concrete subjected to cryogenic temperatures. In this model, concrete is considered as a three-phase composite material that consists of mortar (or matrix), aggregate, and interfacial transmission zone (ITZ). The Concrete Damaged Plasticity model in ABAQUS

is used to represent the mortar and ITZ phases of concrete. This model accounts for the effect of temperature on the materials properties. The aggregate phase is modeled as a linear-elastic material.

2. Use the computational model to study the effect of aggregate sizes, aggregate volume fraction, aggregate shape, and CTEs of mortar and aggregate values on concrete damage.

The above objectives are achieved through the following tasks:

1. Conduct a comprehensive literature review on construction of LNG tanks, concrete behavior and properties at cryogenic temperatures, and the development of computational models to study the damage behavior of concrete under mechanical and thermal loads.
2. Determine the mechanical properties of concrete phases as functions of temperatures based on comprehensive literature search.
3. Develop a computational, meso-scale model in the finite element package ABAQUS. This model considers concrete as a three-phase composite material: ITZ, aggregate, and mortar. The model is developed to have different aggregate volume fractions of aggregates, different aggregate sizes, and different coefficient of thermal expansion of the phases. The aggregates are initially modeled as idealized, circular shape particles.
4. Expand the meso-scale model to represent the actual geometry of the internal structure of concrete. This model is used to evaluate the effect of CTE on concrete damage and stress distributions within the internal structure.

Consequently, the analysis results are used to compare different concrete materials and better understand the effect of material properties on damage.

5. Validate the model by comparing the damage results from the model with experimental results published in the literature about damage of concrete specimens subjected to freezing.

1.4 Thesis Organization

The thesis is organized in five chapters. **Chapter I** provide a brief background of the problem under consideration, research needs, objectives of this study, and research tasks. **Chapter II** includes the literature review which discusses construction of LNG storage tanks, concrete performance under cryogenic temperatures, and computational modeling of concrete. **Chapter III** presents the development of the computational model: generation of meso-scale model geometry, constitutive models, boundary conditions, and determination of model parameters. **Chapter IV** includes the results of the sensitivity analysis of idealized meso-scale model. This model involves the use of circular shape particles as representatives of aggregates. The analysis focuses on the effects of volume fraction of aggregates, aggregate size distribution, and coefficient of thermal expansion on damage, yielding, and stress distribution. **Chapter V** expands on the development of the meso-scale model by using a concrete internal structure in the meso-scale model. In addition, this chapter presents validation of the model by comparing the damage results from the model with experimental results from the literature for air entrained and non-air entrained concrete specimens. **Chapter VI**

provides the main conclusions from this study with a focus on design factors that reduce concrete damage and it also provided recommendations for future research.

CHAPTER II

LITERATURE REVIEW

2.1 Storage Tanks of Liquefied Natural Gas (LNG)

The Liquefied natural gas (LNG) is as primary source of energy. The gas is stored at cryogenic temperatures equal to or less than -160°C in order for the storage and transportation of natural gas in its liquid form to be safe with minimum possibility of explosion danger.

There are three typical systems of the construction of LNG tanks: (a) single containment which consists of a single wall-roof structure; this type has the lowest construction cost but the highest risk of failure because there is no secondary containment in case of gas leak (see Figure 2.1(a)), (b) double containment which consists of a single roof system and two distinct wall systems, and (c) full containment which consists of double walls and a roof system (See Figure 2.1(b)); this system is considered the safest but it has the highest construction cost (Krstulovic-Opara, 2007). The concrete outer tank is used to protect the inner tank from external loading and to increase the safety in case of failure in the inner tank. Failure could happen because of the propagation of micro-cracks in concrete containment walls.

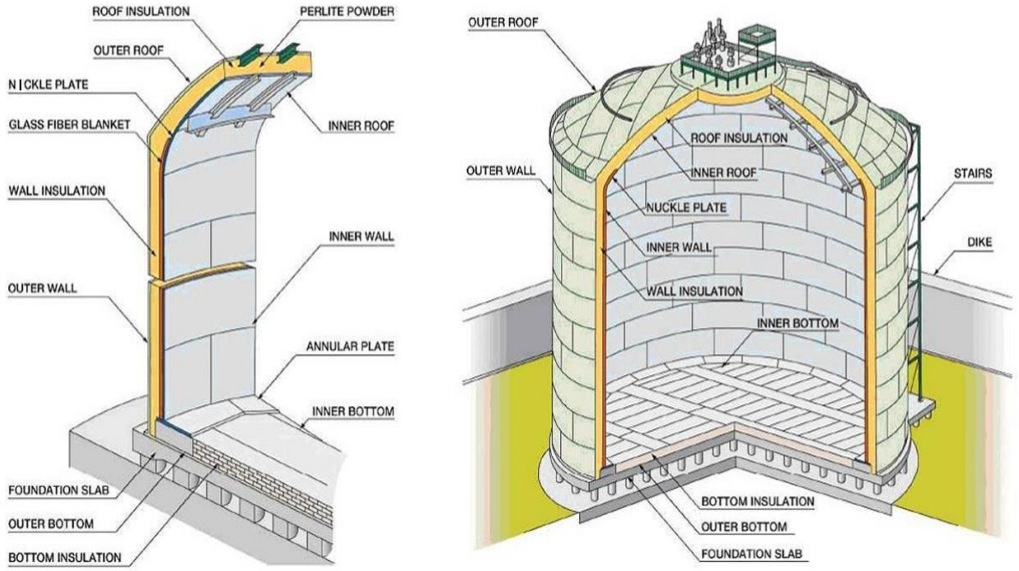

(a)

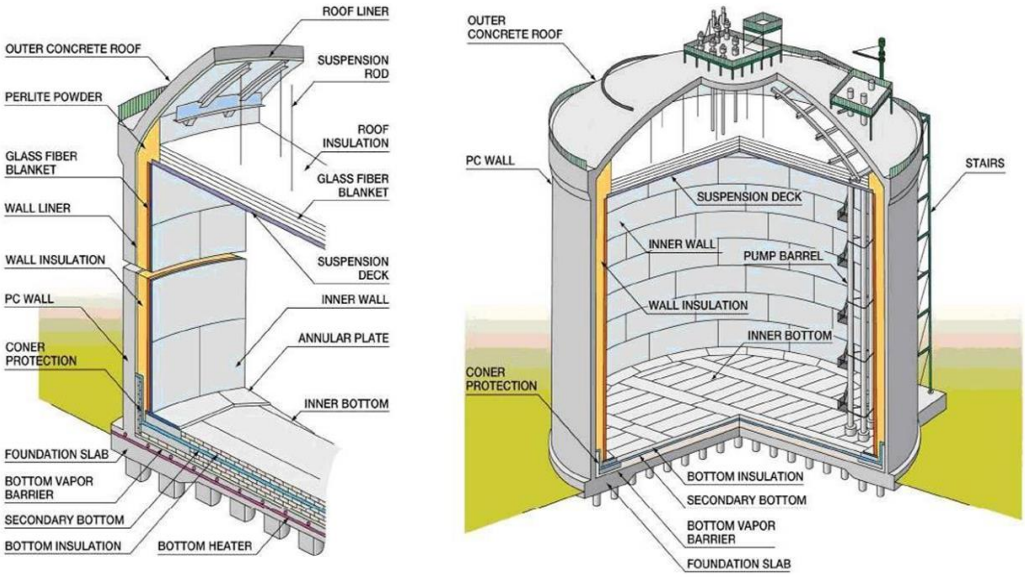

(b)

Figure 2.1 LNG tank: (a) single containment tank and (b) full containment tank (GIIGNL, 2009).

There are several factors that affect the behavior of LNG storage tanks. The interaction between the aggregate and mortar (matrix) phases is an important factor because these two phases have different mechanical and thermal properties that could lead to possible separation or damage at the interface when subjected to cryogenic temperatures. The use of concrete in the construction of LNG primary tank wall and roof construction requires fundamental knowledge of material properties and structural behavior of concrete. van Breugel (1982) reported that the lack of understanding of the behavior of LNG tanks and the loads that are subjected to have led to the use of very high design safety factors.

2.2 Concrete Performance Under Cryogenic Temperatures

Concrete is considered a suitable material to construct the LNG tanks because its mechanical properties improve under cryogenic temperatures (Krstulovic-Opara, 2007). For example, tensile strength, compressive strength, Poisson's ratio, and stiffness increase while creep decrease with a decrease in temperature (See Figures 2.2-2.5). This is caused primarily by the freezing of water form load-bearing ice in the concrete pores (Miura, 1989).

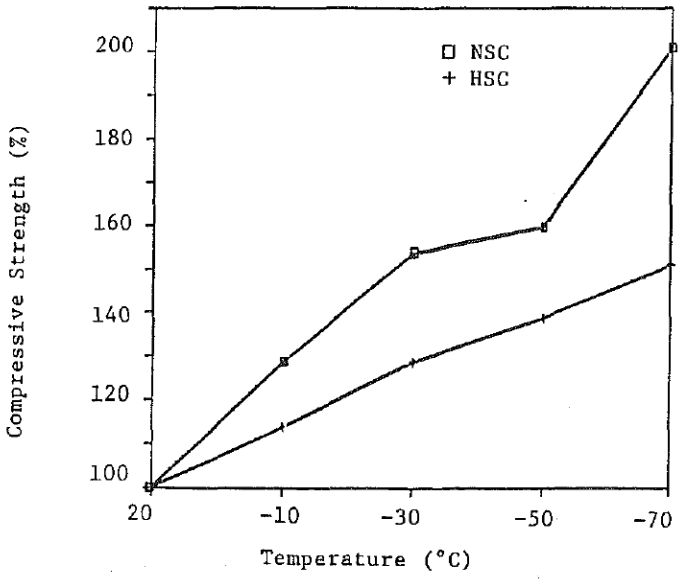

Figure 2.2 The effect of low temperatures on compressive strength ratio % of normal concrete and high concrete strength (Lee, et al., 1988).

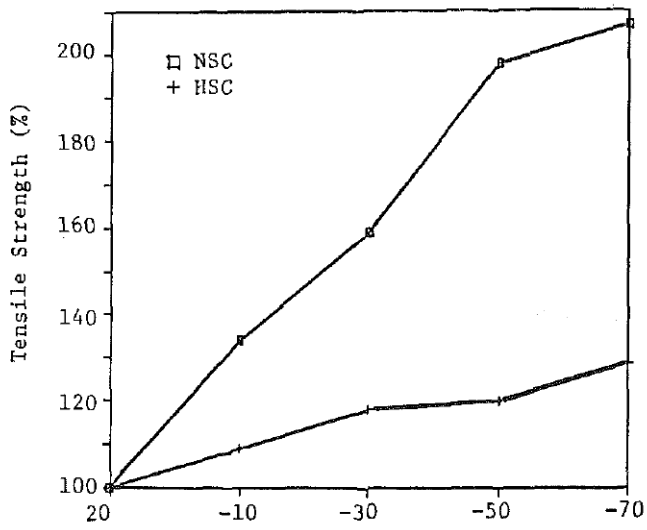

Figure 2.3 The effect of low temperatures on tensile strength ratio % of normal concrete and high concrete strength (Lee, et al., 1988).

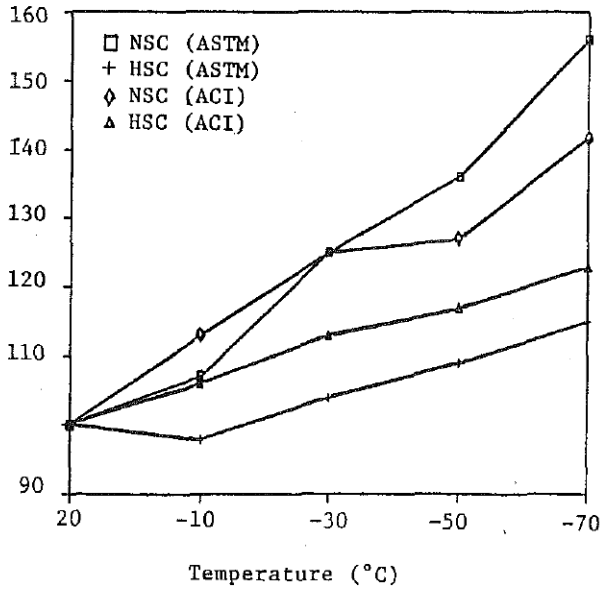

Figure 2.4 The effect of low temperatures on Young's Modulus ratio % of normal concrete and high concrete strength (Lee, et al., 1988).

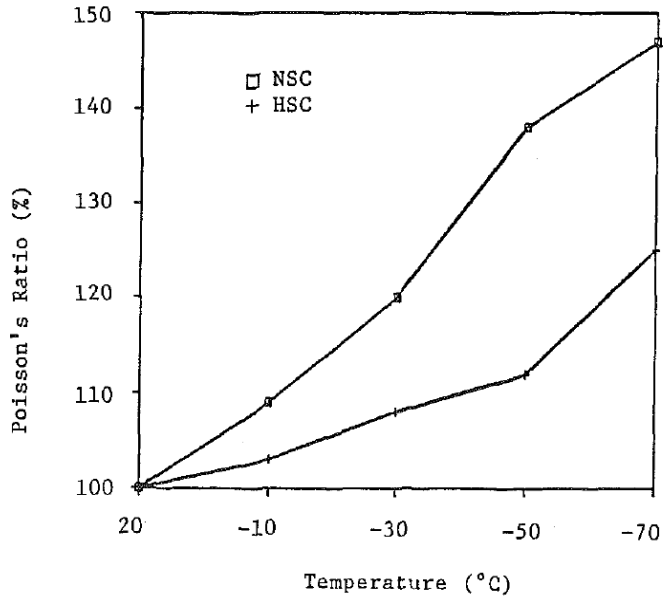

Figure 2.5 The effect of low temperatures on Poisson's ratio % of normal concrete and high concrete strength (Lee, et al., 1988).

As discussed earlier, the primary containment tanks are constructed from concrete and 9 % Ni steel in order to increase the ductility of the containment (van Breugel, 1982). The use of concrete only for primary containment would decrease the construction cost because Ni steel is an expensive. However, there should be clear requirements for exposing concrete for the cryogenic temperatures because of the effects on mechanical and thermal properties (Krstulovic-Opara, 2007). For example, the CTEs of matrix and aggregate are different which causes internal stresses at the interfacial transition zone (ITZ). These stresses develop micro-cracks and could lead to failure in concrete structure. These internal stresses depend on material properties such as temperature, moisture content, and cooling rate (Miura, 1989).

Since concrete becomes more brittle as temperature decreases, it is important to fully understand the effect of CTE on concrete damage growth. The CTE value decreases with a decrease in temperature (Krstulovic-Opara, 2007). The CTE value depends on different factors such as aggregate type and the aggregate content of the concrete. In order to improve resistance to cracking, it is preferred that the concrete has a low CTE and a high tensile strain capacity (Kogbara, et al., 2013).

Moisture content has an effect on concrete strength at low temperatures; strength increases with an increase in moisture content because of the frozen water in pores (Rostasy, et al., 1979). The volume expansion of concrete as a result of ice filling the pores causes tensile stresses that may exceed the bond strength leading to cracks and failure. The stress-strain behavior of concrete changes because the concrete stiffness decreases due to micro-cracking (Miura, 1989). The pore size distribution is an

important factor that influences the formation of ice and its ability to expand, and consequently, it affects the development of internal stresses in concrete as results of freezing water (Kogbara, et al., 2013).

Moisture content has a major effect on the CTE of concrete under cryogenic temperatures (see Figure 2.6). Figure 2.6 shows that the CTE of dry concrete decreases linearly with a decrease in temperature. The CTE decreases and then increases with a decrease in temperature for wet concrete.

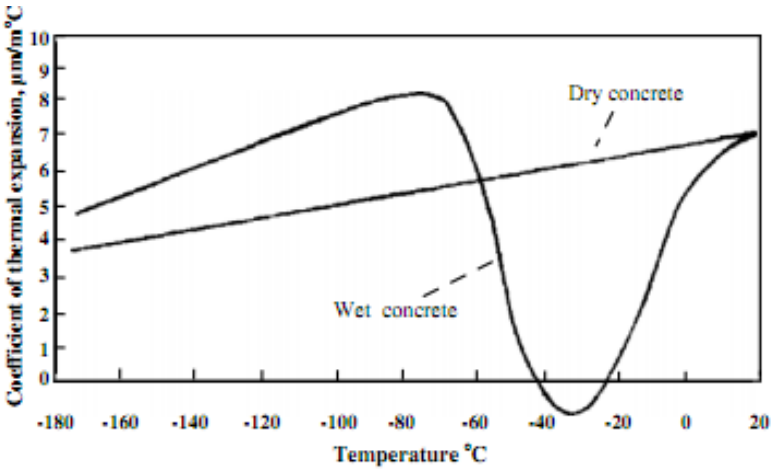

Figure 2.6 Coefficient of thermal expansion of dry/wet concrete versus cryogenic temperatures (Marshall, 1982).

The air-entrained concrete has the ability to resist freezing-thawing cycles; therefore, it is recommended to be used in applications that need frost resistance. Air entrained concrete has air pores that can handle and relief the pressure due to ice

formulation, however, the ice growth in non-air entrained concrete causes expand in cracks which lead to deterioration of concrete after many freeze-thaw cycles.

2.3 Concrete Plasticity Damage Models

Concrete is a heterogeneous material that consists of aggregates, water, cement, and air voids. According to (Wittmann, 1987) concrete can be represented in three simulation scale levels. The macro scale level at which concrete is considered as a homogenous material because the internal structure concrete is ignored; the meso scale level at this level concrete is considered as heterogeneous material which is suitable for simulation the mechanical behavior of concrete. The meso-scale model considers the properties of the various phases and the interactions among these phases. The micro scale level deals with the crystal structure of matrix and the contact zone (interfacial transmission zone) (see Figure 2.7). The work in this thesis is based on the simulation of concrete at the meso-scale.

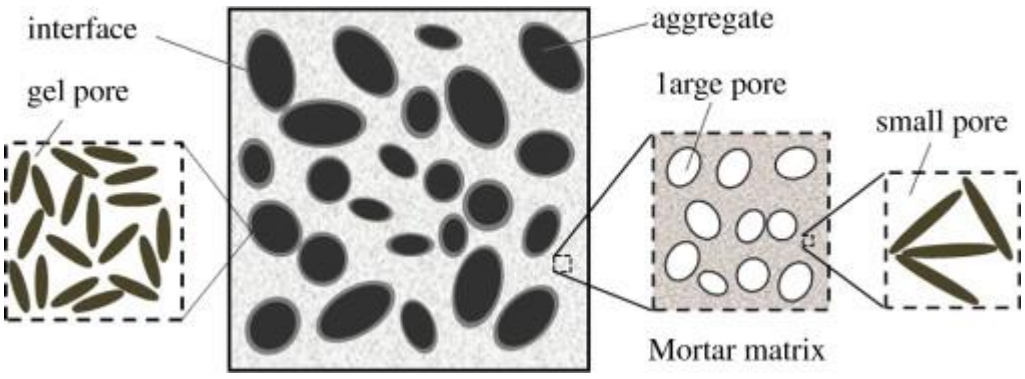

Figure 2.7 The phases of concrete material (Du, et al., 2013).

The description of the concrete damage model presented in this chapter is based on the work of Kim (2010) and the documentation in the ABAQUS theory manual (ABAQUS, 2008). The concrete damaged plasticity model implemented in ABAQUS is used to describe the complex mechanical behavior of concrete. This model is based on continuum mechanics and combines the characteristics of plasticity theory (irreversible deformation) and damage (stiffness degradation). Plasticity-based models alone do not consider the degradation in stiffness due to micro-cracking and micro-voids that would develop in concrete under loading. On the other hand, damage theories are limited in accounting for the nonlinear behavior of concrete (Cicekli, et al., 2007). The degradation in stiffness because of damage can be defined in continuum damage mechanics by the relation between nominal and effective stresses (Lee and Fenves, 1998).

The combine plasticity and damage mechanics model developed by (Yazdani and Schreyer, 1990) distinguishes between a damage surface and a plasticity surface. The damage surface is pressure dependent and considers softening behavior, while the hardening behavior is considered in the plasticity Von Mises surface.

Abu Al-Rub and Kim (2010) modified the coupled plasticity-damage model developed by Cicekli, et.al. (2007) and used it to analyze the meso-scale behavior of concrete. The model considers the plastic behavior of concrete in the effective configuration (Lee and Fenves, 1998), and it uses a the power damage law. The numerical algorithmic model of the coupled plasticity-damage model is coded in the UMAT user material subroutine and implemented in the finite element software

ABAQUS. The detailed numerical algorithms is developed and presented by Abu Al-Rub and Kim (2010).

2.3.1 Damage Model

The damage in a material is represented as micro cracks and opening. The damage density φ is defined as the ratio of the total damage area A^D over the area of whole cross section of the material A (Kachanov, 1958). Damage density ranges from zero for the undamaged material to one for fully damage material. The effective stress in the material reaches the ultimate strength if the material is fully damaged. Damage φ is defined as the ratio of the damaged cross section to the total cross section as shown in Eq. (2.1).

$$\varphi = \frac{A^D}{A} \qquad 0 \le \varphi \le 1 \tag{2.1}$$

In continuum damage mechanics (CDM), there are two types of stresses. The effective stress $\bar{\sigma}_{ij}$ is the force divided by the undamaged part of the area cross section and the nominal stress σ_{ij} is the force divided the total area of the cross section. The relation for the isotropic elastic damage case between the nominal stress and the effective stress is as follows (Kachanov, 1958):

$$\sigma_{ij} = (1-\varphi)\bar{\sigma}_{ij} \tag{2.2}$$

when the cracks propagate in concrete under uniaxial loading the effective stress $\bar{\sigma}_{ij}$ increases because of the reduction occurs in the undamaged area carrying the load.

The relationship between the damaged and the undamaged configurations is based on strain equivalent hypothesis that presented by Lemaitre and Chaboche (1978).

This theory assumes that the strain in the damage state configuration under total stress is equivalent to strain in the fictitious undamaged state configuration under the effective stress. The total strain is decomposed into elastic and plastic strain using incremental theory of plasticity (see Figure 2.8).

$$\varepsilon_{ij} = \varepsilon_{ij}^{\ e} + \varepsilon_{ij}^{\ p} = \bar{\varepsilon}_{ij} = \bar{\varepsilon}_{ij}^{\ e} + \bar{\varepsilon}_{ij}^{\ p} \tag{2.3}$$

where ε_{ij} is the total strain tensor, $\bar{\varepsilon}_{ij}$ is the effective strain tensor, and $\varepsilon_{ij}^{\ e}$, $\varepsilon_{ij}^{\ p}$ are the elastic and plastic strain tensors respectively.

Using strain equivalent hypothesis, the relation between the damage elasticity tensor and the effective elasticity tensor is as follow (Lemaitre and Chaboche, 1978):

$$E_{ijkl} = (1 - \varphi)\bar{E}_{ijkl} \tag{2.4}$$

In Figure 2.8 the behavior of concrete under uniaxial tension and compression is presented. Concrete has higher compressive strength than tensile strength; consequently, the tensile yield strength is equal the ultimate strength of concrete and damage starts at this point. The tensile stress-strain curve increases linearly until it reaches the concrete cracking stress then it decreases linearly due to the softening behavior of concrete in tension. In compression, however, concrete yields before it reaches the ultimate compression strength then the concrete compressive plastic behavior expresses stress hardening followed by strain softening (Prakash, et al., 2011). The difficulty of modeling concrete is that its behavior in compression differs than in tension.

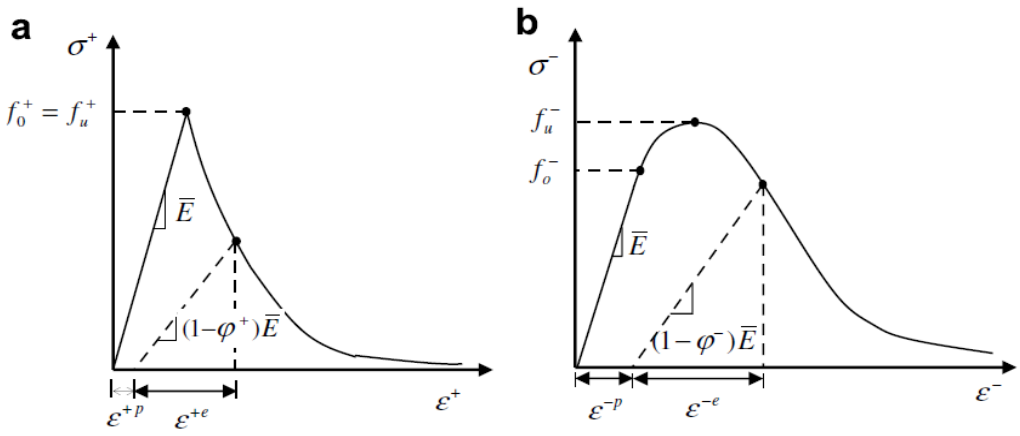

Figure 2.8 The concrete behavior under uniaxial: (a) tension and (b) compression (Cicekli, et al., 2007).

If one considers a nonlinear relation between the damage density and the stiffness density, then the stress relation between normal stress and effective stress in Eq. (2.5) is modified as follow (Cicekli, et al., 2007):

$$\sigma_{ij} = (1-\varphi)^{\alpha}\,\sigma_{ij} \tag{2.5}$$

Where α is a material constant.

2.3.2 Concrete Damaged Plasticity Model in ABAQUS

The concrete damaged plasticity used in ABAQUS is based on the work of Lubliner, et al (1989) and the modification proposed by Lee and Fenves (1998). The failure mechanisms of concrete in this model are tensile cracking and compressive crushing. This model represents the inelastic behavior of concrete based on isotopic damage elasticity and isotopic tension and compression plasticity during fracturing process.

The Abaqus-user should provide the stress-inelastic data and the damage-inelastic data of the uniaxial stress-strain curves shown in Figure 2.8. ABAQUS converts the stress-inelastic data to stress-plastic strain data using Eqs. (2.6 - 2.8).

$$\varepsilon^{+p} = \varepsilon_{cr} - \left(\frac{\varphi^{+}}{1-\varphi^{+}}\right)\left(\frac{\sigma^{+}}{\bar{E}}\right) \tag{2.6}$$

$$\sigma^{+} = \sigma^{+}(\varepsilon^{+p}, \dot{\varepsilon}^{+p}, \theta, f_i) \tag{2.7}$$

$$\sigma^{-} = \sigma^{-}(\varepsilon^{-p}, \dot{\varepsilon}^{-p}, \theta, f_i) \tag{2.8}$$

where ε_{cr} is the cracking strain, ε^{+p}, ε^{-p} are the equivalent plastic strain, $\dot{\varepsilon}^{+p}$, $\dot{\varepsilon}^{-p}$ are the rate of equivalent plastic strain, θ is the temperature, and f_i other predefined value.

The tension and compression plastic strain control the evolution of failure or yield surface. If the calculated effective stress lies within the yield surface then the material still behave elastically.

The stiffness degradation (damage effect) ($E = (1-\varphi)\bar{E}$) is determined from loading-unloading stress strain data. The tension and compression damage variables φ^{+} and φ^{-} are expressed as follows:

$$\varphi^{+} = \varphi^{+}(\varepsilon^{+p}, \theta, f_i) \qquad 0 \le \varphi^{+} \le 1 \tag{2.9}$$

$$\varphi^{-} = \varphi^{-}(\varepsilon^{-p}, \theta, f_i) \qquad 0 \le \varphi^{-} \le 1 \tag{2.10}$$

Lee and Fenves (1998) provided the relation between damaged and undamaged configurations. From the concrete stress-strain relation the nominal stress is shown in Eq. 2.11.:

$$\sigma = E\varepsilon^{e} = E : \left(\varepsilon - \varepsilon^{p}\right) \tag{2.11}$$

According to continuum damage theory, the effective stress $\bar{\sigma}$ is related to the nominal stress σ as in Eq. 2.12.

$$\bar{\sigma} = \boldsymbol{\varphi} : \sigma = \bar{E} : \left(\varepsilon - \varepsilon^{p}\right) \tag{2.12}$$

Using isotropic degradation damage $0 \le \boldsymbol{\varphi} \le 1$, then $\boldsymbol{\varphi} = 1/(1-\varphi)\mathbf{I}$, where $\mathbf{I}$ is fourth order identity tensor. Then, damaged stress and nominal stress are related as in Eq. (2.13).

$$\sigma = \left(1-\varphi\right)\bar{\sigma} \tag{2.13}$$

The concrete damaged plasticity is based on the yield surface that defines the stress level when plastic deformation begins, the changing of hardening properties and loading surface due to plastic flow, and a plastic flow which gives an incremental plastic stress-strain relation with applied loading (Taqieddin, 2008).

The plasticity yield surface implemented in ABAQUS and used in this study is based on the work of Lubliner, et al (1989) and the modification proposed by Lee and Fenves (1998). The Lubliner yield criterion, which is calibrated with uniaxial tension and compression, has the form:

$$\frac{1}{(1-\alpha)}(\bar{q}-3\alpha\bar{p}+\beta(\varepsilon^{p})\left\langle\hat{\bar{\sigma}}_{\max}\right\rangle-\gamma\left\langle-\hat{\bar{\sigma}}_{\max}\right\rangle)-\bar{\sigma}^{-}(\varepsilon^{-p})=0 \tag{2.14}$$

where α , γ , and β are material constants

$$\alpha=\frac{(f_{bo}/f_{o}^{-})-1}{2(f_{bo}/f_{o}^{-})-1} \tag{2.15}$$

$$\gamma=\frac{3(1-K_{c})}{2K_{c}-1} \tag{2.16}$$

$$\beta=(1-\alpha)\frac{\bar{\sigma}^{-}(\varepsilon^{-p})}{\bar{\sigma}^{+}(\varepsilon^{+p})}-(1+\alpha) \tag{2.17}$$

$$\left\langle\hat{\bar{\sigma}}_{\max}\right\rangle=\frac{1}{2}\left(\left|\hat{\bar{\sigma}}_{\max}\right|+\hat{\bar{\sigma}}_{\max}\right) \tag{2.18}$$

The effective pressure $\bar{p}$ is :

$$\bar{p}=-\frac{\bar{\sigma}I}{3} \tag{2.19}$$

The Mises equivalent effective stress is:

$$\bar{q}=\sqrt{\frac{3}{2}(\bar{S}:\bar{S})} \tag{2.20}$$

where the effective stress deviator is $\bar{S}=\bar{\sigma}+\bar{p}\mathbf{I}$

f_{bo}/f_{o}^{-} is the ratio of initial equi-biaxial and uniaxial compressive yield strength. The range for this ratio, based on experimental values, is between 1.1 and 1.16. The yielding value is between 0.08 and 0.12, $\hat{\bar{\sigma}}_{\max}$ is the maximum principal effective stress, and K_{c} is the ratio of second stress invariant on tensile meridian q(TM) to compressive meridian q (CM).

The potential plastic flow in this model is the Drucker-Prager hyperbolic function:

$$G = \sqrt{\left(\mathrm{e} f_{\mathrm{o}}^{+} \tan\psi\right)^2 + \bar{q}^2} - \bar{p}\tan\psi \tag{2.21}$$

where ψ is the dilation angle and e is the flow potential eccentricity.

2.3.3 Plastic Yield Surface

The yield criterion in the effective configuration is expressed as follows (Abu Al-Rub and Kim, 2010):

$$f = \sqrt{3\bar{J}_2} + \alpha\bar{I}_1 + \beta(\varepsilon_{eq}^{+}, \varepsilon_{eq}^{-})\mathrm{H}(\hat{\bar{\sigma}}_{\max})(\hat{\bar{\sigma}}_{\max}) - (1-\alpha)c^{-}(\varepsilon_{eq}^{-}) \le 0 \tag{2.22}$$

Where

$$\beta = (1-\alpha)\frac{c^{-}(\varepsilon^{-p})}{c^{+}(\varepsilon^{+p})} - (1+\alpha) \tag{2.23}$$

$$\bar{J}_2 = \frac{\bar{s}_{ij}\bar{s}_{ij}}{2} \tag{2.24}$$

$$\bar{s}_{ij} = \bar{\sigma}_{ij} - \frac{\bar{\sigma}_{kk}\delta_{ij}}{3} \tag{2.25}$$

$$\bar{I}_1 = \bar{\sigma}_{kk} \tag{2.26}$$

where $\bar{J}_2$ is the second invariant of the effective deviatoic stress tensor, $\bar{s}_{ij}$ is the first invariant of the effective Cauchy stress tensor $\bar{\sigma}_{ij}$, $\hat{\bar{\sigma}}_{\max}$ is the maximum principal effective stress, and the Heaviside step function ($\mathrm{H}(\hat{\bar{\sigma}}_{\max})$: H=1 if $\hat{\bar{\sigma}}_{\max} > 0$ and H=0 if $\hat{\bar{\sigma}}_{\max} < 0$), c^{-} is the compression isotropic hardening function (Abu Al-Rub and Kim, 2010).

In the plasticity-damage model, the concrete is considered as a cohesive frictional material; therefore, the compressive and tensile isotropic hardening functions c^- and c^+ are explained by exponential and linear hardening laws as follows:

$$c^- = f_o^+ + Q^-\left[1-\exp(-b^-\varepsilon^{-p})\right] \tag{2.27}$$

$$c^+ = f_o^+ + h^+\varepsilon^{+p} \tag{2.28}$$

The material constants Q^-, h^+, b^- are obtained from the effective configuration of tension and compression uniaxial stress-strain diagrams.

The loss in concrete strength leads to decrease in its cohesion. If full damage occurs in concrete, this would cause vanish of cohesion.

2.3.4 Tensile and Compressive Damage Surfaces

The damage growth function $g^\pm$ is generalized by Cicekli et al., (2007) and is used in the model by Abu Al-Rub and Kim (2010).

$$g^\pm = \sqrt{\frac{1}{2}Y_{ij}^\pm L_{ijkl}^\pm Y_{kl}^\pm} - K^\pm(\varphi_{eq}^\pm) \le 0 \tag{2.29}$$

Where $K^\pm$ is the tensile and compression damage isotropic hardening function, $L_{ijkl}^\pm$ is fourth order symmetric tensor is taken as the fourth-order identity tensor I_{ijkl}, and $Y_{ij}^\pm$ is the damage driving force can be defined as the energy release rate. The equivalent damage variables $\varphi_{eq}^\pm$ are evaluated using damage consistency conditions.

2.3.5 The Power Evolution Law

The power relationships in Eqs. (2.30) and (2.31) are suitable to predict the concrete damage behavior when it is compared with the experimental data (Kim 2010).

$$\varphi_{eq}^{+} = B^{+}\left(\frac{K_{\mathrm{o}}^{+}}{K^{-}}\right)\left(\frac{K^{+}}{K_{\mathrm{o}}^{+}} - 1\right)^{q^{+}} \tag{2.30}$$

$$\varphi_{eq}^{-} = B^{-}\left(\frac{K^{-}}{K_{\mathrm{o}}^{-}} - 1\right)^{q^{+}} \tag{2.31}$$

where $B^{\pm}$ are material constants and can be identified from uniaxial compressive and tensile stress and strain diagrams. $q^{\pm}$ are power tensile and compressive damage evaluation law constants.

$$B^{\pm} = \left[\frac{G_f^{\pm}\bar{E}}{\ell f_{\mathrm{o}}^{\pm 2}} - \frac{1}{2}\right]^{-1} \geq 0 \tag{2.32}$$

where $G_f^{\pm}$ is fracture energy that is required to open unit area of crack (Hillerborg, et al., 1976), ℓ is the characteristic length scale parameter that usually has a value close to the size of the smallest element in a finite element mesh, $f_{\mathrm{o}}^{\pm}$ is the uniaxial compression and tension yield strength, K_{o}^{+}/K the ratio of the tensile damage threshold to the tensile damage hardening function. $K_{\mathrm{o}}^{\pm}$ is can be interpreted as the area under the linear portion of stress strain diagram

$$K_o^{\pm} = \frac{f_o^{\pm 2}}{2\bar{E}} \tag{2.33}$$

The damage is initiated when the damage hardening function $K^{\pm}$ is greater than the tensile damage threshold $K_{\mathrm{o}}^{\pm}$. The value of K_{o}^{+} is nearly equal to tensile yield strength f_{o}^{+} and K_{o}^{-} is greater than the compressive yield strength f_{o}^{-} because the damage initiated after the material reaches the compressive yield strength.

Kim (2010) used the power damage model to represent the behavior of matrix and ITZ in a concrete meso-scale model. The required parameters for this model are elastic constant υ and E, tensile material constants f_o^+, K_o^+, h^+, q^+, B^+ compressive material constants, f_o^-, K_o^-, b^-, Q^-, q^-, B^- and other constants α and α_P. The plasticity constants which are tensile and compressive hardening moduli, h^+ and Q^-, compressive hardening rate constant b^-, and the damage constants which $B^{\pm}$ and power tensile and compressive damage evaluation law constants $q^{\pm}$.

The calibration for tensile and compressive material constants are based on uniaxial loading and unloading stress-strain test results (Abu Al-Rub and Kim, 2010). The damage young's modulus E can be determinate from the nominal loading – unloading stress – strain curves. Once E is determined, the effective stress can be computed using the relation $\bar{E}/E = \bar{\sigma}/\sigma$. Effective stress – strain diagram can then be established and from this curve the plasticity material constants f_o^-, b^-, Q^-, h^+ can be identified. The damage density can be identified using Eq. (2.34)

$$\varphi = 1 - \sqrt{E / \bar{E}} \tag{2.34}$$

Then the damage constants K_o^-, B^-, q^- .can be evaluated. The same procedure is used to find the tensile material constant. The nominal stress-strain curves that fit the experimental curves are evaluated using power damage evaluation law.

2.4 Summary

The literature review discussed the typical methods used in the construction and containment of LNG storage tanks. It is clear from the literature review that there is a need to better understand the behavior of concrete which is in direct contact with LNG at cryogenic temperatures. More specifically the concrete behavior and potential damage are affected by the coefficient of thermal expansion values of the phases and the design of the concrete mixture.

The coupled plasticity-damage model implemented in ABAQUS and modified by Abu Al-Rub and Kim (2010) is suitable to represent the meso-scale behavior of the mortar and ITZ. This model is calibrated using compressive and tensile uniaxial tests of concrete at different temperatures. The model is capable of representing the nonlinear damage behavior as well as the plastic deformation of concrete. The remaining chapters of this thesis utilize this model to analyze the effects of concrete design and properties of its phases on damage at different temperatures.

CHAPTER III

DEVELOPMENT OF MESO-SCALE MODEL FOR SIMULATION OF CONCRETE SUBJECTED TO CRYOGENIC TEMPERATURES

3.1 Introduction

This chapter describes the development of the meso-scale model used in the simulation of the effect of cryogenic temperatures on concrete behavior. The meso-scale model is developed using the software package ABAQUS. The concrete is considered as a three-phase composite material that consists of aggregate, mortar or matrix and interfacial transmission zone (ITZ). The concrete damage plasticity in ABAQUS is used to represent the mortar and ITZ. This model, which is described in Chapter II, is capable of accounting for permanent deformation, nonlinear damage or reduction in stiffness, and the effect of temperature on material properties. The aggregate particles are modeled as linear elastic. The properties of the three phases are modeled as functions of temperature. The selection of the material properties and their dependence on temperature are based on the published literature. This chapter discusses the approach followed to determine these properties and the boundary conditions (displacement and temperature) used in the development of the meso-scale model.

3.2 Meso-Model Structure and Boundary Conditions

The generation of the representative volume element (RVE) of the meso-scale model starts with predefined size distribution of particles. This distribution can be based on

actual analysis of particles in a mixture or simply assumed for parametric analysis. The next step is to use a code written in MATLAB Generator which developed by Kim (2010) based on the method of Bazant et al. (1990) to develop random computer generator of aggregate. This code is used to find the positions of these particles in the RVE by a generation random geometrical configurations of particles. This code needs the number of aggregates for each particle size and their radii and it outputs the coordinates for the particles in RVE. The output of the MATLAB code is then transformed to AutoCAD to draw the three-phase material. The ITZ is assumed to have a uniform thickness of 0.1mm (Zheng, et al., 2005) around all particles and the remaining medium is considered the mortar or matrix phase. An example of the geometry generated by AutoCAD is shown in (see Figure 3.1(a)).

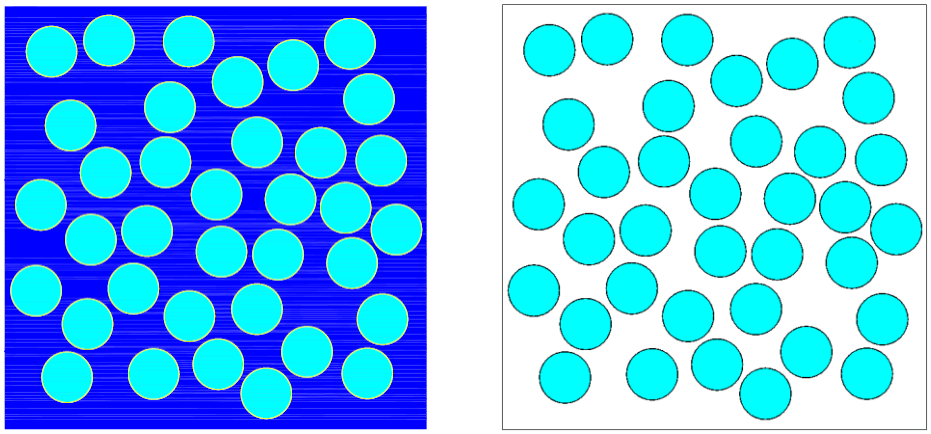

(a) (b)

Figure 3.1 Concrete geometry generated by: (a) AutoCAD and (b) ABAQUS.

The model geometry generated by AutoCAD is then imported to ABAQUS to generate the 2-D meso-scale structure (see Figure 3.1(b)). The finite element model is plane strain, and the element CPE4R, which is four nodes bilinear quadrilateral element in ABAQUS, is used in generating the finite element mesh. The size of the RVE is 100 mm × 100 mm.

The displacement boundary conditions are taken as a roller at the bottom side (restricted movement in the vertical direction and free to move in the horizontal) and the left side (restricted movement in the horizontal direction and free to move in the vertical direction) of the RVE. Figure 3.2 illustrates the model with the boundary conditions. The analysis considers two cases of temperature boundary conditions. In the first case, the whole model is initially subjected to a temperature of 20 ^{o}C and then the temperature is reduced linearly with time to -160 ^{o} C. This case represents a rapid cooling of a concrete specimen, and it is referred to as the "steady state analysis" in this thesis.

The second analysis considers the model to be subjected to 20 ^{o}C on the left side and -160 ^{o}C on the right side. This case represents the temperature gradient that a concrete specimen is subjected to when it is in contact with the LNG in one side and at atmospheric temperature on the other side. This analysis is referred to as the "transient analysis".

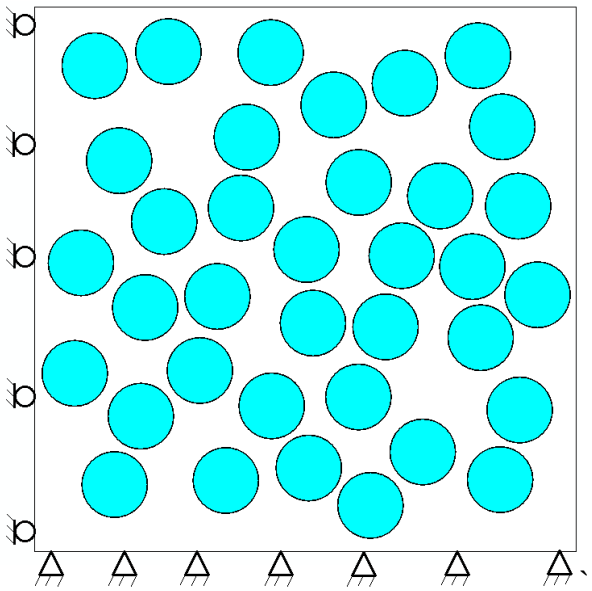

Figure 3.2 The boundary conditions for the meso-scale model.

3.3 Constitutive Models and Material Properties

3.3.1 Aggregates

The aggregate phase is modeled as a linear elastic material. The dependency of the aggregate elastic properties (modulus of elasticity and Poisson's ratio) on temperature is taken based on the data by (Inada, et al., 1997). These properties are shown in Table 3.1.

Table 3.1 Elastic properties for aggregates as a function of temperature.

Aggregate Properties		
Temperature (°C)	Elastic Modulus E (MPa)	Poisson's ratio υ
20	30,000	0.200
0	32,100	0.215
-40	38,199	0.230
-80	43,547	0.250
-120	48,773	0.275
-160	51,211	0.297

3.3.2 Matrix and ITZ

The matrix and ITZ are modeled using the concrete coupled damage plasticity model (ABAQUS 6.8; Abu Al-Rub and Kim 2010). More information about this model is given in Chapter II. The elastic material properties were determined in two steps. In the first step, a typical value for the elastic modulus was assumed to be 26,000 MPa at a temperature of 20 ^{o}C (Yang, et al., 1996). In the second step, the effect of temperature was accounted for by following the trend of experimental measurements reported by (Lee, et al., 1988). It was assumed that the effect of temperature on the mortar follows the same trend as that on concrete.

The tensile strength and compressive strength of mortar at different temperatures were specified following the data reported by Lee, et al, (1988) and Neven Krstulovic-Opara (2007) (See Tables 3.2 -3.3).

Table 3.2 Matrix properties as a function of temperature**.**

Temperature (°C)	Poisson's ratio υ	Tensile yield strength (MPa)	Compressive yield strength (MPa)	Elastic Modulus E (MPa)
20	0.220	3.00	42	26000
0	0.231	3.75	50	27750
-40	0.280	5.50	65	33000
-80	0.330	6.40	85	37500
-120	0.339	6.51	87	42120
-160	0.350	6.60	90	44200

Table 3.3 ITZ properties as a function of temperature.

Temperature (°C)	Poisson's ratio υ	Tensile yield strength (MPa)	Compressive yield strength (MPa)	Elastic Modulus E (MPa)
20	0.220	3.00	42	23400
0	0.231	3.75	50	24975
-40	0.280	5.50	65	29700
-80	0.330	6.40	85	33750
-120	0.339	6.51	87	37908
-160	0.350	6.60	90	39780

The damage behavior under tensile stresses was determined at each temperature according to the following steps:

1. The model by Abu Al-Rub and Kim (2010) was run in ABAQUS using the elastic properties, tensile strength and compressive strength at a given temperature along with a set of damage parameter B^+ and the plasticity parameter h^+ in Eq.(3.1) and Eq.(3.2) (same as Eq. (2.27) and Eq.(2.31) in Chapter II).

$$c^+ = f_o^+ + h^+ \varepsilon^{+p} \tag{3.1}$$

$$\varphi_{eq}^+ = B^+ \left(\frac{K_o^+}{K^-} \right) \left(\frac{K^+}{K_o^+} - 1 \right)^{q^+} \tag{3.2}$$

The tensile yield stress of concrete subjected to cryogenic temperature decreases, therefore, the damage parameter B^+ and the plasticity parameter h^+ are assumed in order to describe this behavior (See Table 3.4).

Table 3.4 Damage and plasticity parameters for matrix and ITZ as a function of temperature Type A.

Temperature (°C)	B^+	h^+(MPa)
20	1.2	10,000
0	1.3	10,000
-40	1.5	10,000
-80	1.6	10,000
-120	1.55	10,000
-160	1.5	10,000

These parameters were varied to generate different stress-strain and damage-strain curves as shown in Figures 3.3 and 3.4. An example of the set of parameters that were determined at 20 ^{o}C are shown in Table 3.5.

Table 3.5 The material parameters for matrix and ITZ in meso-scale simulations based on Abu Al-Rub and Kim (2010) model.

Constants			Matrix	
Elastic Constants	$\bar{E}$ (MPa)		26000	
	υ		0.22	
Tensile Material Constants	f_o^+ (MPa)		3.0	
	K_o^+ (MPa)		3.0	
	h^+ (MPa)		10,000	
	B^+		1.20	
	q^+		1.10	
Compressive Material Constants	f_o^- (MPa)		15.0	
	K_o^- (MPa)		20.0	
	Q^- (MPa)		80.0	
	b^-		820.0	
	B^-		0.15	
	q^-		1.40	
Yield Criteria	α	0.12	α_P	0.2

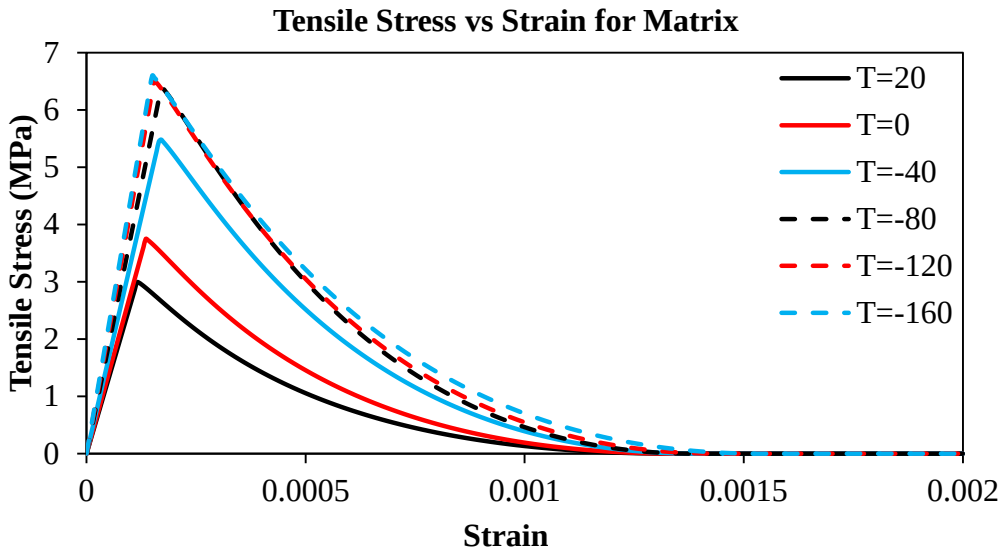

(a)

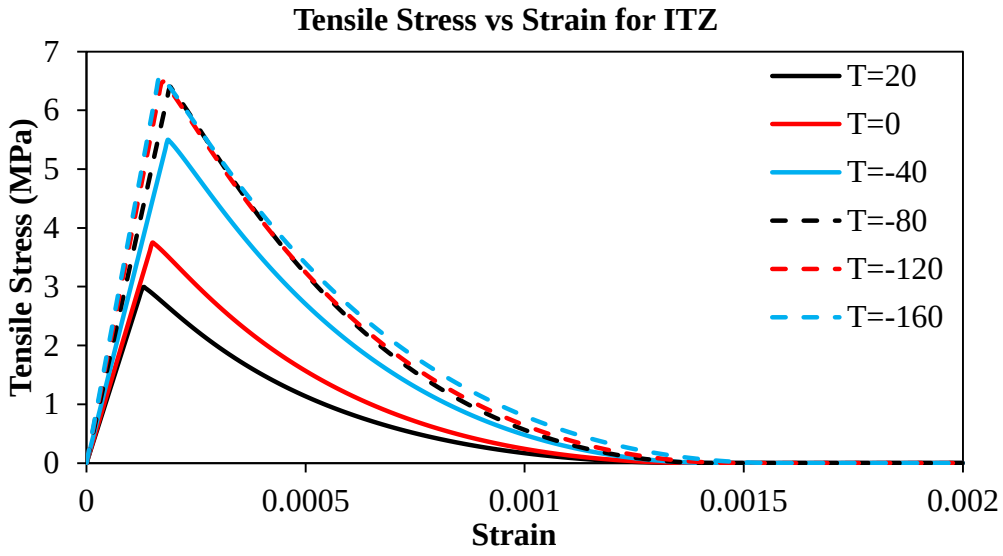

(b)

Figure 3.3 Tensile stress-strain relations at different temperature values for: (a) matrix and (b) ITZ (Type A).

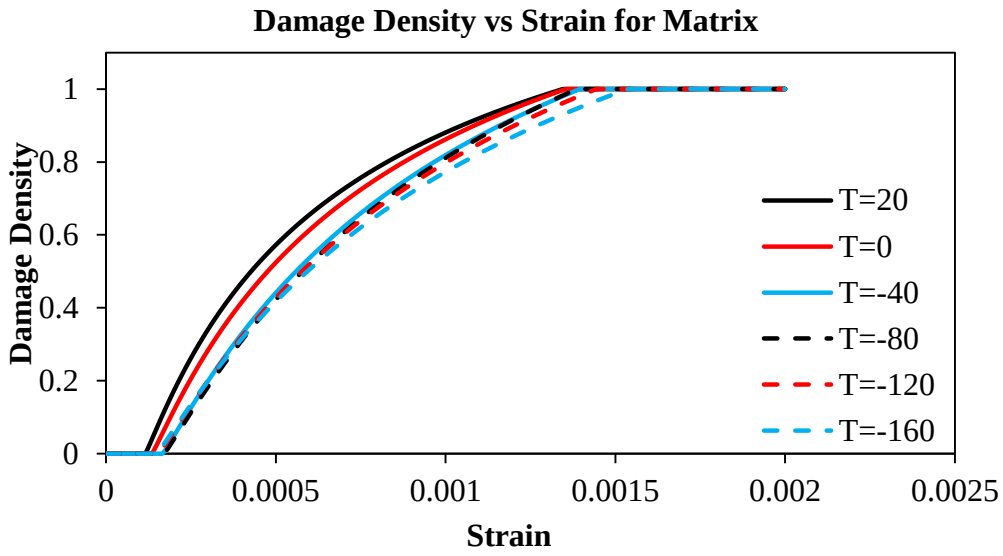

(a)

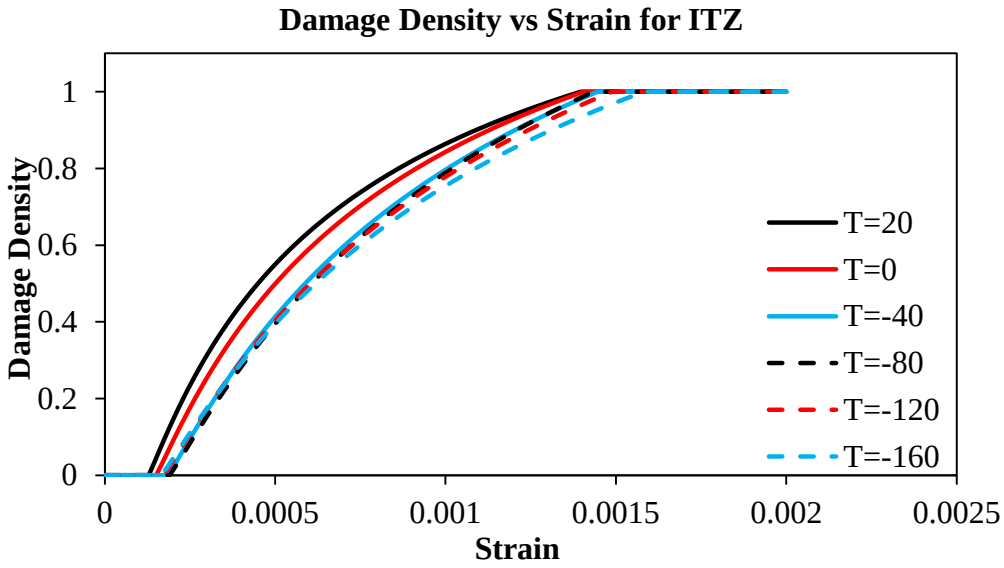

(b)

Figure 3.4 Damage density-strain relations at different temperature values for: (a) matrix and (b) ITZ (Type A).

2. The parameters that are needed for the plasticity model Eqs. (3.1) and (3.2) were selected to represent normal strength concrete as reported by Kim (2010).
3. Then concrete damage model in ABAQUS requires inputting two relationships: stress versus cracking strain (see Figure 3.5) and damage density versus cracking strain (see Figure 3.6).

   The cracking strain is expressed as follows:

$$\varepsilon_{cr} = \varepsilon - \frac{\sigma_y}{\varepsilon_y} \tag{3.3}$$

   Where ε_{cr} is the cracking strain for each point in tensile stress-strain curves, where ε is the strain at the point, σ_y is the initial yield stress value of the curve, and ε_y is yield strain at the initial yield stress. The stress is plotted against the cracking strain as shown in Eq. (3.3). The model by Abu Al-Rub and Kim (2010) outputs the damage density versus strain, which is converted to damage density versus cracking strain. In order to define the flow potential, yield surface, and viscosity, the parameters of concrete damaged plasticity model in Table 3.6 are required.

Table 3.6 The Concrete Damaged Plasticity model parameters.

Concrete Damaged Plasticity parameters	Values
ψ , Dilation angle	45°
e, Flow Potential Eccentricity	0.1
f_{bo}/f_{o}^{-}	1.16
K_c	2/3
μ , Viscosity Parameter (°C)	0.0

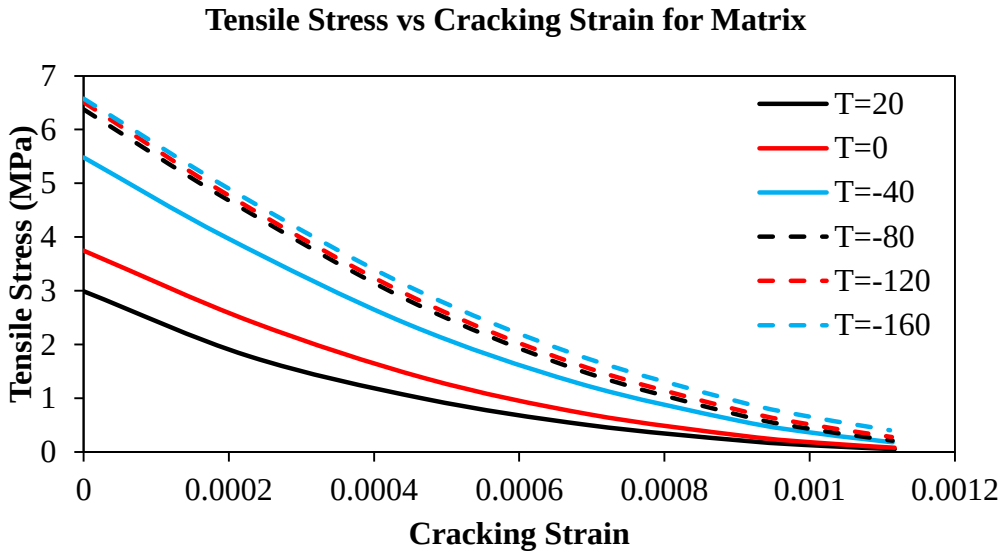

(a)

Figure 3.5 Tensile stress-cracking strain relations at different temperature values for: (a) matrix and (b) ITZ (Type A).

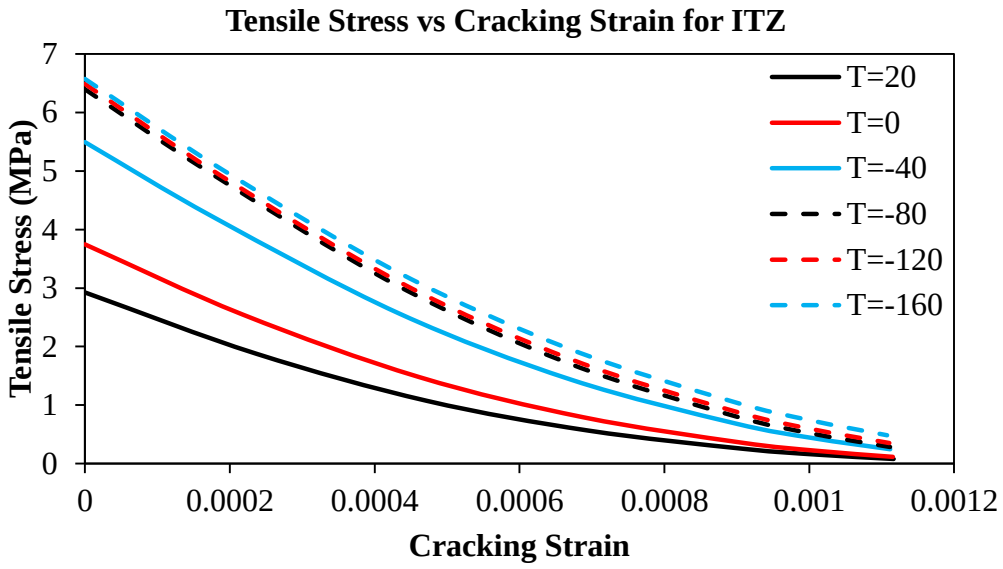

(b)

Figure 3.5 Continued.

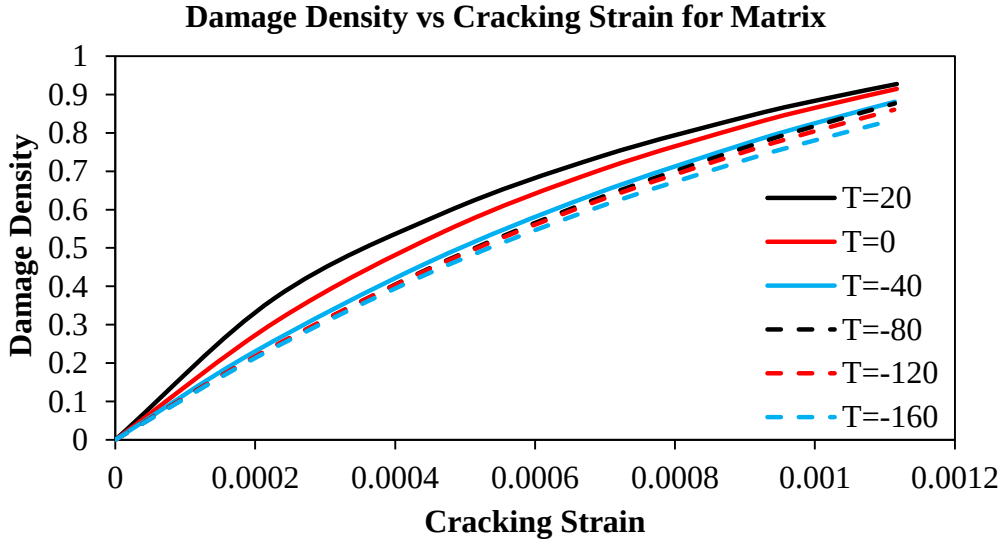

(a)

Figure 3.6 Damage density-cracking strain relations at different temperature values for: (a) matrix and (b) ITZ (Type A).

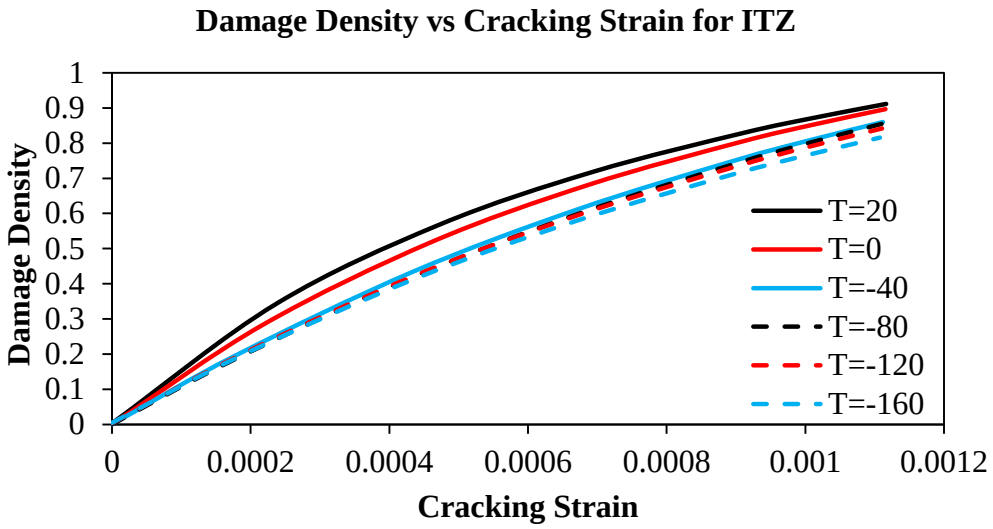

(b)

Figure 3.6 Continued.

4. The values from the two relationships determined in the previous step are used as input in the concrete damaged plasticity model in tabulated format at each temperature. The concrete damage plasticity model was run for one element to generate stress-strain curves in tension (see Figures 3.3- 3.4) that match the original curves that were produced using the model by Abu Al-Rub and Kim (2010).

There are no direct measurements in the literature on the material properties of ITZ and its dependence on temperature. Therefore, material properties for the ITZ are assumed to be the same as the properties of the matrix but the modulus of elasticity of the ITZ is taken as 0.9 of the modulus of elasticity of the matrix. The matrix and ITZ properties used in the model are shown in Tables 3.2 and 3.3 respectively.

In order to study the effect of the tensile damage on the concrete behavior, two sets of tensile stress-strain curves were generated and used in the analysis. The main difference between the curves is how quickly matrix and ITZ damage densities reach full damage (i.e. damage density = 1). The first set of curves is shown in Figures 3.3-3.6 and is referred to as Type A damage, and the second type of curves is shown in Figures 3.7-3.10 and is referred to as Type B damage. These two sets of curves where generated by changing the damage and plasticity parameters B^+ and h^+ (See Table 3.7).

Table 3.7 Damage and plasticity parameters for matrix and ITZ as a function of temperature Type B.

Temperature (°C)	B^+	h^+(MPa)
20	1.2	10,000
0	1.3	9,000
-40	1.5	7,000
-80	1.6	6,500
-120	1.55	6,000
-160	1.5	6,000

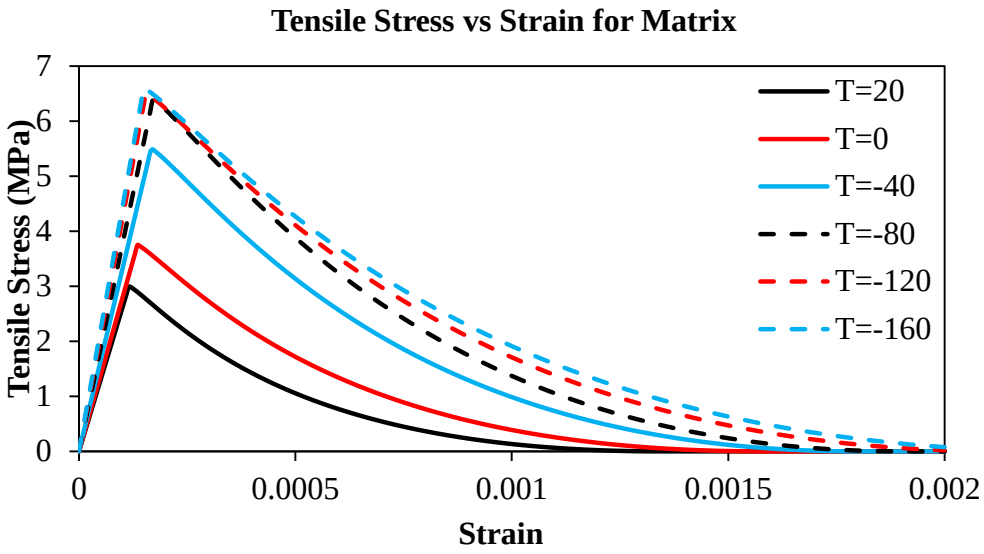

(a)

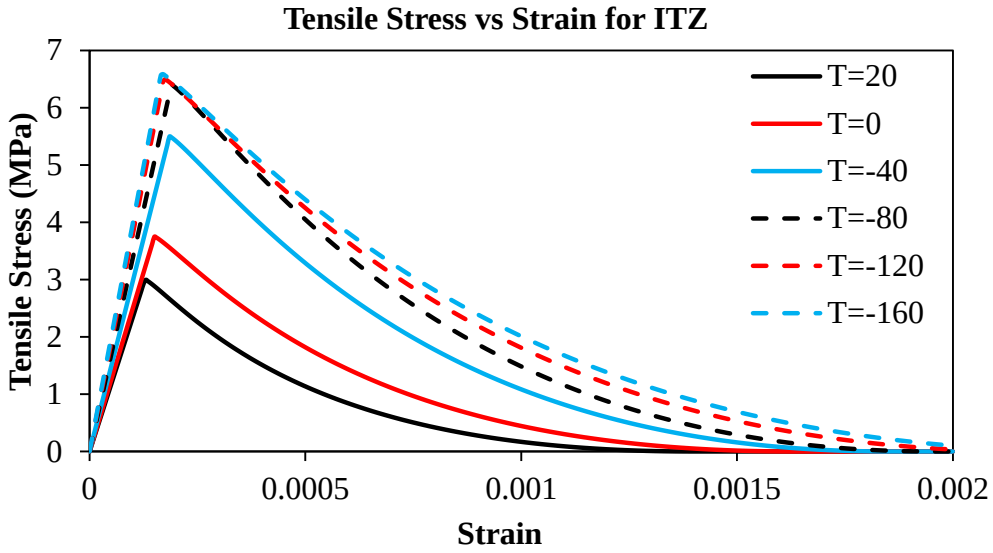

(b)

Figure 3.7 Tensile stress-strain relations at different temperature values for: (a) matrix and (b) ITZ (Type B).

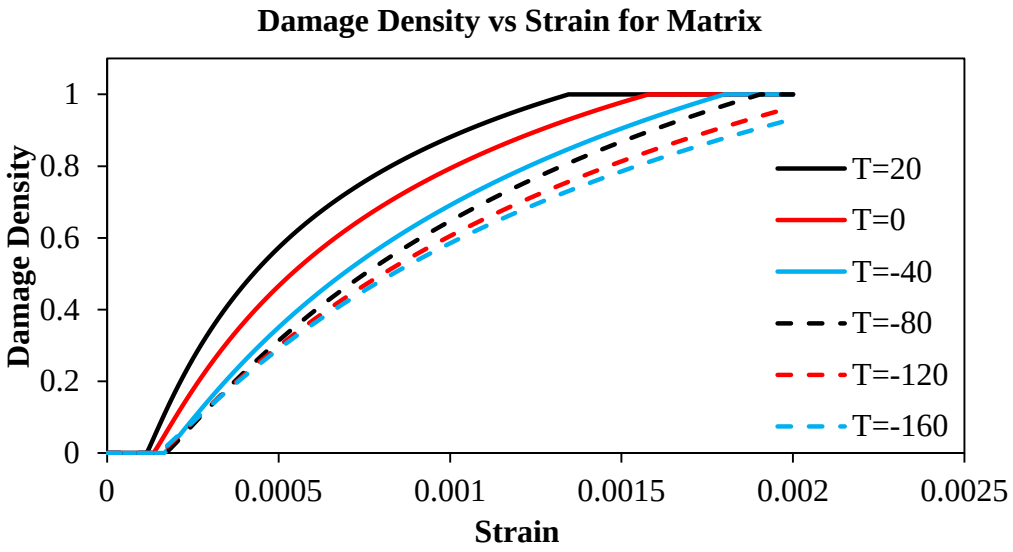

(a)

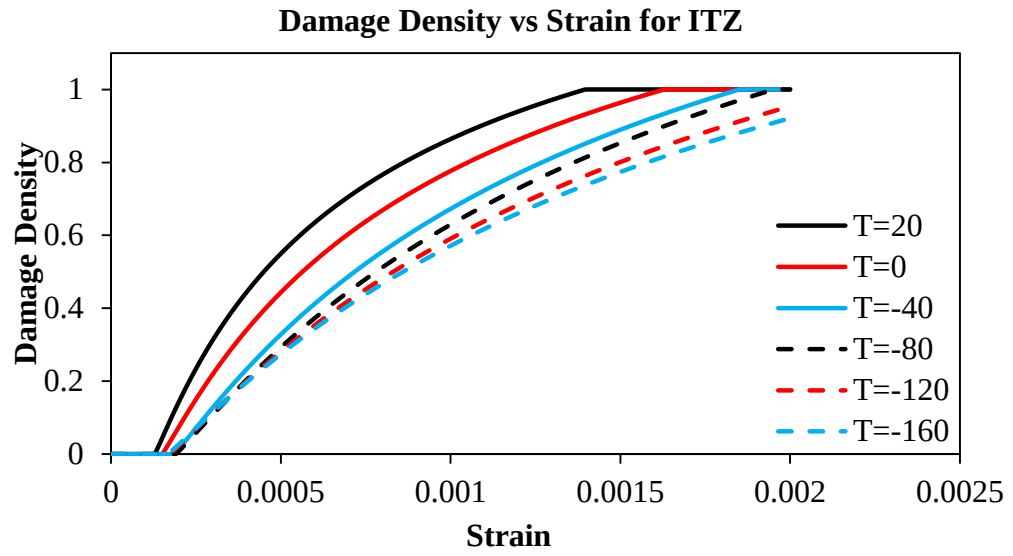

(b)

Figure 3.8 Damage density-strain relations at different temperature values for: (a) matrix and (b) ITZ (Type B).

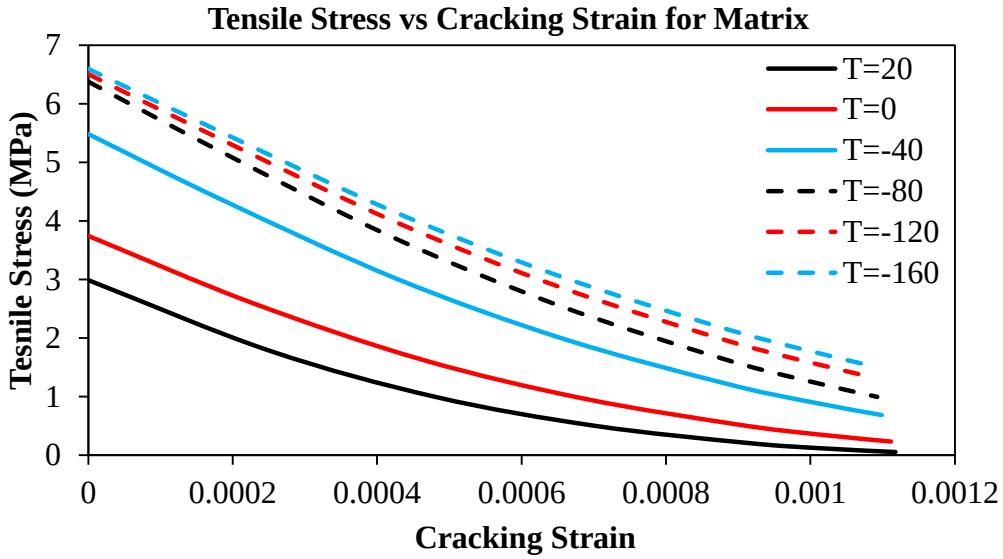

(a)

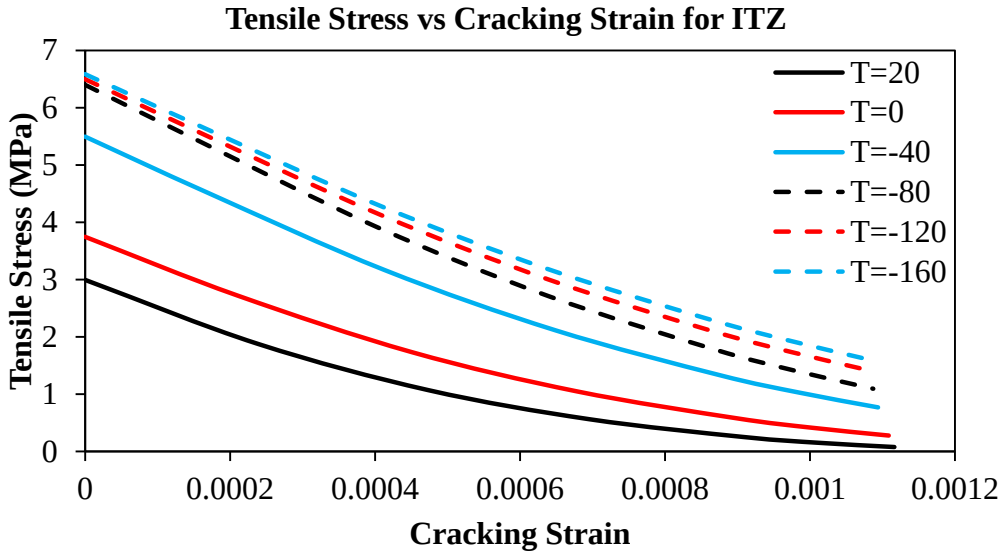

(b)

Figure 3.9 Tensile stress-cracking strain relations at different temperature values for: (a) matrix and (b) ITZ (Type B).

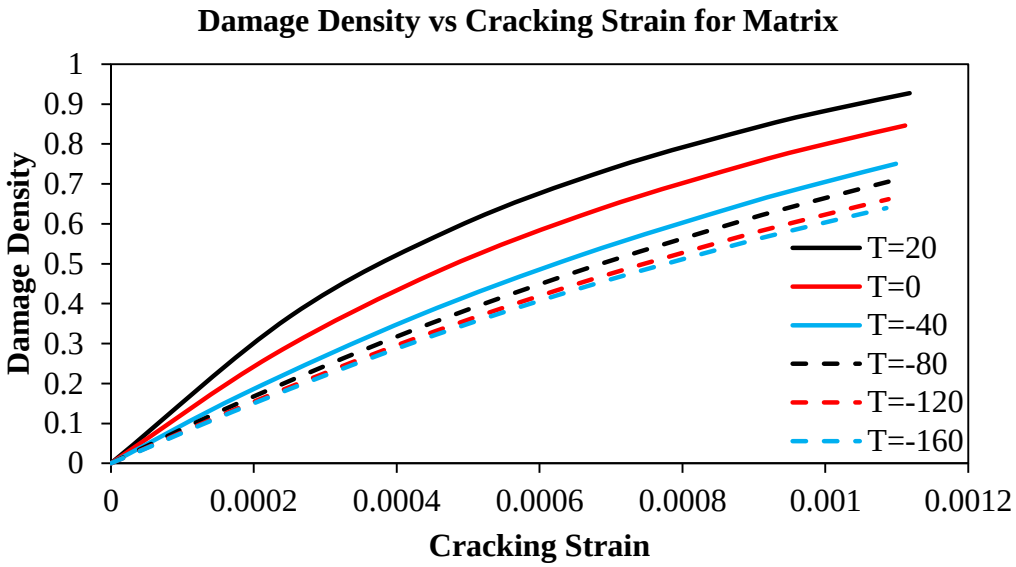

(a)

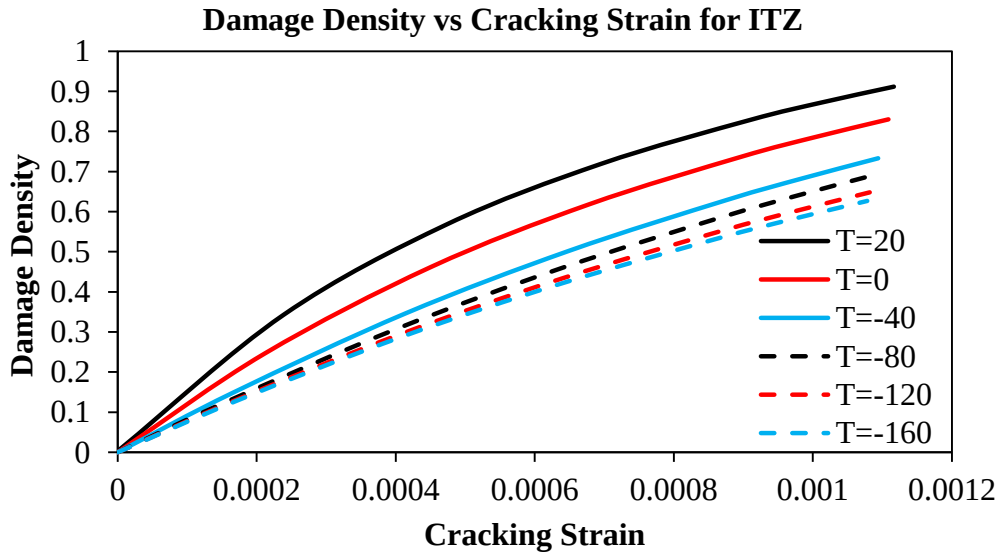

(b)

Figure 3.10 Damage density-cracking strain relations at different temperature values for: (a) matrix and (b) ITZ (Type B).

3.4 Model Sensitivity to Mesh Sizes

The sensitivity of the model to the finite element mesh size was investigated under tensile and compressive loadings.

The element sizes that were investigated were $0.1\text{mm} \times 0.1\text{mm}$, $0.5\text{mm} \times 0.5\text{mm}$, $1\text{mm} \times 1\text{mm}$, and $2\text{mm} \times 2\text{mm}$. These sizes corresponded to total number of elements of 1,211,101, 49,321, 12,562, and 3,673 (See Figure 3.11). For the tensile loading, these simulations were conducted using a tensile displacement. The same mesh size sensitivity was conducted under compressive loading using a loading increment of 0.8 μm. Generally, the concrete has lower mesh sensitivity under tensile and compressive loading and (see Figure 3.12 and Figure 3.13).

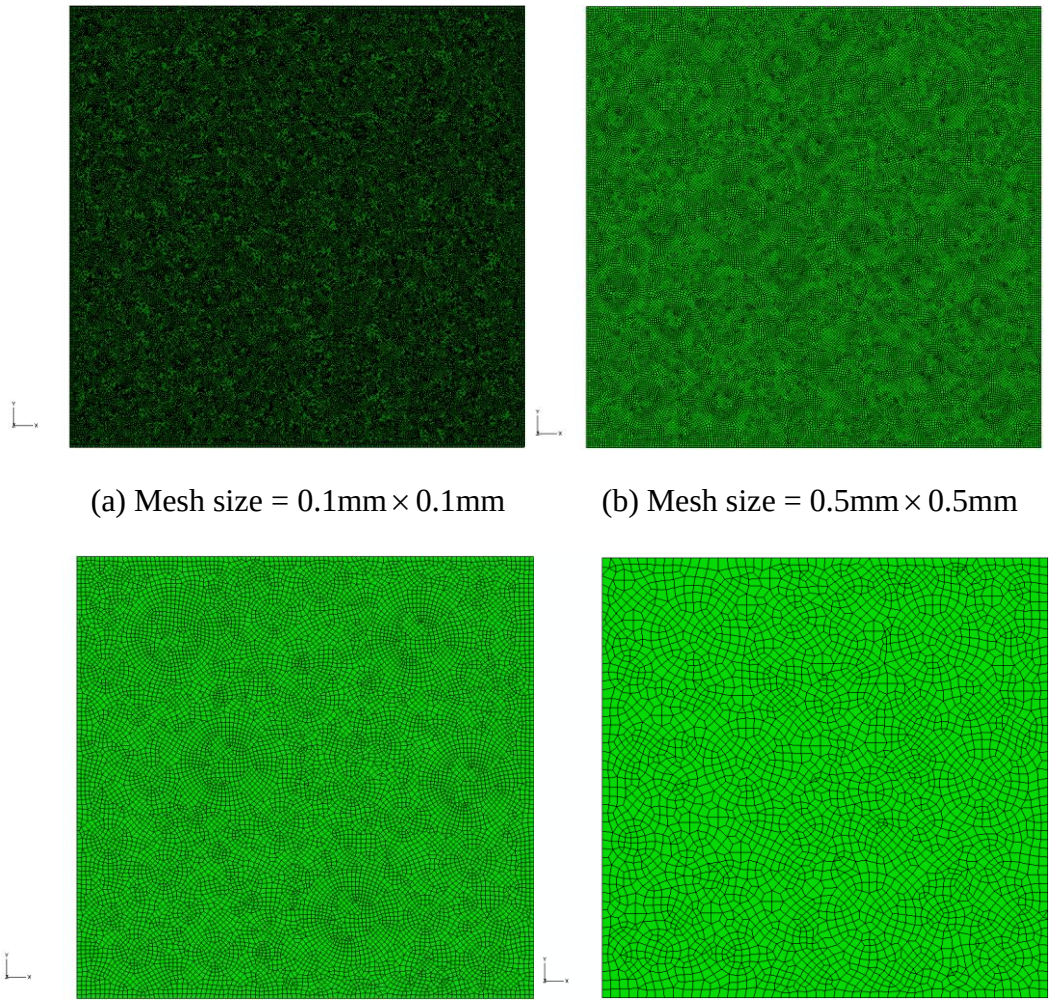

(a) Mesh size = 0.1mm × 0.1mm (b) Mesh size = 0.5mm × 0.5mm

(c) Mesh size = 1mm × 1mm (d) Mesh size = 2mm × 2mm

Figure 3.11 Different meshes sizes: (a) mesh size = 0.1mm × 0.1mm with number of elements = 1211101, (b) mesh size = 0.5mm × 0.5mm with number of elements = 49321, (c) mesh size = 1mm × 1mm with number of elements = 12562, and (d) mesh size = 2mm × 2mm with number of elements = 3673.

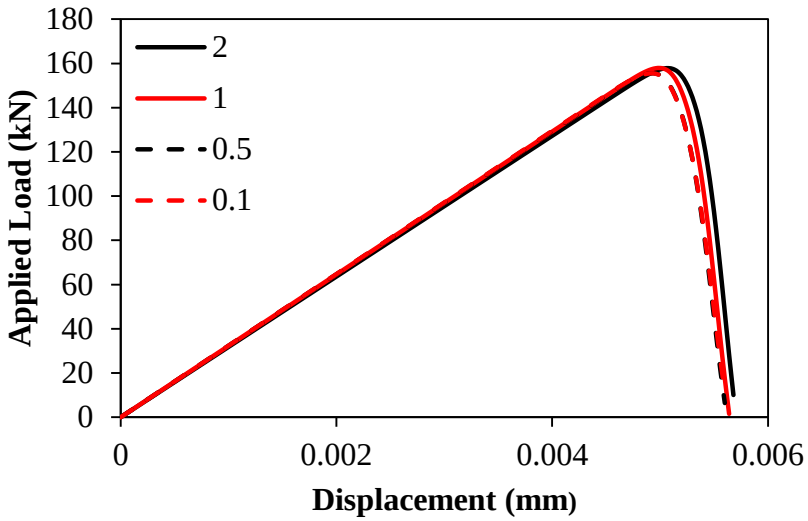

Figure 3.12 Applied load-displacement relation due to applied tensile displacement = 0.01 mm for different meshes sizes.

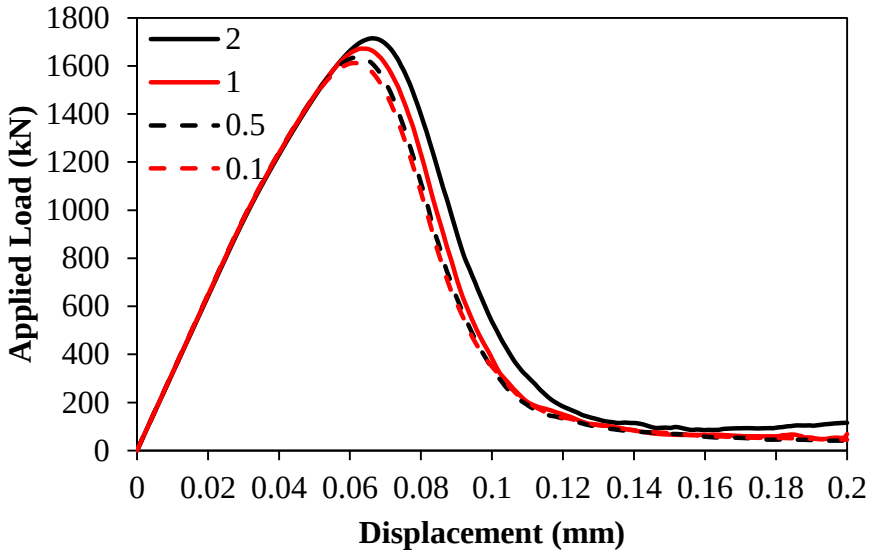

Figure 3.13 Applied load-displacement relation due to applied compressive displacement = - 0.2 mm for different meshes sizes.

The results in Figures 3.12-3.13 clearly show that there is low sensitivity to finite element size; this is an advantage that would allow us to reduce the number of elements in the model, and consequently, reduce the analysis time. Examples of the damage distributions in tensile and compressive loading are shown in Figure 3.14 and Figure 3.15.

Size of Mesh = 0.1 (The number of elements = 1211101)

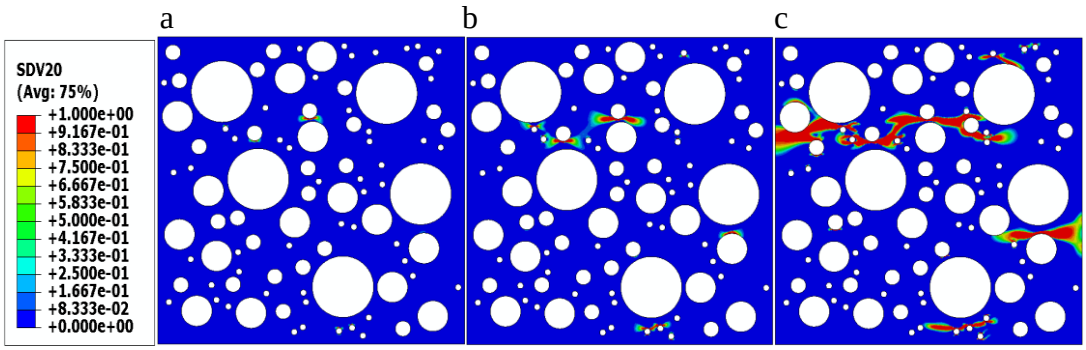

Size of Mesh = 0.5 (The number of elements = 49321)

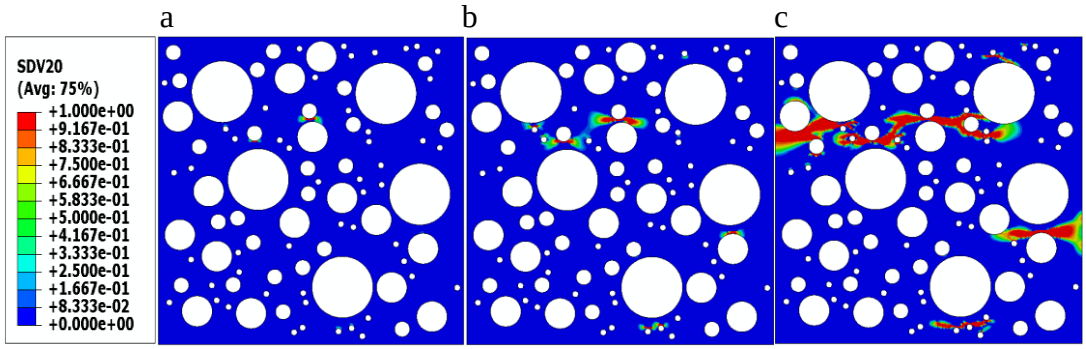

Figure 3.14 Tensile damage due to applied tensile displacement = 0.01 mm (a) Initiation at displacement = 0.00475 mm, (b) Propagation at displacement = 0.005 mm, and (c) Failure at displacement = 0.0054 mm.

Size of Mesh = 0.1 (The number of elements = 1211101)

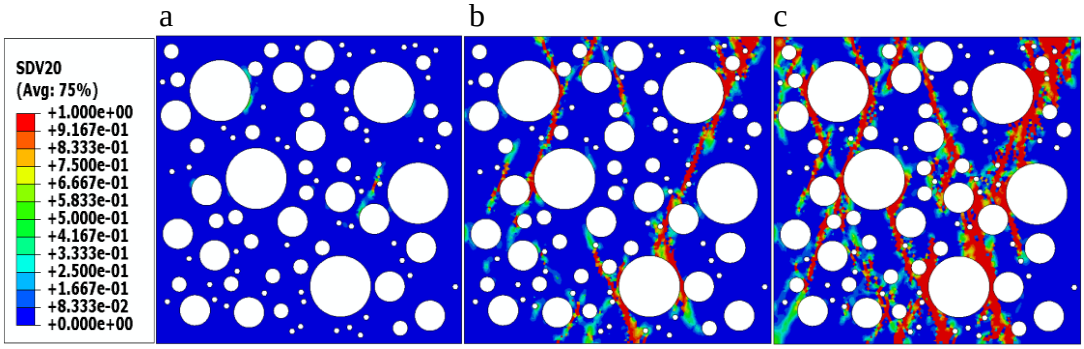

Size of Mesh = 0.5 (The number of elements = 49321)

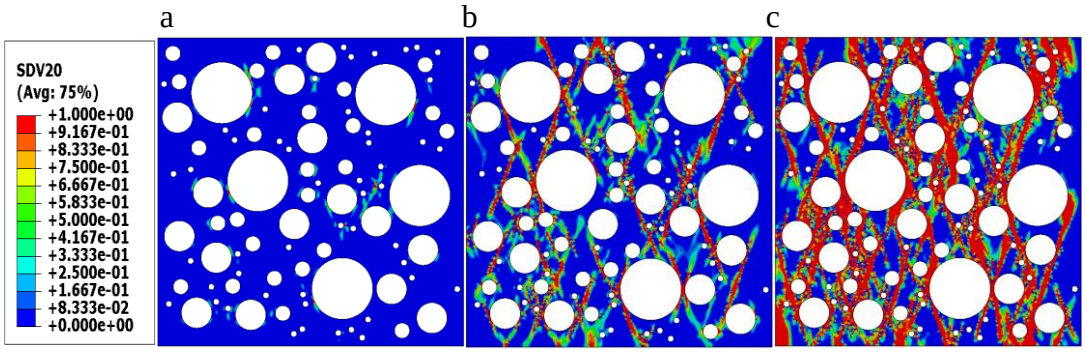

Figure 3.15 Tensile damage due to applied compressive displacement = - 0.2 mm (a) Initiation at displacement = 0.05 mm, (b) Propagation at displacement = 0.07 mm, and (c) Failure at displacement = 0.085 mm.

3.5 Summary

This chapter presented information on the generation of the meso-scale concrete model. This model consists of three phases: aggregates, mortar (or matrix) and ITZ. The aggregate phase is modeled as linear elastic material, while the mortar and ITZ are modeled using the damage plasticity concrete model. The properties of all materials are considered as a function of temperature. The elastic and strength properties were taken based on published data. There are no published data that describe the influence of

temperatures on the post-yield or damage behavior of concrete. Therefore, data were generated to represent different behavior after the damage point. The analysis involved two cases of temperature distribution:

- Case I: the whole model is initially subjected to a temperature of 20 ^{o}C and then the whole temperature is reduced to -160 ^{o}C. This case represents a rapid cooling of a concrete specimen. This analysis is referred to as the "steady state analysis".
- Case II: the model is subjected to 20 ^{o}C on the left side and -160 ^{o}C on the right side. This analysis is referred to as the "transient analysis".

As discussed in this chapter, the post yield behavior at cryogenic temperatures is not well characterized in the literature. Therefore, the analysis considers two sets of stress-strain curves. The damage in one set of curves (referred to as Type A) is faster than in the second set (referred to as Type B).

The analysis in this chapter established that the meso-scale model has low sensitivity to the finite element mesh. Therefore, it was decided to do the analysis using an element size of 1.

CHAPTER IV

SENSITIVITY ANALYSIS OF IDEALIZED MESO-SCALE MODEL

4.1 Introduction

The goal of the analysis presented in this chapter is to evaluate the effect of aggregate size, volume fraction, and coefficient of thermal expansion on the behavior of concrete subjected to cryogenic temperatures. The analysis focused on comparing the distribution of damage, Von Mises stress, and maximum principle stresses in various meso-scale models. The analysis in this chapter uses idealized shape (circular) in presenting aggregate particles in order to simplify the analysis. As discussed in Chapter III, the meso-scale model considers concrete as a composite material that consists of three phases: aggregate phase, mortar or matrix phase, and interfacial transmission zone (ITZ). The aggregate is modeled as an elastic material while the mortar and ITZ are modeled using damage plasticity model. The properties of these phases were determined from data that were obtained from comprehensive literature search. Some of the properties or models' parameters had to be assumed because they are not available from published experimental measurements.

4.2 Steady-State Analysis of Temperature Effects

In the steady-state analysis, the whole model is initially subjected to a temperature of 20 ^{o}C and then the whole temperature is reduced to -160 ^{o}C. This case represents a rapid cooling of a concrete specimen. The analysis in section 4.2 is conducted using the Type A curves shown in Figures 3.3-3.6.

4.2.1 The Effect of Aggregate Size

Two RVEs with aggregate volume fraction of 40% were generated. The first one had an aggregate radius of 6mm and the second one had an aggregate radius of 4mm. The coefficient of thermal expansion was $8\times10^{-6}°C^{-1}$ for aggregate (Mukhopadhyay and Zollinger, 2009) and $15\times10^{-6}°C^{-1}$ for the matrix and ITZ. It was found that size of particles had almost no effect on damage distribution in the model. The least temperature that the model reached and the tensile damage range are shown in Table 4.1. The distribution of damage, Von Misses stresses, and maximum principal stresses are shown in Figures 4.1-4.3. These results show that the two aggregate sizes had almost the same damage behavior.

Table 4.1 Minimum temperature and tensile damage values due to aggregate size effect Type A.

Aggregate radius (mm)	Minimum temperature (°C)	Tensile damage range
4.00	-38.58	0.449 - 0.773
6.00	-37.45	0.439 - 0.763

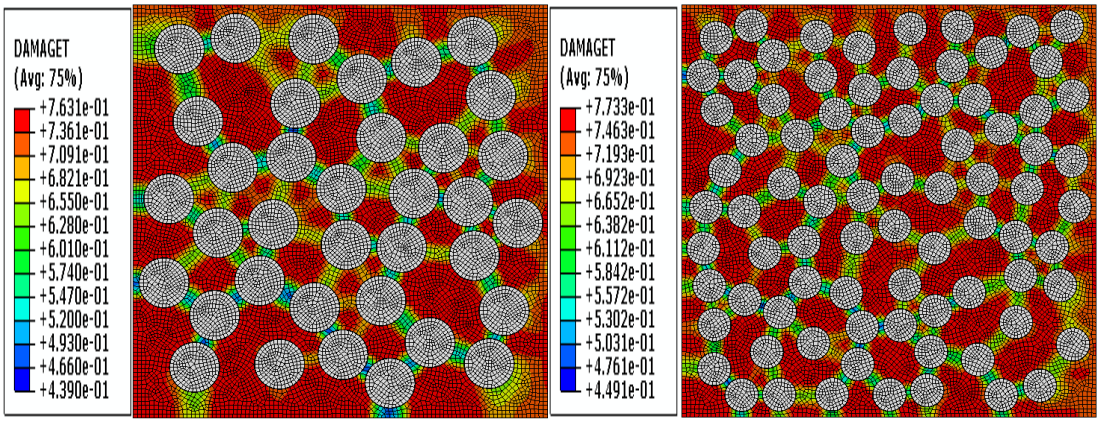

(a) (b)

Figure 4.1 Tensile damage at integration points: (a) aggregate radius = 6mm and (b) aggregate radius = 4mm.

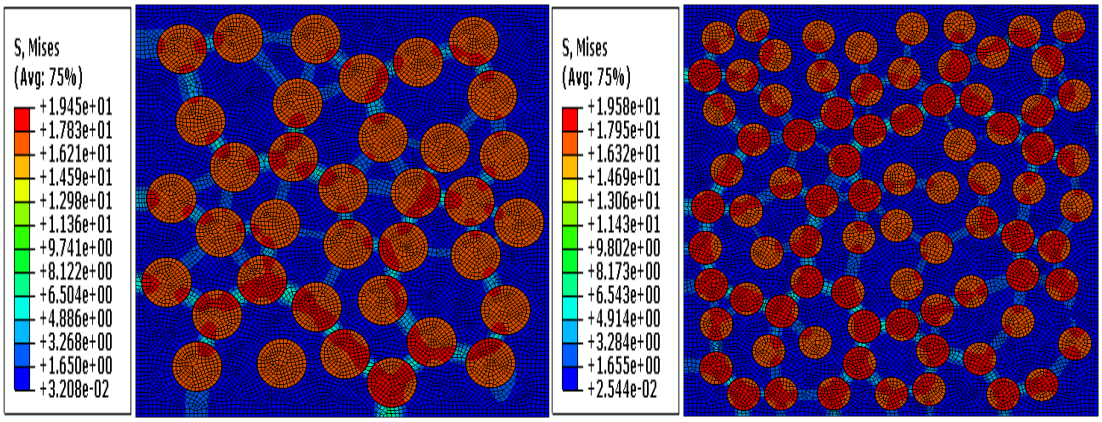

(a) (b)

Figure 4.2 Von Mises stresses: (a) aggregate radius = 6mm and (b) aggregate radius = 4mm

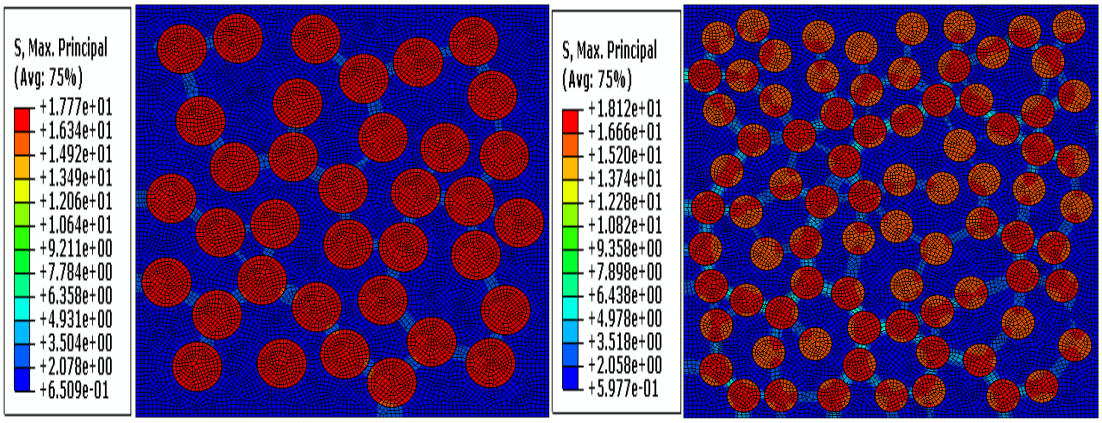

(a) (b)

Figure 4.3 Maximum Principle stresses: (a) aggregate radius = 6mm and (b) aggregate radius = 4mm.

4.2.2 The Effect of Volume Fractions with Different Aggregate Sizes

In this analysis, RVEs were generated to have four volume fractions with the same proportions of particle sizes (see Figure 4.4). Each of the RVEs had aggregate radii 10, 5, 2.5 mm. The volume fractions of the RVEs are 60%, 50%, 40%, and 30% (see Table 4.2). The RVEs with lower volume fractions reached lower temperature which means that they were able to sustain lower temperatures prior to reaching terminal damage. Table 4.3 shows aggregate and matrix properties used in these simulations. The comparison in Table 4.4 shows the damage at the same temperature of -22 ^{o}C. The RVE with 60% aggregates experienced more damage at this temperature than the other two RVEs. Overall, the volume fraction size did not have high effect on the damage distribution or stresses distribution as shown in Figures 4.5-4.7.

Table 4.2 The number of aggregate in RVEs with cross section 100 mm × 100 mm.

RVE	Volume fraction (%)	Number of aggregate with radius (10 mm)	Number of aggregate with radius (5 mm)	Number of aggregate with radius (2.5 mm)
1	30	5	11	23
2	40	6	17	40
3	50	8	19	51
4	60	10	22	60

Table 4.3 The aggregate and matrix properties used in volume fraction simulations.

RVE	Volume fraction (%)	Aggregate radius (mm)	Aggregate CTE α (1/°C)	Mortar CTE α (1/°C)
1	30	10, 5 , 2.5	8×10^{-6}	15×10^{-6}
2	40	10, 5 , 2.5	8×10^{-6}	15×10^{-6}
3	50	10, 5 , 2.5	8×10^{-6}	15×10^{-6}
4	60	10, 5 , 2.5	8×10^{-6}	15×10^{-6}

Table 4.4 Minimum temperature and tensile damage values due to aggregate volume fraction effect Type A.

Volume fraction (%)	Minimum temperature (°C)	Tensile damage range at minimum temperature	Tensile damage range at temperature -22°C
30	-39	0.427 - 0.827	0.335 - 0.616
40	-33	0.378 - 0.724	0.328 - 0.620
50	-31	0.412 - 0.770	0.360 - 0.626
60	-22	0.342 - 0.631	0.342 - 0.631

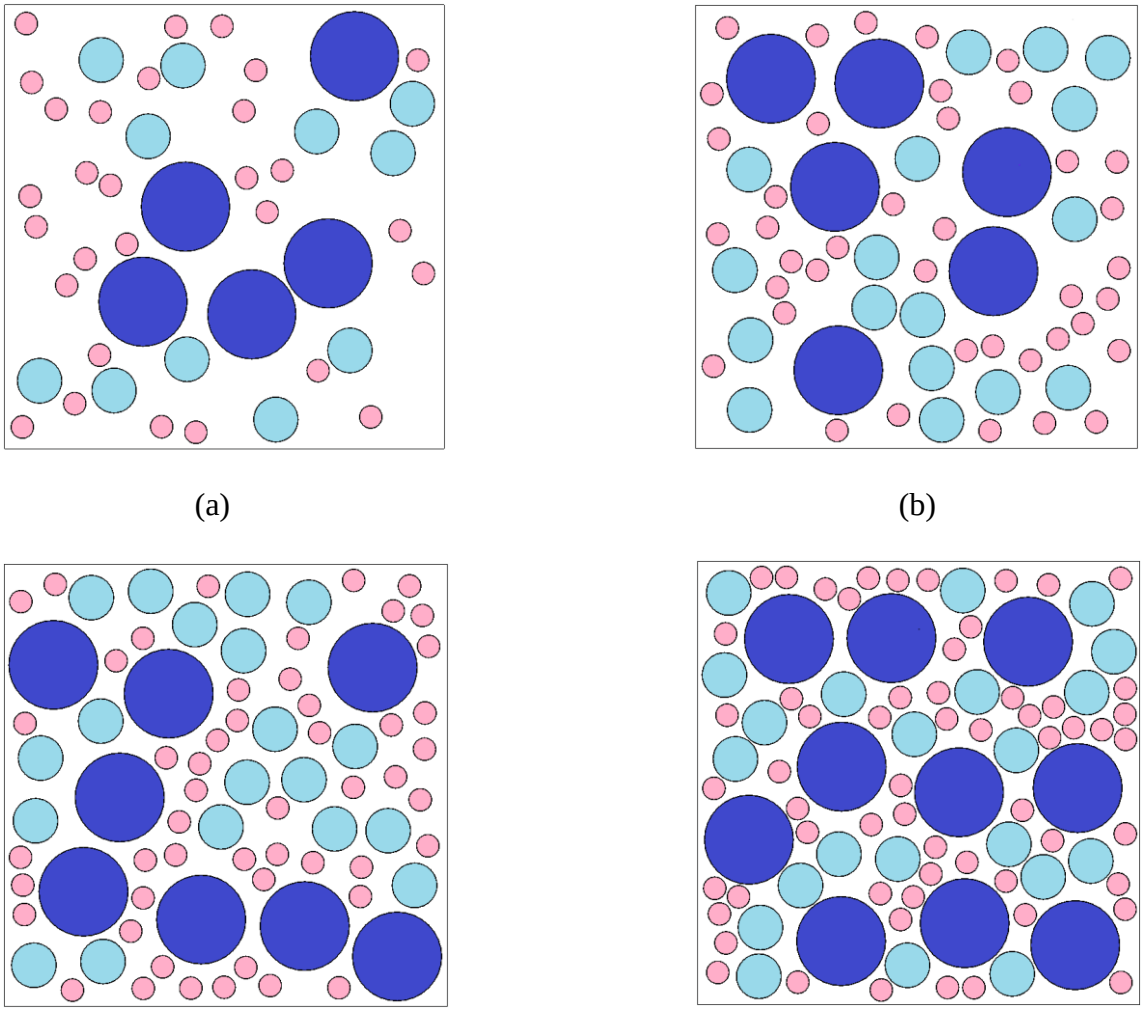

Figure 4.4 Aggregate volume fractions: (a) 30%, (b) 40%, (c) 50%, and (d) 60%.

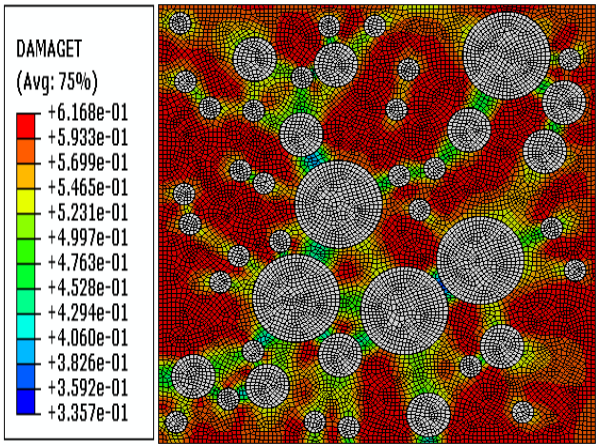

(a)

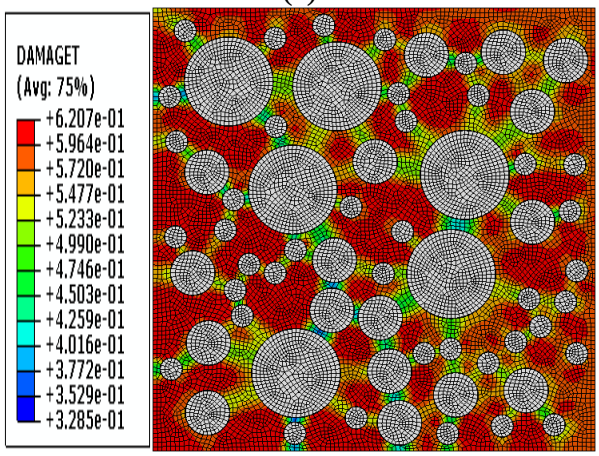

(b)

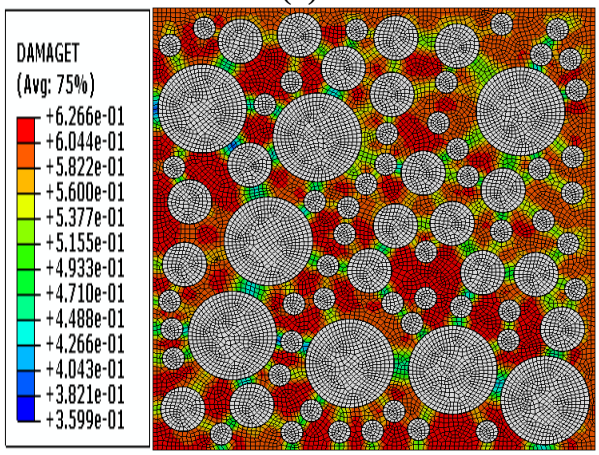

(c)

Figure 4.5 Tensile damage for different volume fraction values at temperature = -22°C: (a) VF = 30%, (b) VF = 40%, (c) VF = 40%, and (d) VF = 60%.

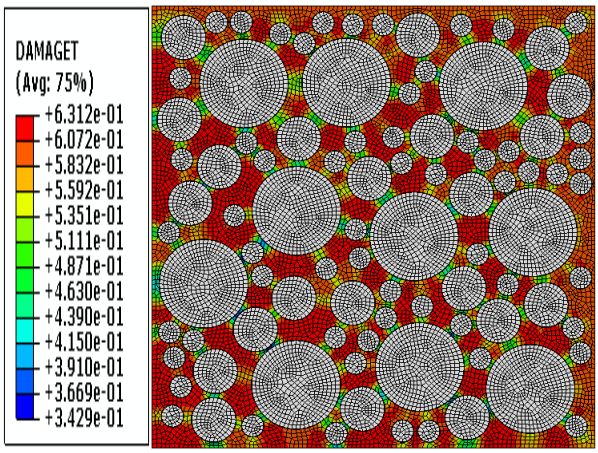

(d)

Figure 4.5 Continued.

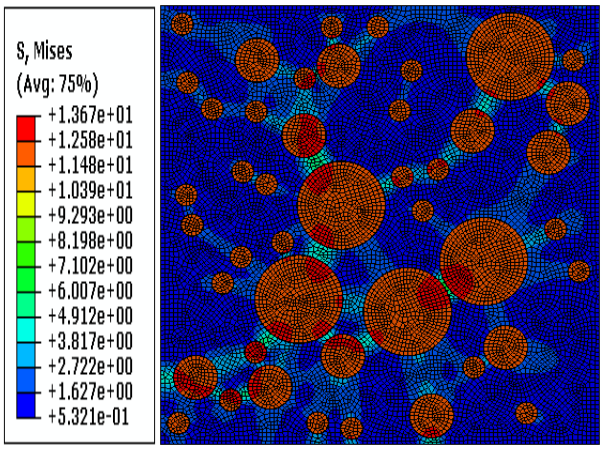

(a)

Figure 4.6 Von Mises stresses for different volume fraction values at temperature = -22°C: (a) VF = 30%, (b) VF = 40%, (c) VF = 40%, and (d) VF = 60%.

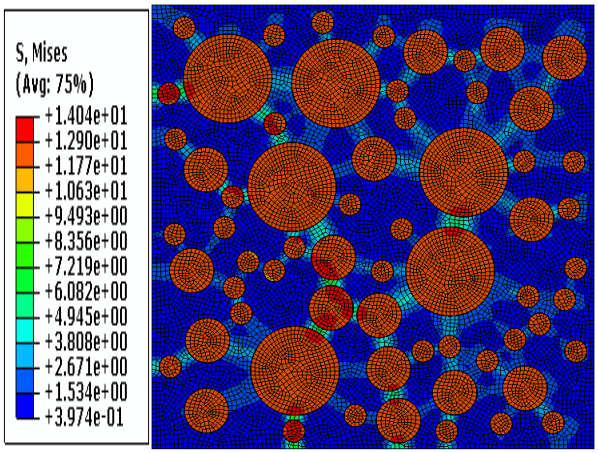

(b)

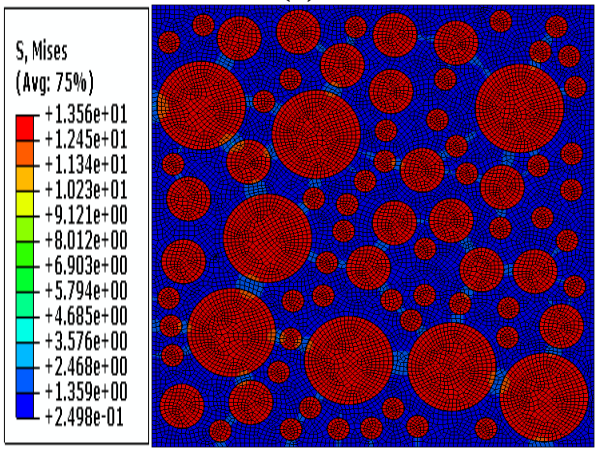

(c)

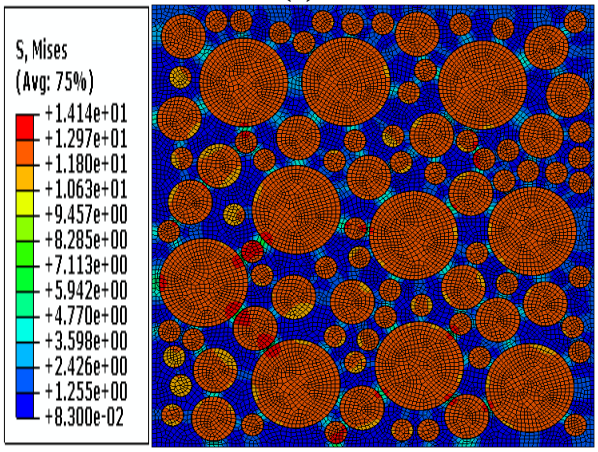

(d)

Figure 4.6 Continued.

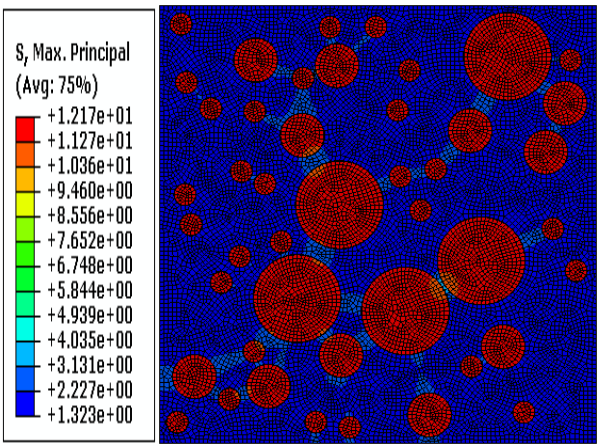

(a)

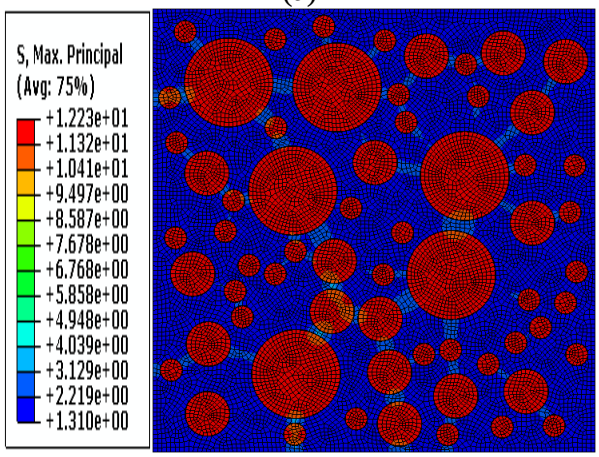

(b)

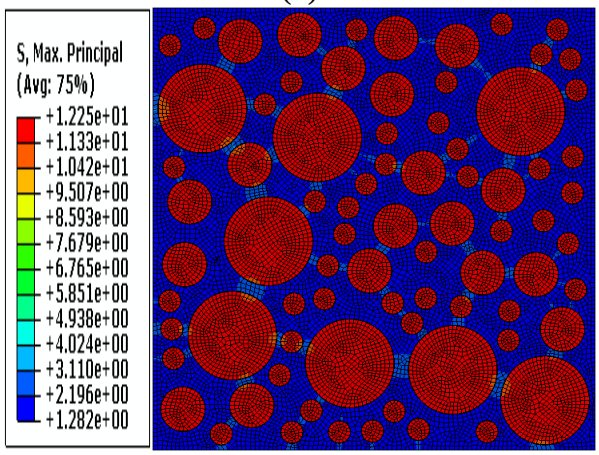

(c)

Figure 4.7 Maximum Principle stresses for different volume fraction values at temperature = -22°C: (a) VF = 30%, (b) VF = 40%, (c) VF = 40%, and (d) VF = 60%.

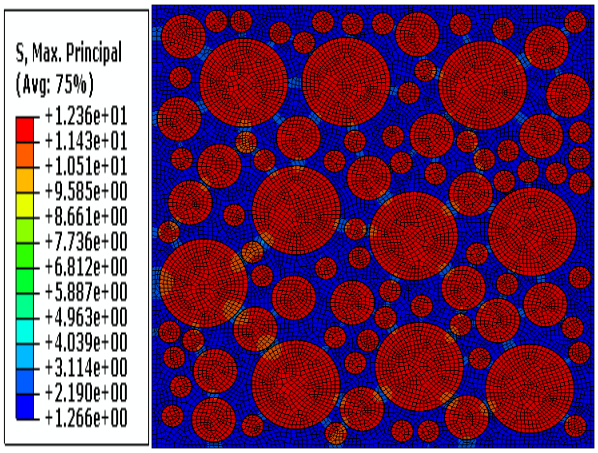

(d)

Figure 4.7 Continued.

4.2.3 The Effect of Coefficient of Thermal Expansion

The representative volume element (RVE), which had one aggregate radius size of 6mm, was used with different values of coefficient of thermal expansion (CTE) to investigate the effects of CTE of aggregate and matrix on concrete damage.

The analysis results shown in Table 4.5 clearly show that damage values increased with an increase in the difference between the CTE values of aggregate and matrix. The third RVE with the highest difference in CTE experienced the highest damage and experienced the least reduction in temperature. The first RVE with least difference in CTE reached -75 ^{o}C, while the third RVE with the highest difference in CTE reached only -28 ^{o}C. When the three RVEs are compared at the same temperature of -28 ^{o}C, the damage in the third RVE reached 0.695 while it only reached 0.470 in the first and second RVEs.

Table 4.5 Minimum temperature and tensile damage values due to CTE effect Type A.

RVE	Aggregate CTE α (1/°C)	Mortar CTE α (1/°C)	Minimum temperature (°C)	Tensile damage range at minimum temperature	Tensile damage range at temperature -28°C
1	6×10^{-6}	10×10^{-6}	-75	0.469 - 0.851	0.274 - 0.470
2	8×10^{-6}	15×10^{-6}	-37	0.439 - 0.763	0.386 - 0.683
3	6×10^{-6}	15×10^{-6}	-28	0.367 - 0.695	0.367 - 0.695

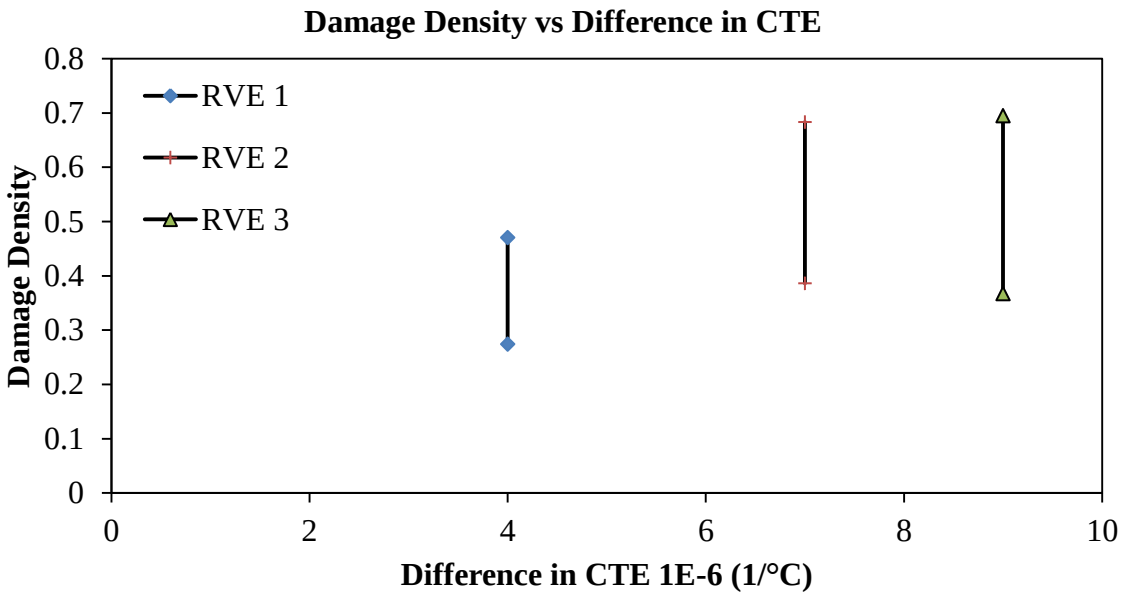

Figure 4.8 The Relation between the difference in CTEs and damage density

Figures 4.8-4.10 show that both damage and stresses were higher in the RVE that had the highest difference in the CTE.

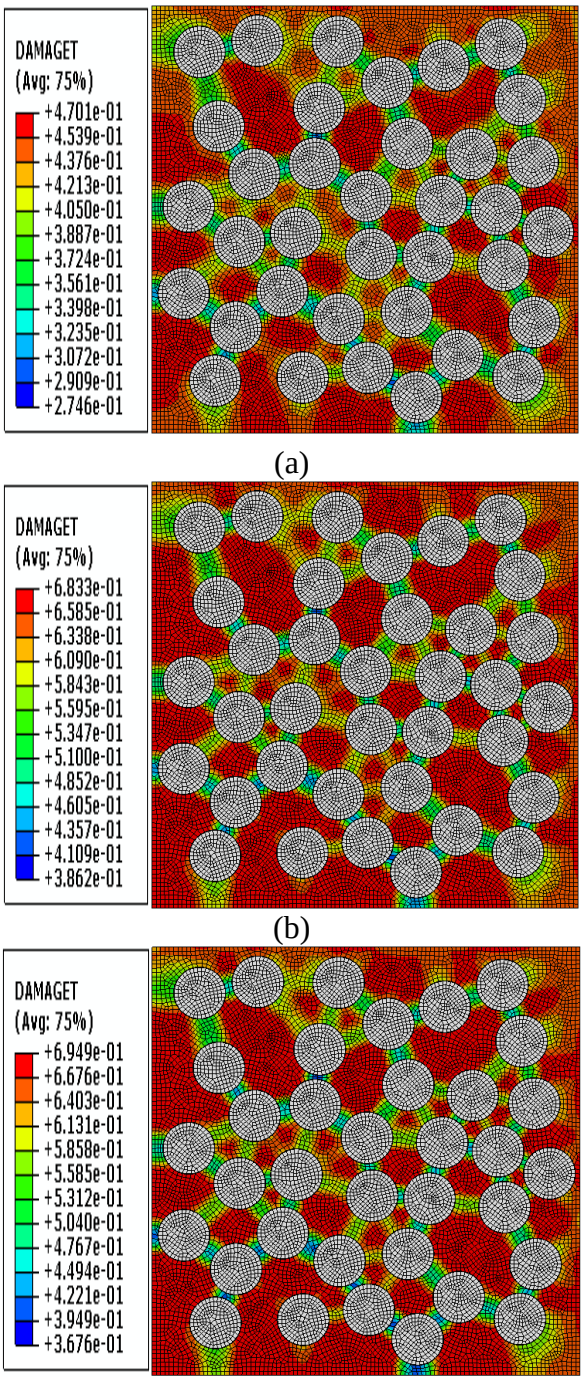

Figure 4.9 Tensile damage for different CTEs at temperature = -28°C: (a) aggregate CTE= 6×10^{-6}°C^{-1} and mortar CTE= 10×10^{-6}°C^{-1}, (b) aggregate CTE= 8×10^{-6}°C^{-1} and mortar CTE= 15×10^{-6}°C^{-1}, and (c) aggregate CTE= 6×10^{-6}°C^{-1} and mortar CTE= 15×10^{-6}°C^{-1}.

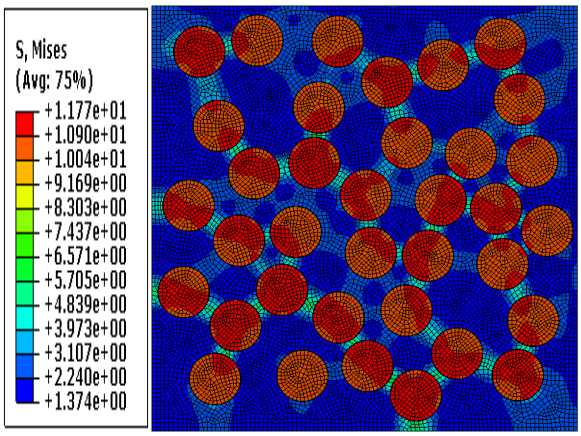

(a)

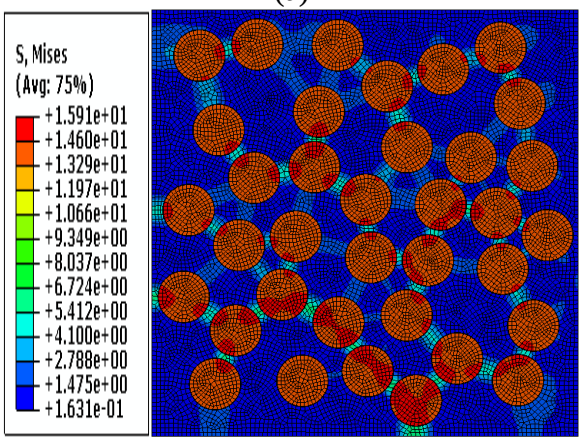

(b)

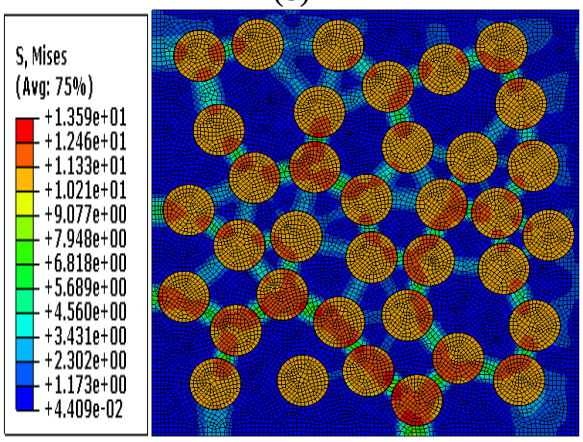

(c)

Figure 4.10 Von Mises for different CTEs at temperature = -28°C: (a) aggregate CTE= 6×10^{-6}°C^{-1} and mortar CTE=10×10^{-6}°C^{-1}, (b) aggregate CTE=8×10^{-6}°C^{-1} and mortar CTE=15×10^{-6}°C^{-1}, and (c) aggregate CTE=6×10^{-6}°C^{-1} and mortar CTE=15×10^{-6}°C^{-1}.

The maximum principle stresses values for RVEs with different CTE values of aggregate and matrix are shown in Figure 4.11 at the same temperature value = -28°C.

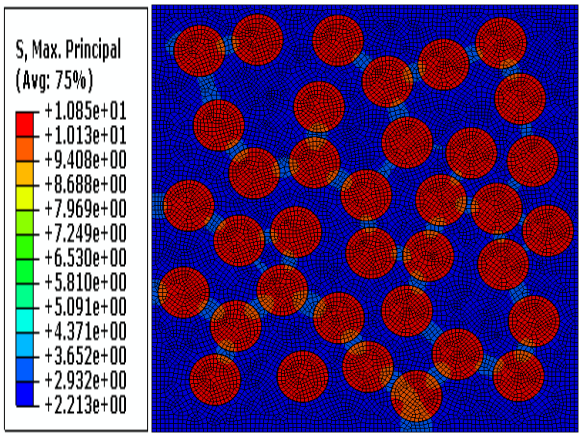

(a)

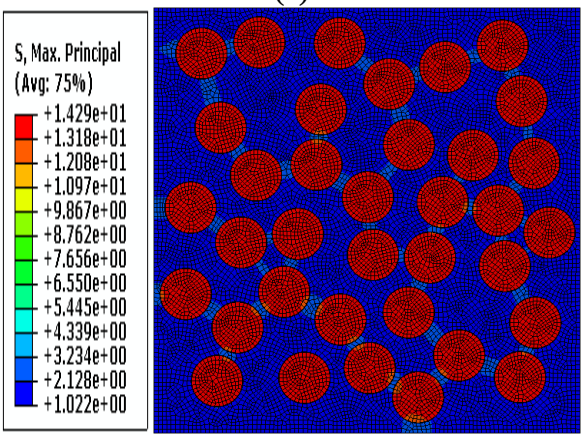

(b)

Figure 4.11 Maximum Principle stresses for different CTEs at temperature = -28°C: (a) aggregate CTE= 6×10^{-6}°C^{-1} and mortar CTE= 10×10^{-6}°C^{-1}, (b) aggregate CTE= 8×10^{-6}°C^{-1} and mortar CTE= 15×10^{-6}°C^{-1}, and (c) aggregate CTE= 6×10^{-6}°C^{-1} and mortar CTE= 15×10^{-6}°C^{-1}.

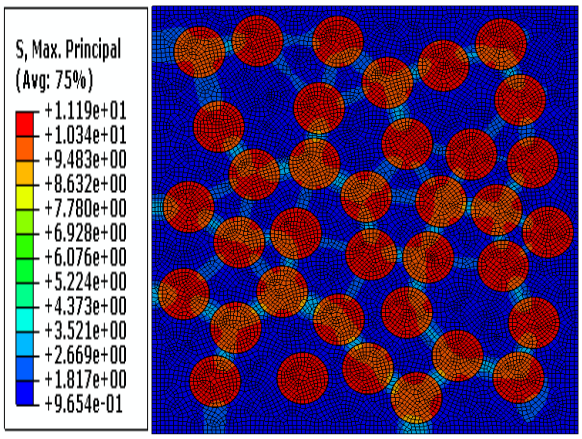

(c)

Figure 4.11 Continued.

4.2.4 The Effect of Matrix and ITZ Behavior

As discussed earlier in Chapter III, there are no data that show the post-damage behavior of concrete at various temperatures. Therefore, it was decided to investigate the effect of post-damage behavior of matrix and ITZ properties on the damage at different temperatures. The Tensile stress in Type B curves (see Figure 3.7) decreases more gradual than the Type A curves shown in (see Figure 3.3) and used in all previous analyses. As a result, the damage-strain relation in Type B curves (see Figure 3.8) reaches the maximum (full damage =1) slower than the first one (see Figure 3.4). The analysis in the previous section with different CTEs is repeated here but with using the curves in Figures 3.7-3.10 to represent the behavior of mortar and ITZ.

Table 4.6 Minimum temperature and tensile damage values due to CTE effect Type B.

RVE	Aggregate CTE α (1/°C)	Mortar CTE α (1/°C)	Minimum temperature (°C)	Tensile damage range at minimum temperature	Tensile damage range at temperature -38°C
1	6×10^{-6}	10×10^{-6}	-160	0.480 - 0.703	0.255 - 0.445
2	8×10^{-6}	15×10^{-6}	-160	0.565 - 0.752	0.353 - 0.649
3	6×10^{-6}	15×10^{-6}	-38	0.330 - 0.652	0.330 - 0.652

Comparing the results in Table 4.5 and Table 4.6 shows that the minimum temperature value decreased when the post-damage behavior is less severe in Type B (gradual decrease in tensile stress). For example, the minimum temperature was -28°C in Table 4.5 for the third RVE, but it only reached -38 °C in Table 4.6 with same damage value. The first and second RVEs were able to reach -160 ^{o}C in this analysis (Table 4.6), while these two RVEs reached only -37 ^{o}C and -75 ^{o}C in the results in Table 4.5. It is also interesting to note that the change in the tensile stress-strain curve made significant impact on the temperature that the first and second RVE could sustain. These results emphasize the importance of obtaining accurate measurements of the tensile stress-strain behavior of concrete at low temperatures. This behavior could significantly influence the temperature that concrete can sustain before it reaches critical damage. The results show that we should put emphasis on designing concrete that has graduate reduction in tensile stress after the initial yielding point.

The tensile damage values using Type B curves for RVEs with different CTE of aggregate and matrix effect are shown in Figure 4.12.

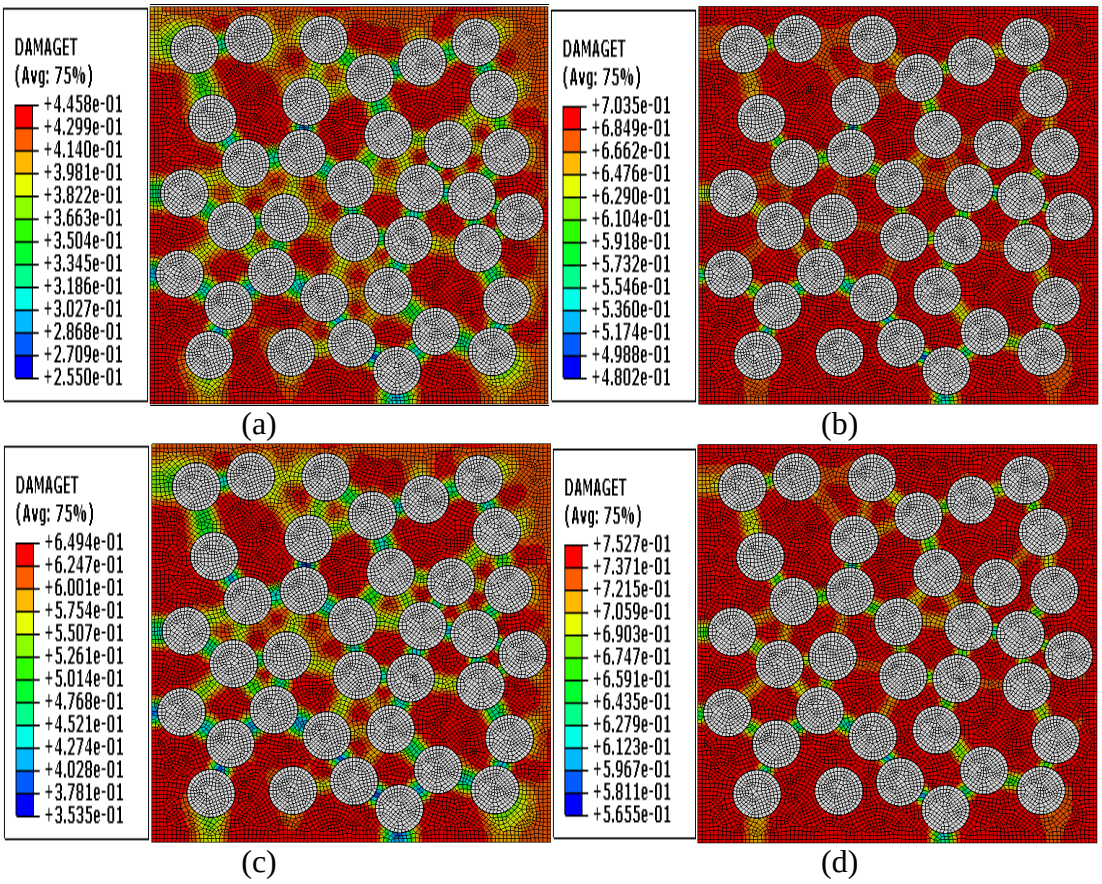

Figure 4.12 Tensile damage for different CTEs: (a) aggregate CTE= 6×10^{-6}°C^{-1} and mortar CTE= 10×10^{-6}°C^{-1} at T= -38°C, (b) aggregate CTE= 6×10^{-6}°C^{-1} and mortar CTE= 10×10^{-6}°C^{-1} at T= -160°C, (c) aggregate CTE= 8×10^{-6}°C^{-1} and mortar CTE= 15×10^{-6}°C^{-1} at T= -38°C, (d) aggregate CTE= 8×10^{-6}°C^{-1} and mortar CTE= 15×10^{-6}°C^{-1} at T= -160°C, (e) aggregate CTE= 6×10^{-6}°C^{-1} and mortar CTE= 15×10^{-6}°C^{-1} at T= -38°C.

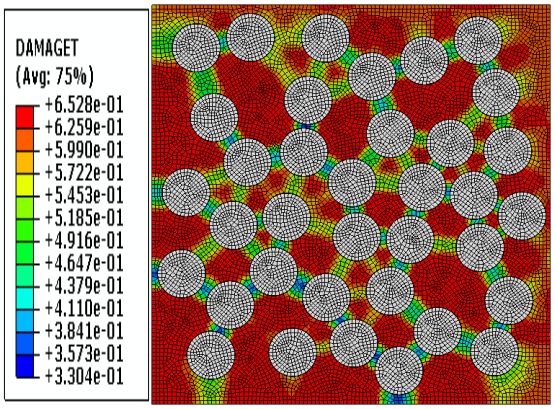

(e)

Figure 4.12 Continued.

The Von Mises stresses values using Type B curves for RVEs with different CTE of aggregate and matrix effect are shown in Figure 4.13.

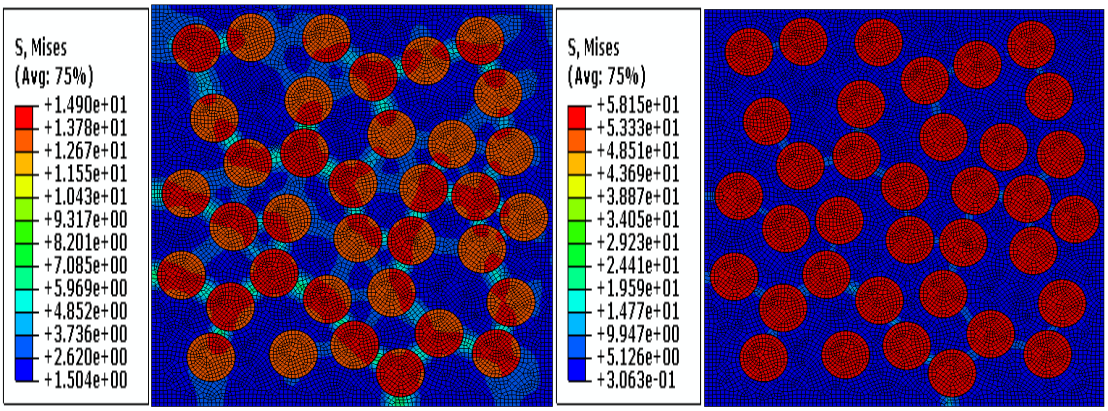

(a) (b)

Figure 4.13 Von Mises for different CTEs: (a) aggregate CTE= 6×10^{-6}°C^{-1} and mortar CTE= 10×10^{-6}°C^{-1} at T= -38°C, (b) aggregate CTE= 6×10^{-6}°C^{-1} and mortar CTE= 10×10^{-6}°C^{-1} at T= -160°C, (c) aggregate CTE= 8×10^{-6}°C^{-1} and mortar CTE= 15×10^{-6}°C^{-1} at T= -38°C, (d) aggregate CTE= 8×10^{-6}°C^{-1} and mortar CTE= 15×10^{-6}°C^{-1} at T=-160°C, (e) aggregate CTE= 6×10^{-6}°C^{-1} and mortar CTE= 15×10^{-6}°C^{-1} at T= -38°C.

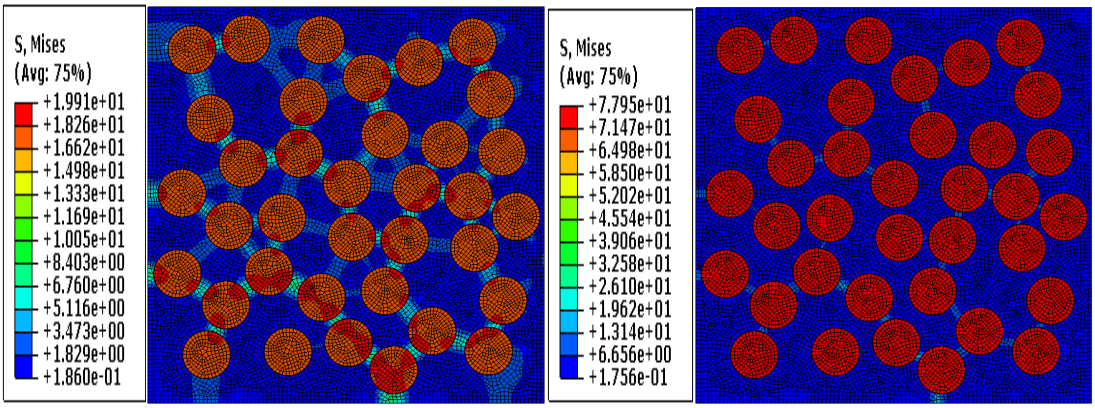

(c)

(d)

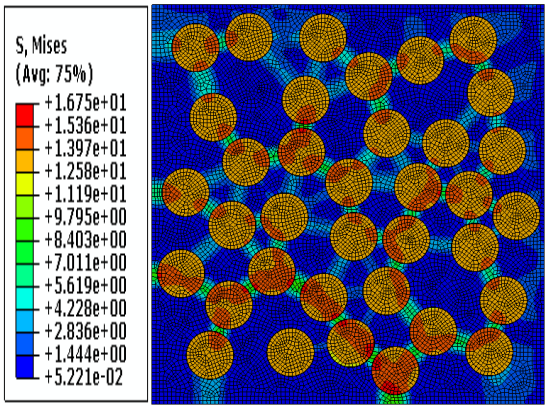

(e)

Figure 4.13 Continued.

The maximum principle stresses values using Type B for RVEs with different CTE values of aggregate and matrix effect are shown in Figure 4.14.

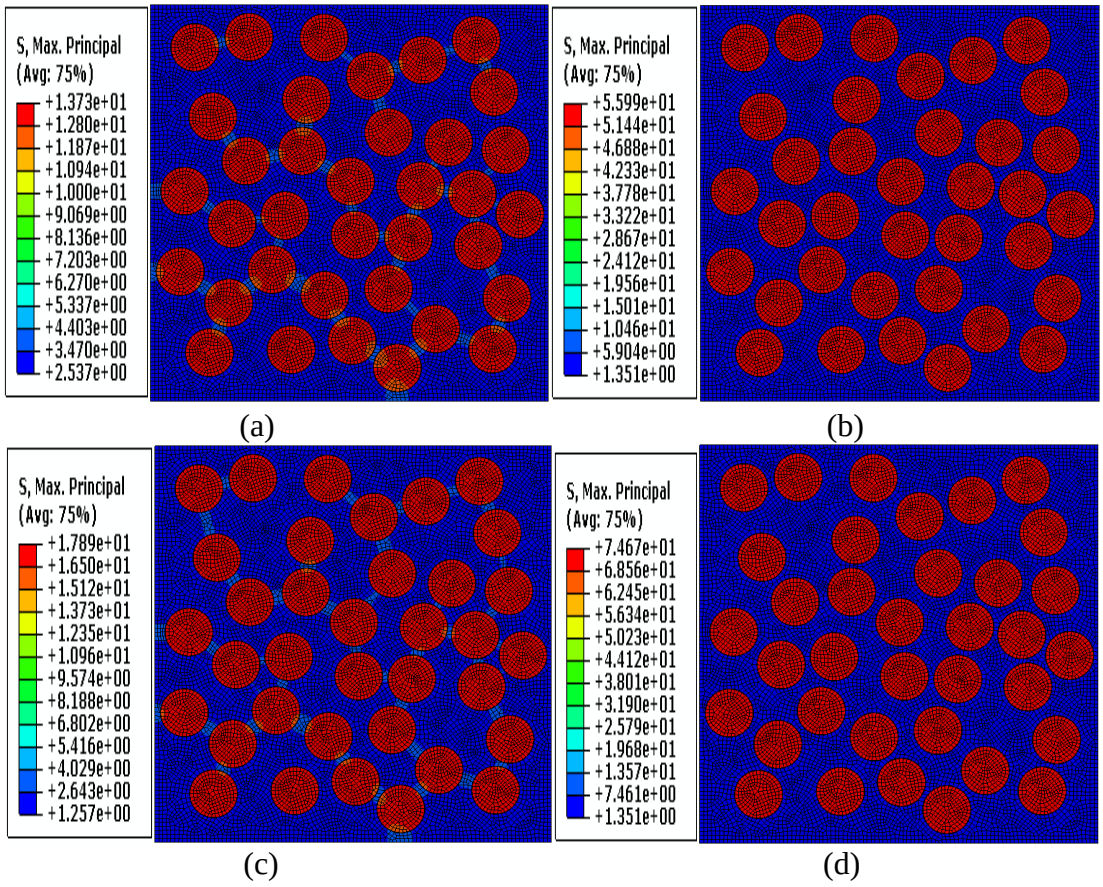

Figure 4.14 Maximum Principle stresses for different CTEs :(a) aggregate CTE= 6×10^{-6}°C^{-1} and mortar CTE=10×10^{-6}°C^{-1} at T= -38°C, (b) aggregate CTE=6×10^{-6}°C^{-1} and mortar CTE=10×10^{-6}°C^{-1} at T= -160°C, (c) aggregate CTE=8×10^{-6}°C^{-1} and mortar CTE=15×10^{-6}°C^{-1} at T= -38°C, (d) aggregate CTE=8×10^{-6}°C^{-1} and mortar CTE= 15×10^{-6}°C^{-1} at T= -160°C, (e) aggregate CTE=6×10^{-6}°C^{-1} and mortar CTE= 15×10^{-6}°C^{-1} at T= -38°C.

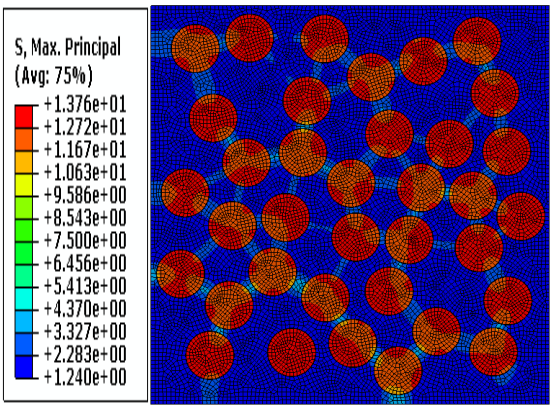

(e)

Figure 4.14 Continued**.**

4.3 Transient Analysis of Temperature Effects

The transient analysis involves applying -160 ^{o}C on the right side of the model and 20 ^{o}C on the left side of the model. The analysis was conducted using Type A stress-strain curves. The thermal properties for aggregate and matrix are used in this section as shown in Table 4.7.

Table 4.7 The thermal properties for aggregate and matrix used in transient analysis.

Thermal Properties	Aggregate	Matrix	ITZ
Specific Heat ($J/kg.^{\circ}C$)	900	1000	1000
Thermal Conductivity ($W/(m.^{\circ}C)$)	1.3	0.5	0.5

4.3.1 The Effect of Aggregate Size

The analysis of RVEs with aggregate radii of 4 mm and 6 mm showed that the number of elements which have zero damage density with aggregate radius 4mm in Figure 4.15 (b) is more than the number of elements with aggregate radius size of 6 mm in Figure 4.15 (c) at a temperature = -60°C. Consequently, the RVE with aggregate radius size of 4 mm reached a low temperature value of -150°C in comparison of a temperature of -60°C for the RVE with 6 mm particles. The damage density increased as the temperature decreased in the right hand side (see Figure 4.15 (b)). The difference in aggregate and matrix properties caused the damage to start in the ITZ as it is shown in Figure 4.16.

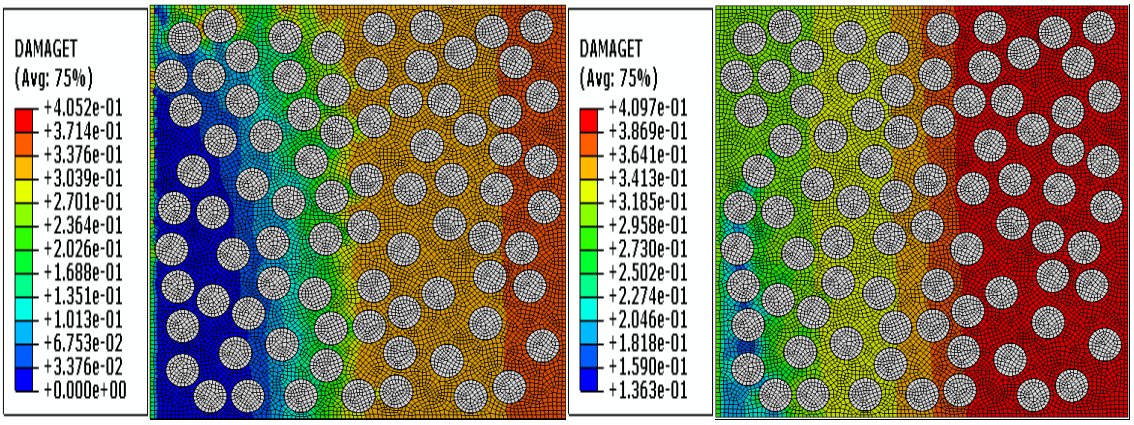

(a) (b)

Figure 4.15 Tensile damage at integration points: (a) aggregate radius = 4mm at T= -60°C, (b) aggregate radius = 4mm at T= -150°C, and (c) aggregate radius = 4mm at T= -60°C.

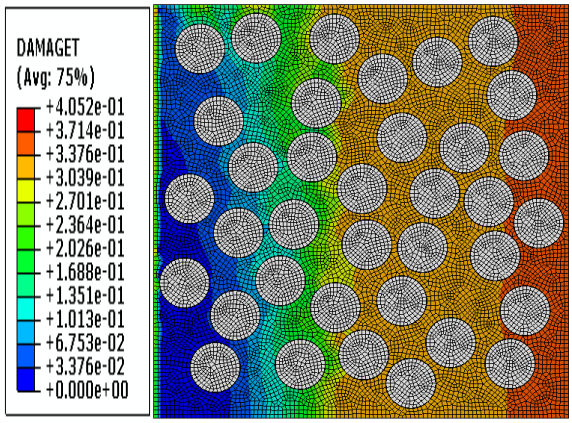

(c)

Figure 4.15 Continued.

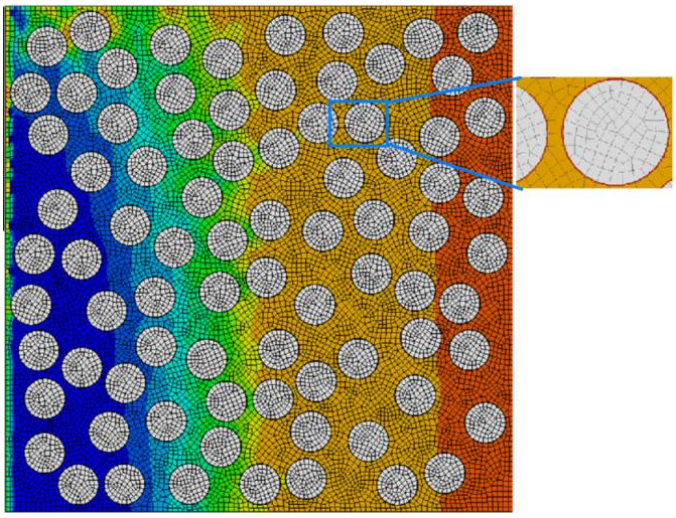

Figure 4.16 The damage in aggregate radius size = 4 mm shows the initial damage begins in the ITZ.

The Von Mises stresses for the RVE with aggregate radius of 4mm in Figure 4.17 (a) is slightly higher than the RVE with aggregate radius of 6mm in Figure 4.17 (c). The number of elements in the 4mm RVE that experienced damage was lower than the number of elements in the 6mm RVE at the same temperature value of -60°C. The maximum principle stresses values for different aggregate sizes are shown in Figure 4.18.

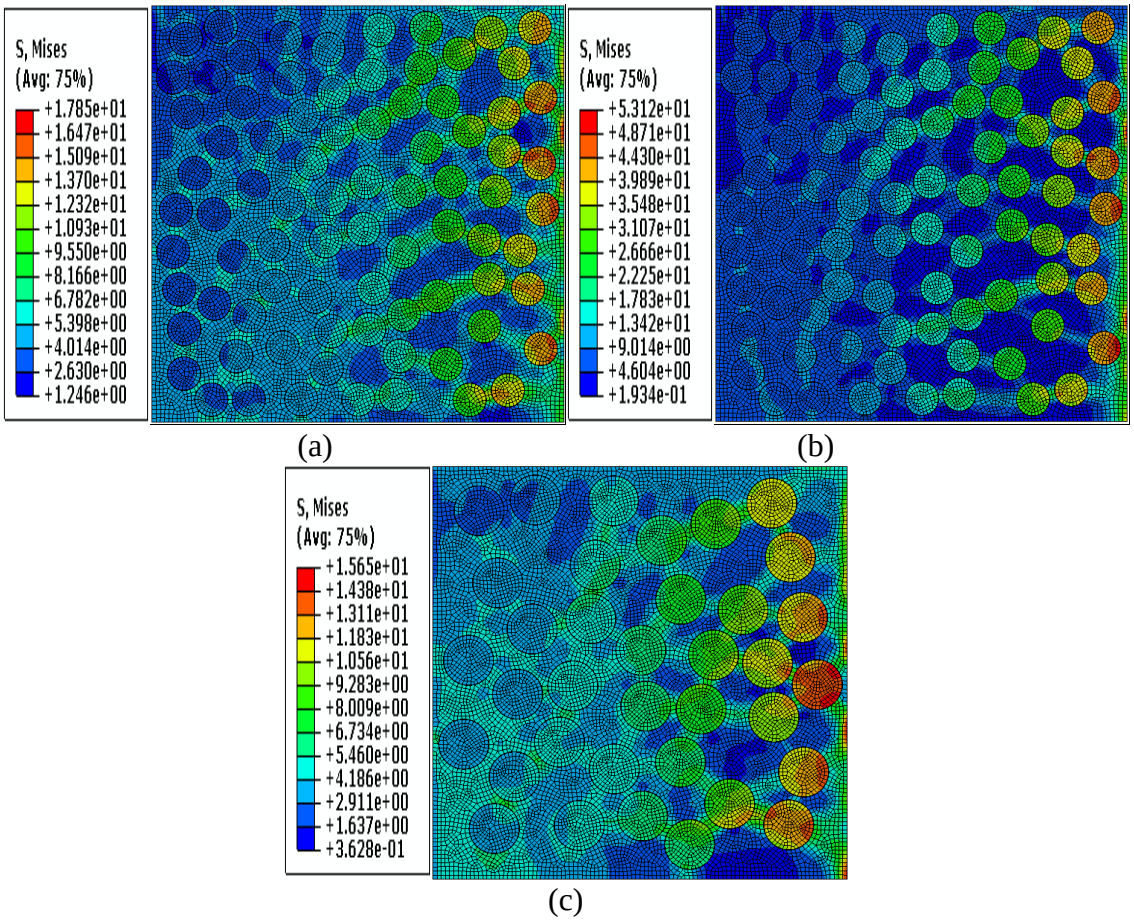

Figure 4.17 Von Mises Stresses: (a) aggregate radius = 4mm at T= -60°C, (b) aggregate radius = 4mm at T= -150°C, and (c) aggregate radius = 6mm at T= -60°C.

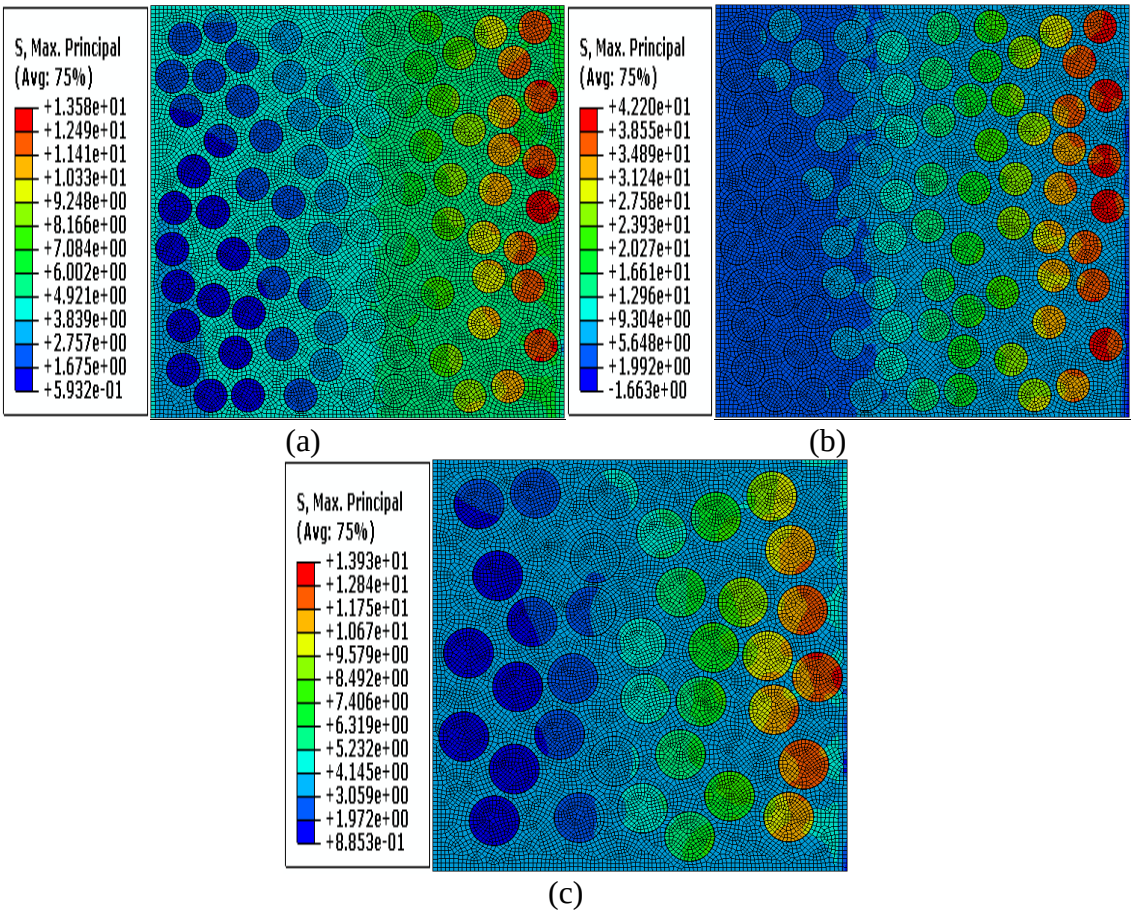

Figure 4.18 Maximum Principle Stresses (a) aggregate radius = 4mm at T= -60°C, (b) aggregate radius = 4mm at T= -150°C, and (c) aggregate radius = 6mm at T= -60°C.

4.3.2 The Effect of Volume Fraction with Different Aggregate Sizes

The RVE with the highest volume fraction of aggregates experienced more damage and didn't reach the same low temperatures as the first RVE with the lowest volume fraction (see Table 4.8).

Table 4.8 Minimum temperature and tensile damage values due to aggregate volume fraction effect for transient analysis.

RVE	Aggregate CTE α (1/°C)	Mortar CTE α (1/°C)	Minimum temperature (°C)	Tensile damage range at minimum temperature
1	8×10^{-6}	15×10^{-6}	-100	0.409
2	8×10^{-6}	15×10^{-6}	-80	0.408
3	8×10^{-6}	15×10^{-6}	-60	0.405

The number of elements with zero damage density in the left side of the RVEs (see Figure 4.19 (a)) is more than the RVEs with lower aggregate volume fraction (see Figure 4.19 (e)), because the model with higher aggregate volume fraction (Figure 4.19 (e)) had smaller particles and larger surface area of ITZ.

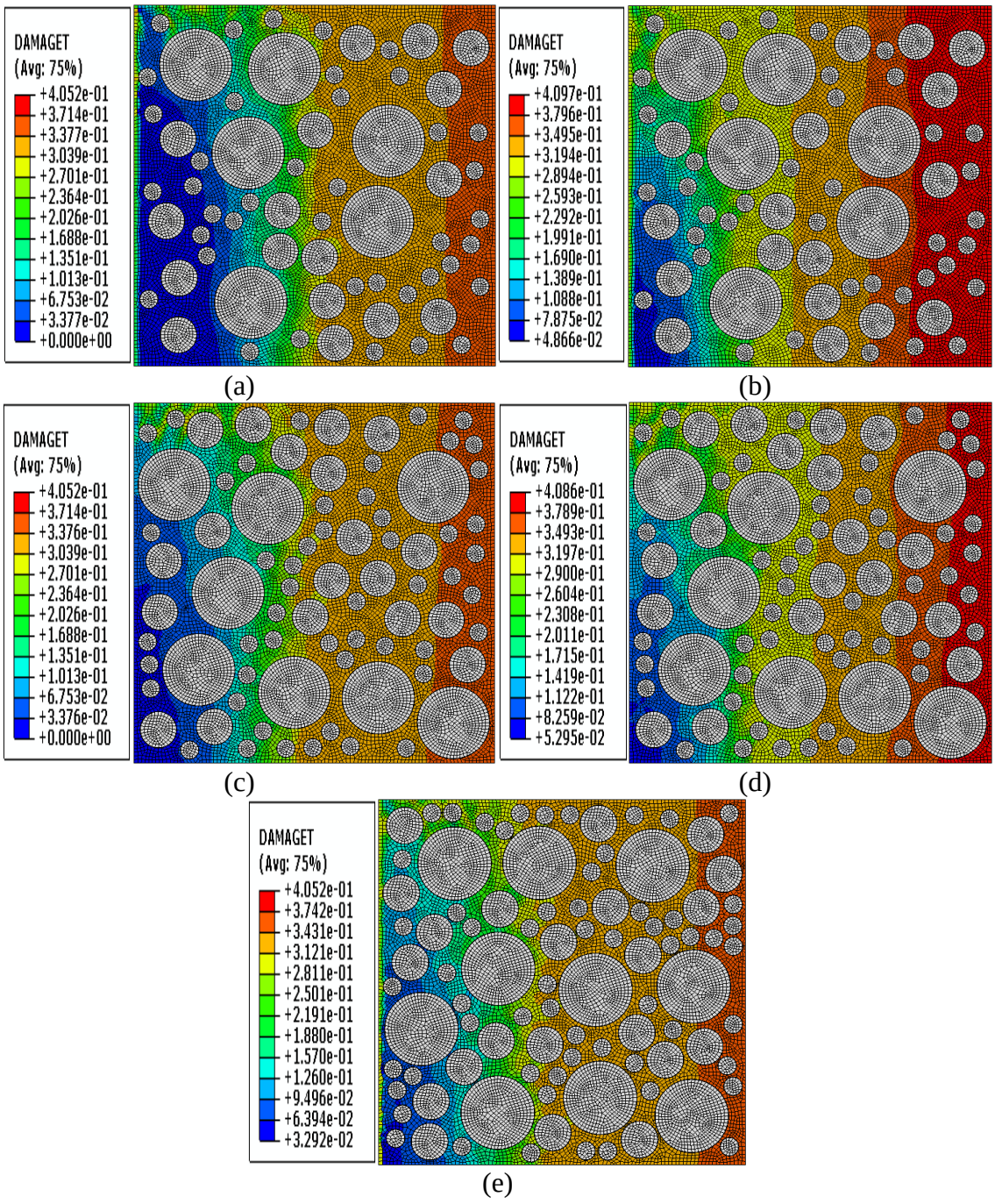

Figure 4.19 Tensile damage for different volume fraction values: (a) VF = 40% at T= -60°C, (b) VF = 40% at T= -100°C, (c) VF = 50% at T= -60°C, (d) VF = 50% at T= -80°C, and (e) VF = 60% at T= -60°C.

The Von Mises stresses and maximum principle stresses values using transient analysis for different volume faction effect are shown in Figure 4.20 and Figure 4.21 respectively.

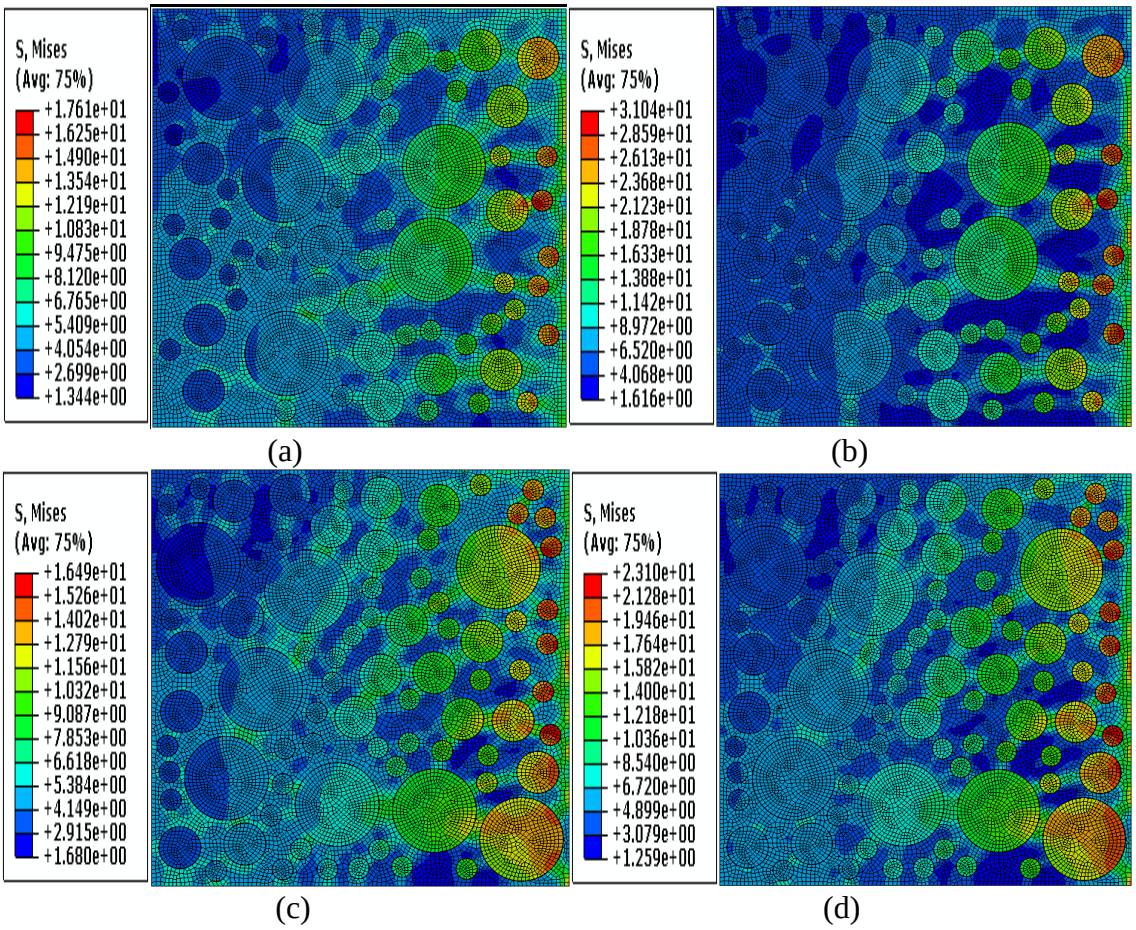

Figure 4.20 Von Mises stresses for different volume fraction values: (a) VF = 40% at T= -60°C, (b) VF = 40% at T= -100°C, (c) VF = 50% at T= -60°C, (d) VF = 50% at T= -80°C, and (e) VF = 60% at T= -60°C.

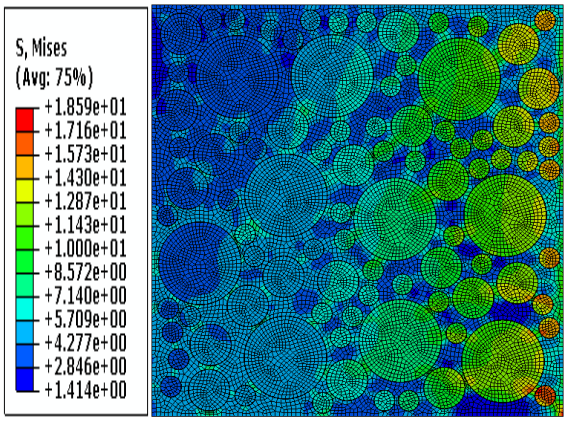

(e)

Figure 4.20 Continued.

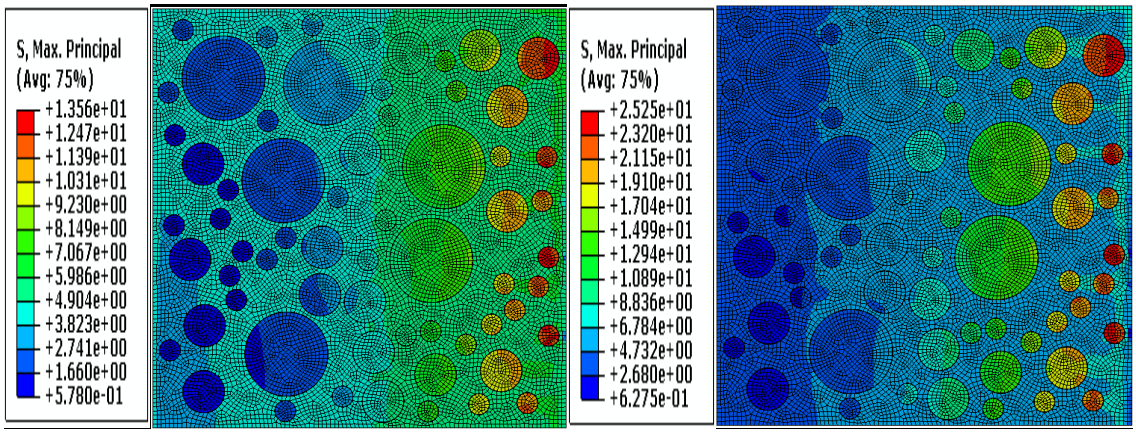

(a) (b)

Figure 4.21 Maximum Principle stresses for different volume fraction values: (a) VF = 40% at T= -60°C, (b) VF = 40% at T= -100°C, (c) VF = 50% at T= -60°C, (d) VF = 50% at T= -80°C, and (e) VF = 60% at T= -60°C.

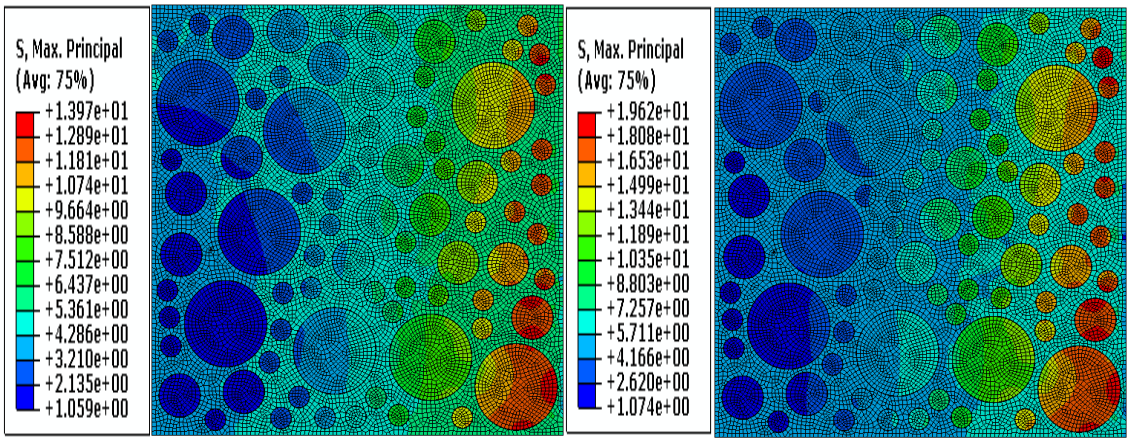

(c) (d)

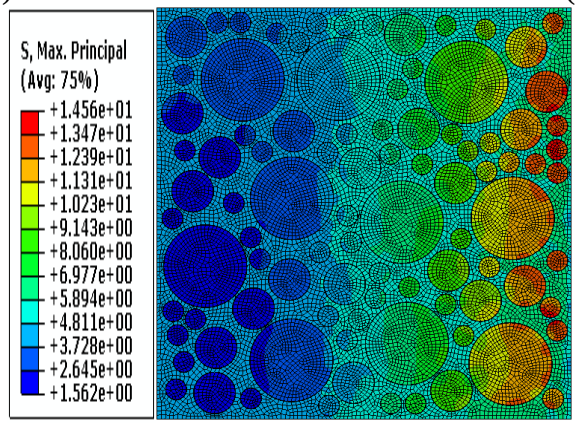

(e)

Figure 4.21 Continued.

4.3.3 The Effect of Coefficient of Thermal Expansion

The results in Table 4.9 show that the increase in the difference in the CTE made the concrete sustain less reduction in temperature. The finding confirms the results from the steady state analysis that less difference in CTE gives less damage in concrete. The difference between aggregate and matrix CTE is the major effect on increasing damage in the model in the steady state analysis as shown in Figure 4.9. In transient analysis, the number of element which has zero damage density in Figure 4.22 (a) was more than the

other RVEs at the same temperature of -60°C. The elements in Figure 4.22 can resist the damage more because the difference between the aggregate and matrix CTE is lower. However, the number of elements that has high damage values in the right side of RVE in Figure 4.22 (b) increased because the temperature decreased.

Table 4.9 Minimum temperature and tensile damage values due to CTE effect for transient analysis.

RVE	Aggregate CTE α (1/°C)	Mortar CTE α (1/°C)	Minimum temperature (°C)	Tensile damage range at minimum temperature
1	6×10^{-6}	10×10^{-6}	-80	0.405
2	8×10^{-6}	15×10^{-6}	-70	0.405
3	6×10^{-6}	15×10^{-6}	-60	0.405

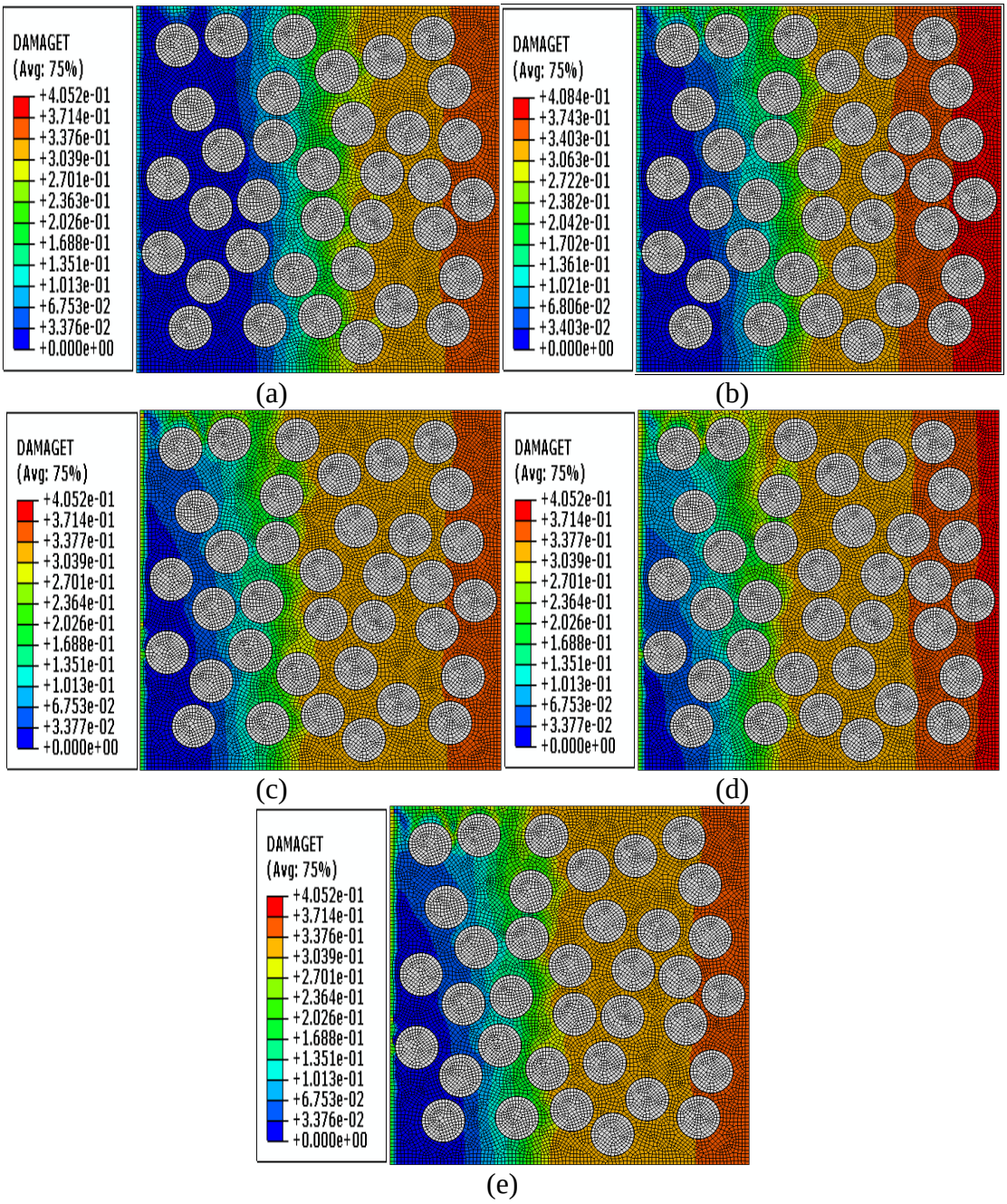

Figure 4.22 Tensile damage for different CTEs: (a) aggregate CTE= 6×10^{-6}°C^{-1} and mortar CTE= 10×10^{-6}°C^{-1} at T= -60°C, (b) aggregate CTE= 6×10^{-6}°C^{-1} and mortar CTE= 10×10^{-6}°C^{-1} at T= -80°C, (c) aggregate CTE= 8×10^{-6}°C^{-1} and mortar CTE= 15×10^{-6}°C^{-1} at T= -60°C, (d) aggregate CTE= 8×10^{-6}°C^{-1} and mortar CTE= 15×10^{-6}°C^{-1} at T= -70°C, (e) aggregate CTE= 6×10^{-6}°C^{-1} and mortar CTE= 15×10^{-6}°C^{-1} at T= -60°C.

The Von Mises stresses and maximum principle stresses values using transient analysis for RVEs with different CTE value of aggregate and matrix effect are shown in Figure 4.23 and Figure 4.24 respectively.

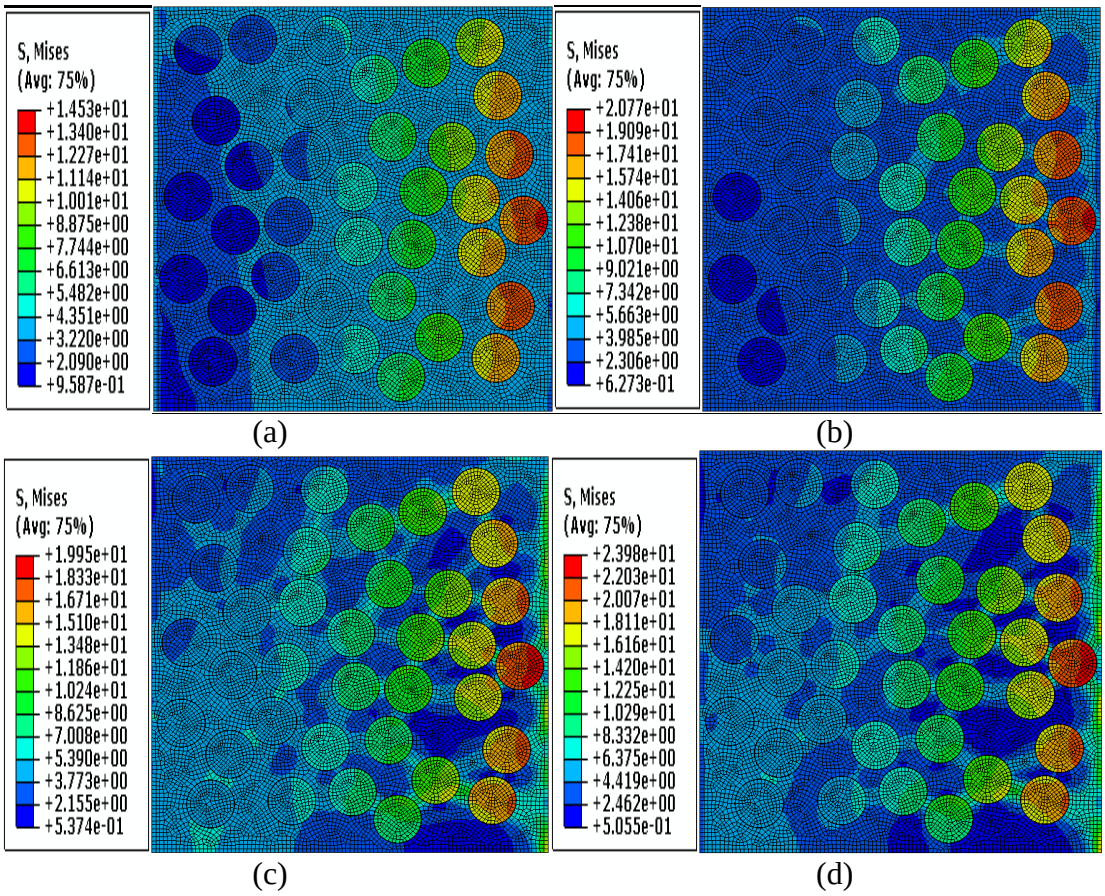

Figure 4.23 Von Mises for different CTEs: (a) aggregate CTE= 6×10^{-6}°C^{-1} and mortar CTE= 10×10^{-6}°C^{-1} at T= -60°C, (b) aggregate CTE= 6×10^{-6}°C^{-1} and mortar CTE= 10×10^{-6}°C^{-1} at T= -80°C, (c) aggregate CTE= 8×10^{-6}°C^{-1} and mortar CTE= 15×10^{-6}°C^{-1} at T= -60°C, (d) aggregate CTE= 8×10^{-6}°C^{-1} and mortar CTE= 15×10^{-6}°C^{-1} at T= -70°C, (e) aggregate CTE= 6×10^{-6}°C^{-1} and mortar CTE= 15×10^{-6}°C^{-1} at T= -60°C.

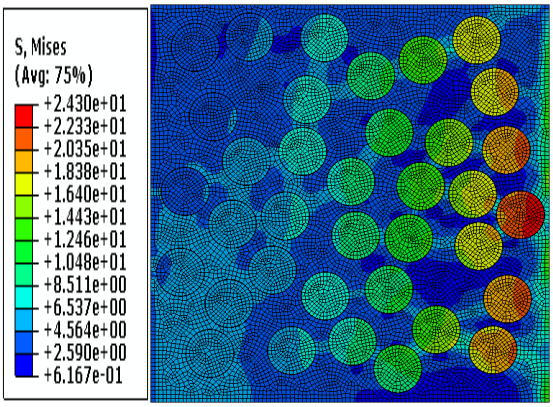

(e)

Figure 4.23 Continued.

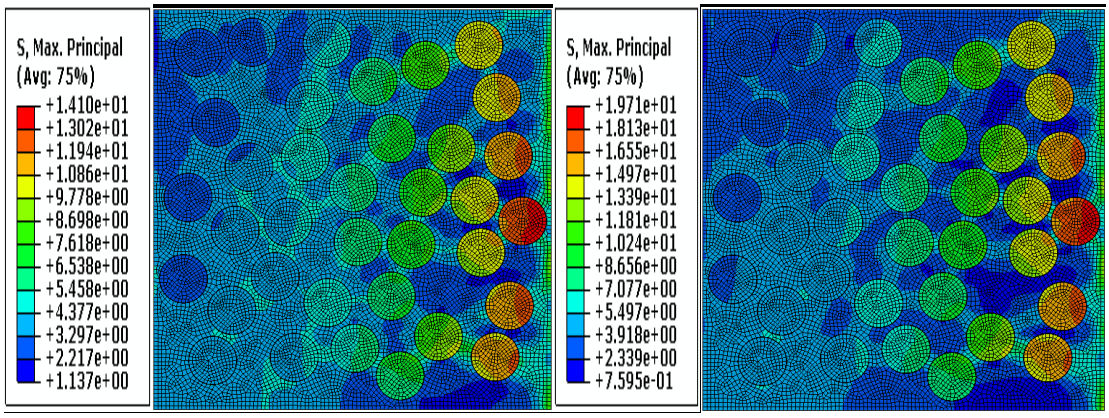

(a) (b)

Figure 4.24 Maximum Principle stresses for different CTEs: (a) aggregate CTE= 6×10^{-6}°C^{-1} and mortar CTE=10×10^{-6}°C^{-1} at T= -60°C, (b) aggregate CTE=6×10^{-6}°C^{-1} and mortar CTE=10×10^{-6}°C^{-1} at T= -80°C, (c) aggregate CTE=8×10^{-6}°C^{-1} and mortar CTE=15×10^{-6}°C^{-1} at T= -60°C, (d) aggregate CTE=8×10^{-6}°C^{-1} and mortar CTE= 15×10^{-6}°C^{-1} at T= -70°C, (e) aggregate CTE=6×10^{-6}°C^{-1} and mortar CTE=15×10^{-6}°C^{-1} at T= -60°C.

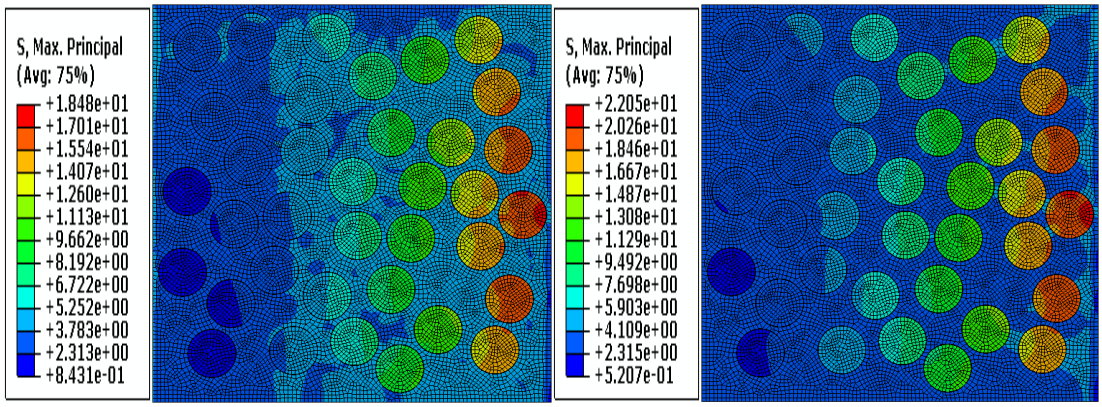

(c) (d)

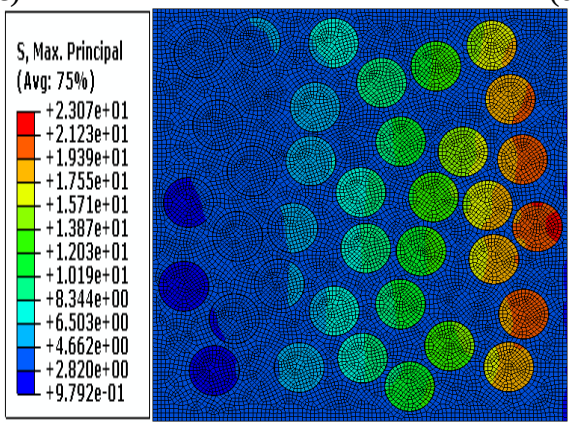

(e)

Figure 4.24 Continued.

4.4 Summary

The results in this chapter focused on the evaluation of the effects of aggregate size, volume fraction, and coefficient of thermal expansion on the behavior of concrete subjected to cryogenic temperatures. The concrete damage model presented in Chapter II was used to represent the matrix and ITZ, while the aggregate particles are modeled as elastic. The results show the difference in the coefficient of thermal expansion between the aggregate and matrix was the most important factor that influences damage due to cryogenic temperatures. Aggregate size and volume fraction had much less effects on

damage. The post-tensile yield or post-damage behavior had significant effect on damage density and distribution. However, there are no measurements of this behavior at cold temperatures in the literature. It is recommended to conduct experiment to better characterize this behavior and include accurate representation of it in the modeling efforts. This chapter used idealized, circular shape particles. The following chapter will include actual images of the concrete microstructure to develop the meso-scale model.

CHAPTER V

VALIDATION USING ANALYSIS OF CONCRETE MESO-SCALE MODEL

5.1 Introduction

The modeling approach and analysis presented in this chapter are similar to those in Chapter IV. However, a model of internal structure of a concrete specimen is used in the meso-scale model developed in this chapter. The analysis in this chapter uses the steady-state temperature boundary conditions and it focuses on the effect of CTE values on concrete damage. Moreover, it examines the effects of changes in CTE as a function of temperature versus the use of a constant, positive value of CTE. The change of CTE was modeled to represent the case of non-air entrained concrete in which the CTE of mortar changes from a positive value to a negative value or remains negative for the whole range of temperatures. The negative CTE value represents contraction of mortar with a decrease in temperature. The change in the coefficients of thermal expansion of different concrete conditions (moisture content and air entrainment) is illustrated in Opara (2007) (see Figure 5.1).

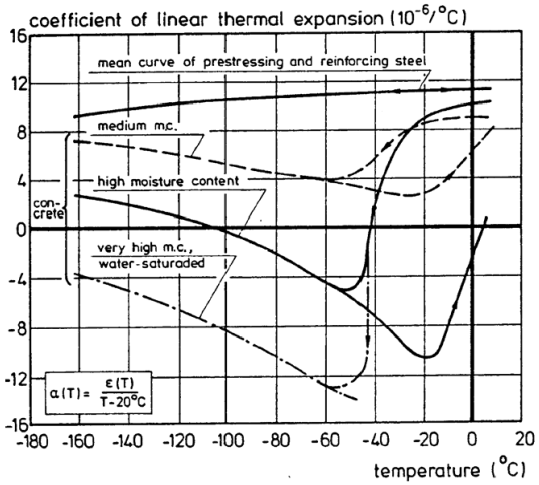

Figure 5.1 The coefficient of thermal expansions of concrete with different degree of saturation (Krstulovic-Opara, 2007).

5.2 Concrete Internal Structure

Chapter IV included the investigation of the concrete sensitivity to coefficient of thermal expansion and volume fraction of circular shape aggregates. This chapter uses irregular shape aggregates with size and distribution similar to real concrete internal structure in the meso-scale model as shown in Figure 5.2 (Wang, et al., 1999). This image is of a concrete internal structure is drawn using AutoCAD and imported to ABAQUS to generate with the finite element mesh with a cross section of 100 mm × 100 mm (see Figure 5.2). The aggregate volume fraction is 50%. The main features of these polygonal angular aggregates that their sizes are chosen with consideration of the sieve analysis and a minimum thickness of mortar can coat them (Wang, et al., 1999).

Figure 5.2 Concrete internal micro-structure (random aggregate model) (Wang, et al., 1999).

5.3 Use of Constant Values of CTE (Air Entrained Concrete)

The mixtures for air entrained concrete specimens represented in this section are shown in Table 5.1. The CTEs listed in Table 5.1 are used to analyze damage in the concrete internal structure. The CTE values in Tables 5.1 and 5.3 are based on knowledge and published values of the properties of various aggregate types and mortars. The model is initially subjected to a temperature of 20 ^{o}C and then the whole temperature is reduced to -160 ^{o}C. This case represents a rapid cooling of a concrete specimen. This is the "steady state analysis" described in Chapter IV.

Table 5.1 The mixtures for air entrained concrete specimens (Mukhopadhyay and Zollinger, 2009; Lukefahr and Du, 2010).

RVE	CA aggregate	FA in mortar	CTE CA 10^{-6} (1/°C)	Air-Entrainment	CTE mortar 10^{-6} (1/°C)
RVE1	Lightweight	N Siliceous	5-6	Yes	10
RVE2	Hanson Limestone	N Siliceous	6.5-8	Yes	15
RVE3	Hanson Limestone	N Siliceous	6.5-8	Yes	15

Table 5.2 Minimum temperature and tensile damage values due to CTE effect in air entrained concrete.

RVE	Aggregate CTE α (1/°C)	Mortar CTE α (1/°C)	Minimum temperature (°C)	Tensile damage range at minimum temperature	Tensile damage range at temperature -30°C
1	6×10^{-6}	10×10^{-6}	-160	0.448 - 0.705	0.214 - 0.400
2	8×10^{-6}	15×10^{-6}	-47	0.350 - 0.711	0.296 - 0.592
3	6×10^{-6}	15×10^{-6}	-30	0.270 - 0.804	0.270 - 0.804

Comparing the results in Table 5.2 with those in Table 4.6 shows that the damage is higher in the model of concrete internal structure than the model with circular particles. In addition, the idealized shape model was able to sustain lower temperatures. For example, the minimum temperature value was -160 °C in RVE 2 in Table 4.6 while it was -47 °C in Table 5.2. This means that the aggregate shape has significant effect on the damage and the temperature values the model can sustain more before reaching the

damaged states. The ultimate tensile strength of specimens with circular aggregates is higher than specimens with more irregular shape aggregates because of the higher stress concentrations that are generated at the sharp edges of aggregates; these high stresses induce more damage (Du and Sun, 2007).

Figures 5.3(a) and (b) show that the damage is distributed in the whole RVE. Figure 5.3(c) shows that damage occurred in the whole specimen while the temperature did not drop below -30 ^{o}C. Figure 5.4(a) also shows that the model with the least difference in CTE has the least Von Misses stresses in the mortar phase. These results emphasize that the difference between CTE values of aggregate and mortar has significant role in concrete damage resistance and durability at low temperatures. Callan (1952) found that the concrete durability effected by the difference in CTE of aggregate and mortar and recommended that the difference in CTE between mortar and aggregate should not exceed $5.4\times10^{-6}{}^{\circ}\mathrm{C}^{-1}$ (Callan, 1952).

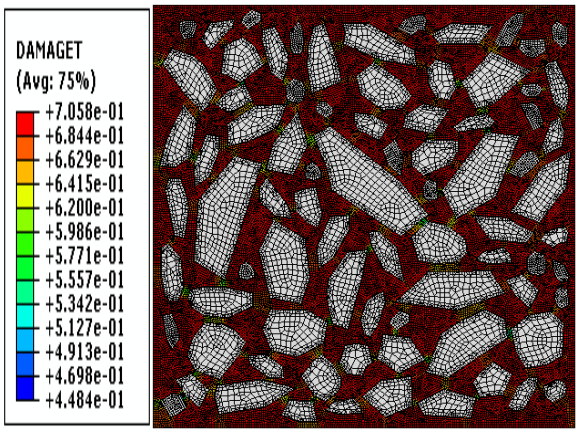

(a)

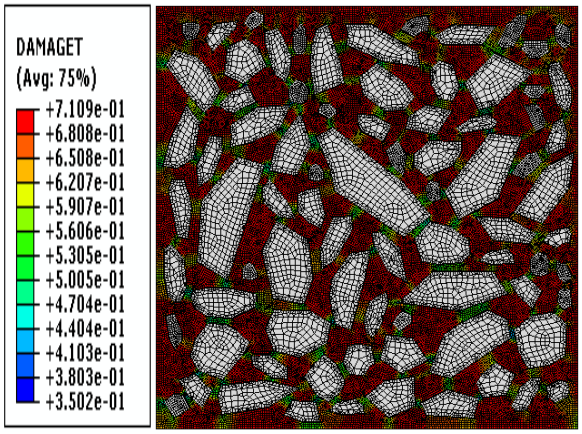

(b)

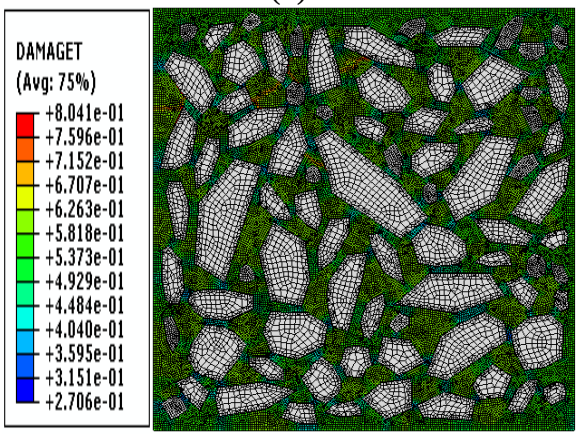

(c)

Figure 5.3 Tensile damage for different CTEs: (a) aggregate CTE= 6×10^{-6}°C^{-1} and mortar CTE= 10×10^{-6}°C^{-1} at T= -160°C, (b) aggregate CTE= 8×10^{-6}°C^{-1} and mortar CTE= 15×10^{-6}°C^{-1} at T= -47°C, and (c) aggregate CTE= 6×10^{-6}°C^{-1} and mortar CTE= 15×10^{-6}°C^{-1} at T= -30°C.

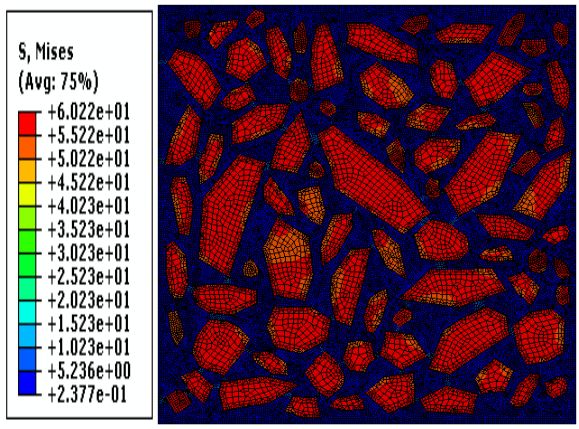

(a)

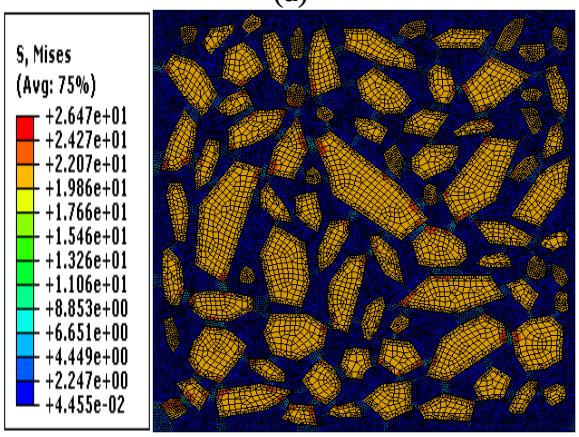

(b)

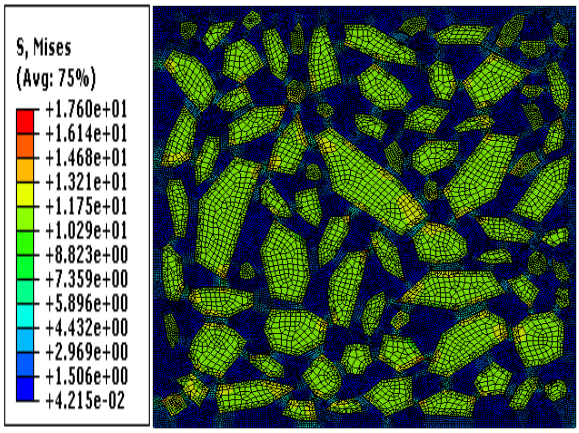

(c)

Figure 5.4 Von Mises for different CTEs: (a) aggregate CTE= 6×10^{-6}°C^{-1} and mortar CTE= 10×10^{-6}°C^{-1} at T= -160°C, (b) aggregate CTE= 8×10^{-6}°C^{-1} and mortar CTE= 15×10^{-6}°C^{-1} at T= -47°C, and (c) aggregate CTE= 6×10^{-6}°C^{-1} and mortar CTE= 15×10^{-6}°C^{-1} at T= -30°C.

5.4 Effect of Changes of CTE as a Function of Temperature (Non-Air Entrained Concrete)

Rahman (2013) developed a model based on poro-elasticity theory to calculate the CTE values of mortar and concrete. In addition, this model calculates stress, strain and pore pressure with time at different locations in concrete model that consists of with an aggregate core surrounded by a matrix sphere. The governing equation for pore pressure is solved in the Laplace Transformed domain to model the deformations in concrete that occurs due to freezing effect and pressure. These equations are modified to determine the stress and strain fields in concrete caused by the porous aggregates under freeze-thaw cycles. These equations are then inverted to time domain using Stehfest Algorithm (Rahman and Grasley, 2013).

The model by Rahman and Grasley (2013) was used to calculate the change in CTE as a function of temperature for non-air entrained concrete. The non-air entrained concrete needs aggregates with low permeability and porosity to increase concrete frost resistance and to decrease the internal pressure due to ice formation in pores (Verbeck and Landgren, 1960). Therefore, the concrete specimen that is modeled in this section consists of Traprock coarse aggregates with low porosity, low permeability, and high strength properties. The mortar included siliceous fine aggregates. The specifications in the code of American Concrete Institute (ACI) for liquefied natural gas tank (LNG) are taken into consideration in order to determine the characteristics of the non-air entrained concrete specimens. The concrete compressive strength at 28-days is 40 MPa and the water to cement ratio is 0.42. In addition, the ACI code recommends adding some

admixture to concrete such as fly ash or slag-cement to reduce permeability and increase durability (ACI.376-10, 2010).

The model was used to determine CTEs values as functions of temperature for non-air entrained concrete and mortar with aggregate CTE = 6×10^{-6}°C^{-1} and mortar CTE=10×10^{-6}°C^{-1} at T of 20°C. The corresponding properties of the non-air entrained concrete are shown as Case 1 in Table 5.3. The input values for the model by Rahman and Grasley (2013) are given in Table 5.4, and the CTE simulation results are shown in Figure 5.5.

Table 5.3 The mixtures for non-air entrained concrete specimens (Mukhopadhyay and Zollinger, 2009).

RVE	CA aggregate	FA in mortar	CTE CA 10^{-6} (1/°C)	Air-Entrainment	CTE mortar 10^{-6} (1/°C)
Case 1	Traprock	N Siliceous	6	No	See Figure 5.5
Case 2	Traprock	N Siliceous	8	No	See Figure 5.7

Table 5.4 The input values for analytical model to find CTE values for non-air entrained concrete and mortar for Case 1.

Properties	Mortar	Aggregate
Porosity ϕ (μm)	0.25	0.05
Permeability (k)	10^{-19}	10^{-21}
Bulk Modulus (K) (GPa)	13.9	35
Maximum Pore Size R* (μm)	0.2	0.1
Pore Size Distribution (m^2)	0.5	0.5
CTEs α (1/°C) at T=20	10×10^{-6}	6×10^{-6}

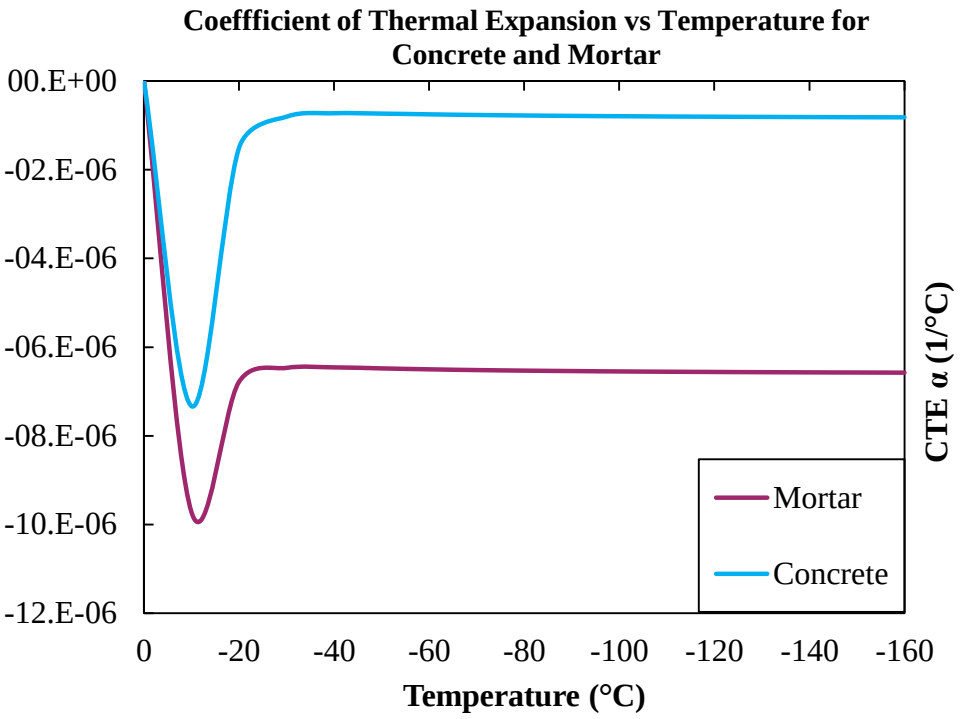

Figure 5.5 Coefficient of thermal expansion values of non-air entrained concrete specimen and mortar with aggregate CTE= 6×10^{-6}°C^{-1} and mortar CTE= 10×10^{-6}°C^{-1} at T= 20°C (Case 1).

Figure 5.5 shows that the coefficient of thermal expansion values of mortar and concrete are negative for non-entrained concrete characteristics indicating that water will expand and the whole material will expand during the cooling process. The damage results are shown in Figure 5.6. It is noticed that damage is highly localized at the interface and damage is reached at a temperature higher than the case of positive CTE values when compared with the corresponding RVE 1 in Table 5.2.

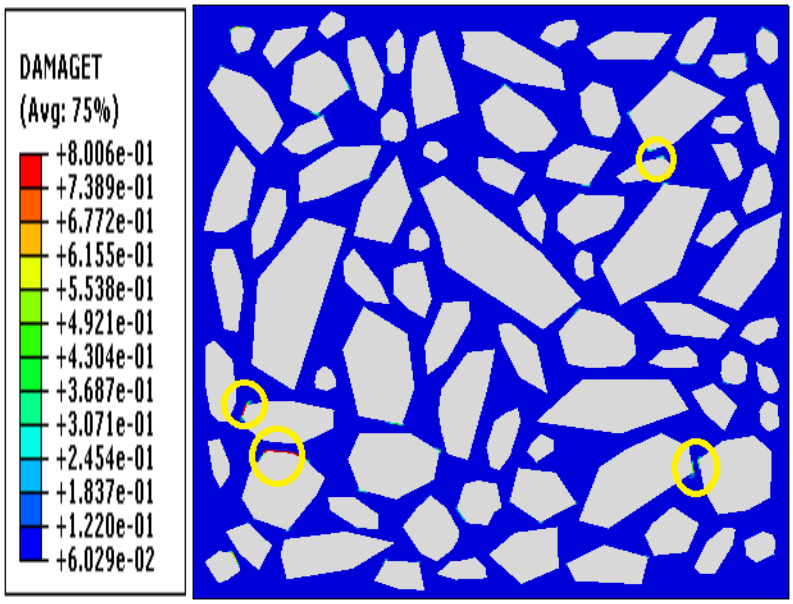

(a)

Figure 5.6 The damage in non-air entrained concrete at T= -33°C with aggregate CTE= 6×10^{-6}°C^{-1} and mortar CTE=10×10^{-6}°C^{-1} at starting T=20°C: (a) The initiation damage and (b) Magnified of cross section (Case 1).

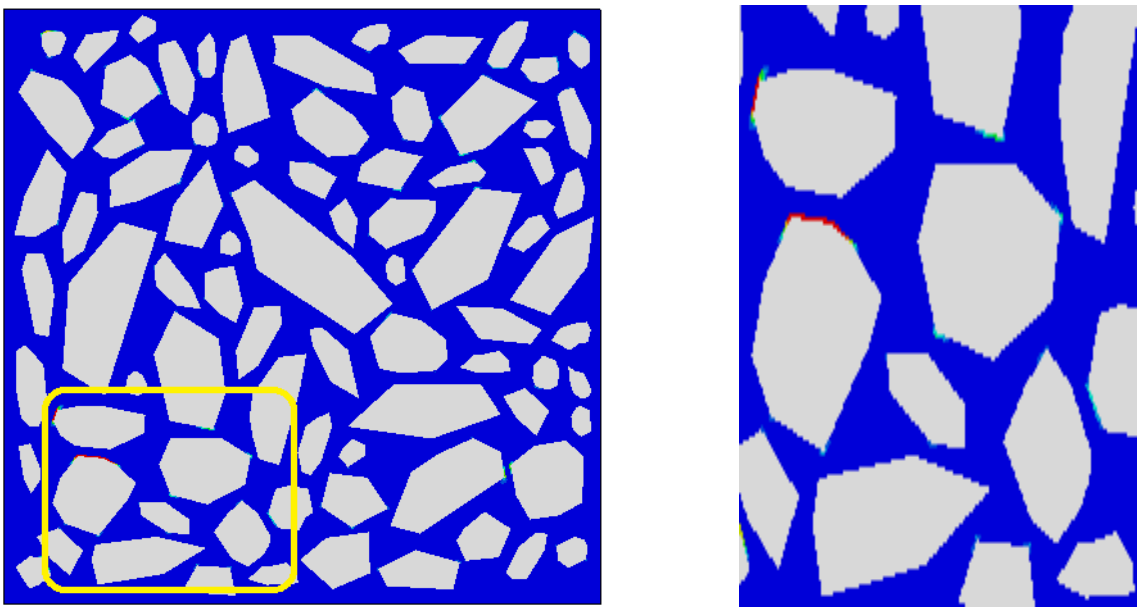

(b)

Figure 5.6 Continued.

The same analysis was repeated for CTEs values for non-air entrained concrete with aggregate CTE = 8×10^{-6}°C^{-1} and mortar CTE = 15×10^{-6}°C^{-1} at T=20°C. The model input parameters are shown in Table 5.5 while the results are shown in Figure 5.7.

Figure 5.7 shows that the coefficient of CTE of concrete changes from a negative value to a positive value with decreasing temperature. This means that concrete expands at the beginning due to ice formation and when the ice filled the pores it contracts because of the low permeability and porosity values.

Comparing Figures 5.6 and 5.8 shows that damage initiated at more points in Figure 5.8 than in Figure 5.6. In addition, damage in Figure 5.8 was reached at a higher temperature (-13°C) than the case in Figure 5.6 (-33 °C). These results emphasize that the increase in difference in CTE values of mortar and concrete causes more damage.

Table 5.5 The input values for analytical model to find CTE values for non-air entrained concrete and mortar for Case 2.

Properties	Mortar	Aggregate
Porosity ϕ (μm)	0.25	0.05
Permeability (k)	10^{-19}	10^{-21}
Bulk Modulus (K) (GPa)	13.9	35
Maximum Pore Size R* (μm)	0.2	0.1
Pore Size Distribution (m^2)	0.5	0.5
CTEs α (1/°C) at T=20	15×10^{-6}	8×10^{-6}

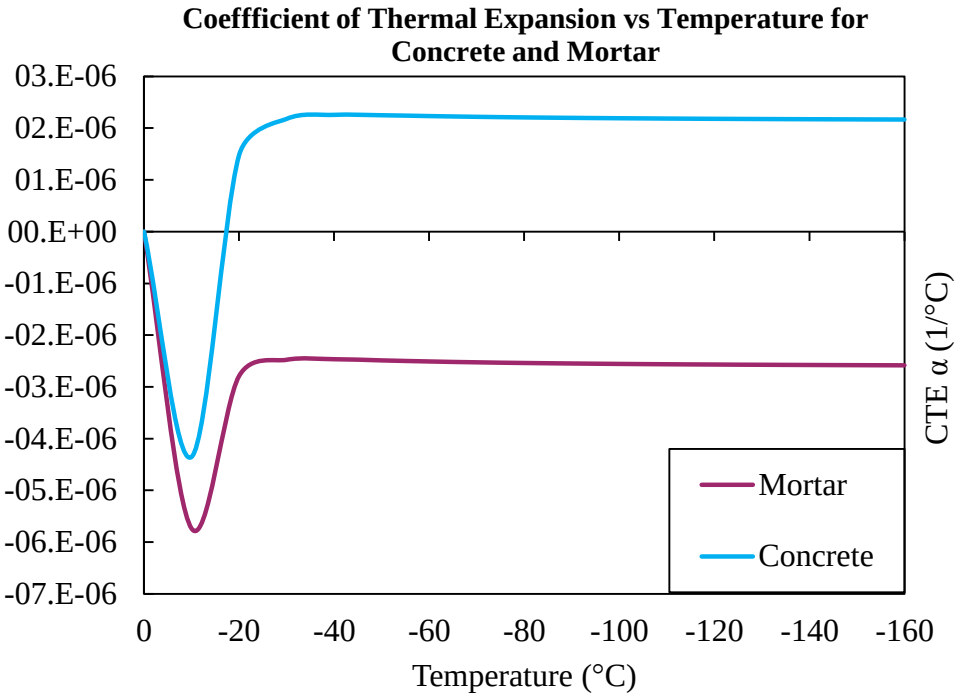

Figure 5.7 Coefficient of thermal expansion values of non-air entrained concrete specimen and mortar with aggregate CTE=8×10^{-6}°C^{-1} and mortar CTE=15×10^{-6}°C^{-1} at T= 20°C (Case 2).

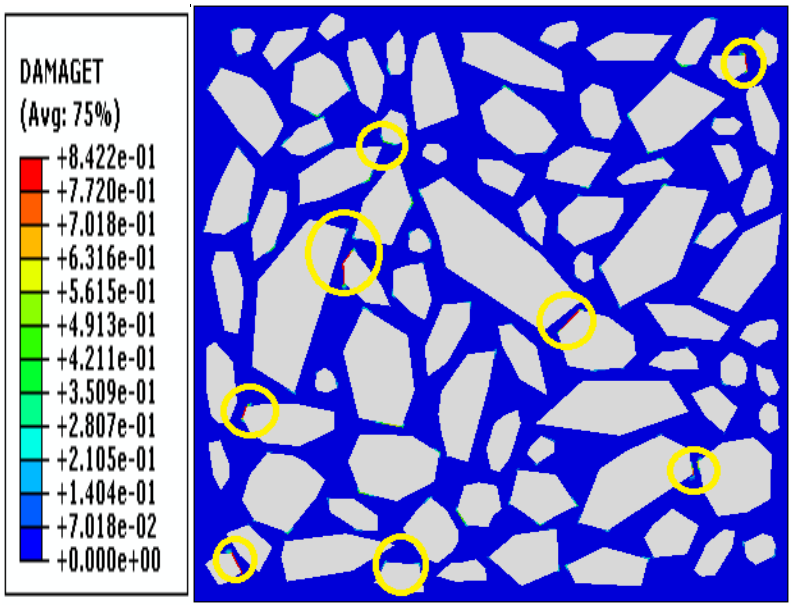

(a)

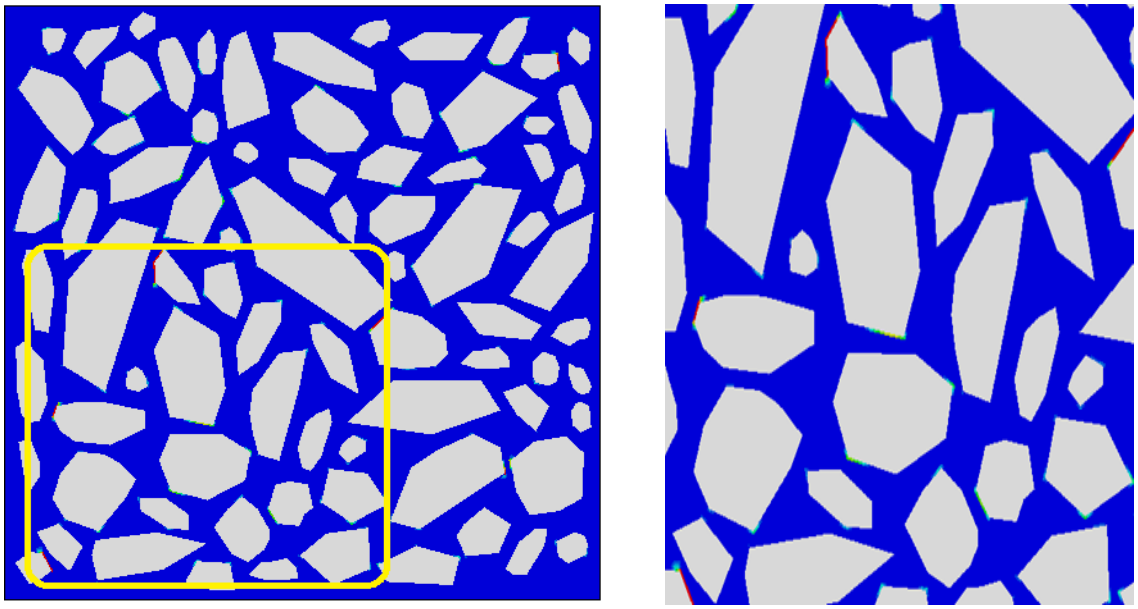

(b)

Figure 5.8 The damage in non-air entrained concrete at T= -13°C with aggregate CTE= 8×10^{-6}°C^{-1} and mortar CTE=15×10^{-6}°C^{-1} at starting T= 20°C: (a) The initiation damage and (b) Magnified of cross section (Case 2).

The Von Mises stresses for the two non- air entrained concrete cases shown in Figure 5.9.

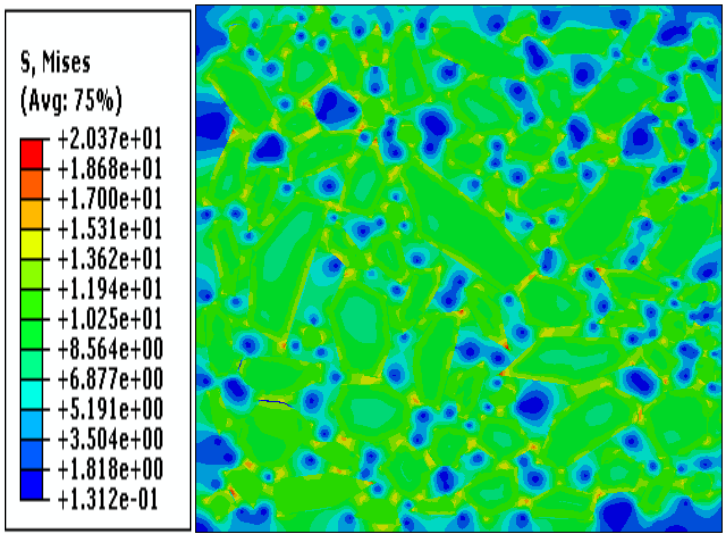

(a)

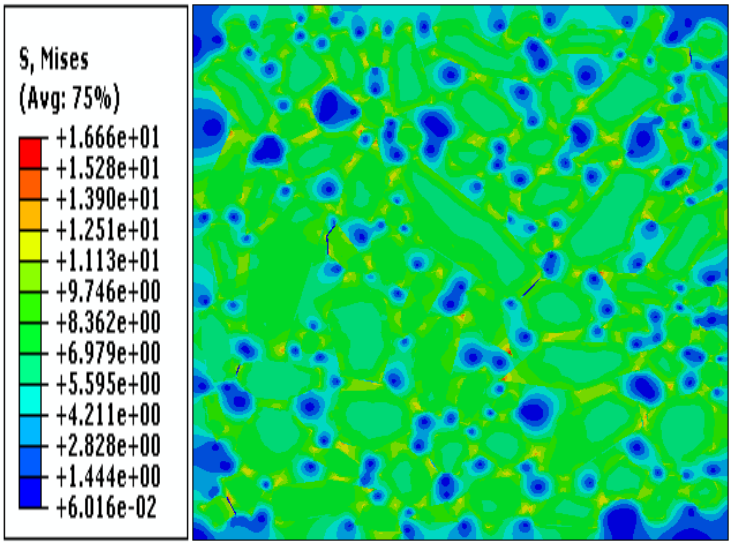

(b)

Figure 5.9 The stress in non-air entrained concrete: (a) aggregate CTE=6×10^{-6}°C^{-1} and mortar CTE=10×10^{-6}°C^{-1} at starting T= 20°C (Case 1) (b) aggregate CTE=8×10^{-6}°C^{-1} and mortar CTE=15×10^{-6}°C^{-1} at starting T=20°C (Case 2).

5.5 Evaluation of Sensibility of Model Results

The model results presented in the previous sections are evaluated in this section based on results published by Callen (1952). Callan (1952) found that concrete durability subjected to freezing-thawing cycles decreased as the difference of CTE between coarse aggregates and mortar increased. Figure 5.10 shows that concrete consists of limestone coarse aggregates and limestone sand mortar has higher durability (relative dynamic modulus of elasticity (DFE)) than concrete prepared using different types of aggregates such as concrete with limestone coarse aggregates and silica sand mortar. The dynamic modulus of elasticity was determined by sonic method after 300 freezing-thawing cycles. Callan (1952) concluded that the factor which plays the main role in concrete durability is the difference in CTE between concrete components. This difference causes high stresses at the ITZ zone.

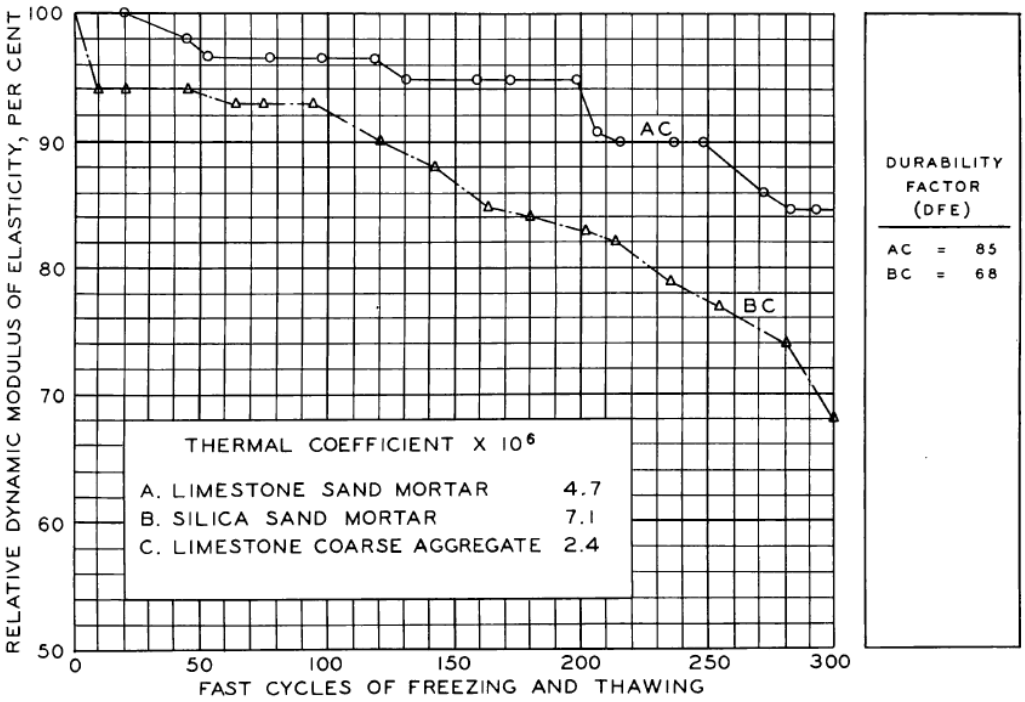

Figure 5.10 Freezing and thawing test results for concrete specimens containing limestone coarse aggregate (Callan, 1952).

Callan (1952) plotted difference in CTEs of mortar and coarse aggregates on durability factors (DFE) for 78 concrete mixtures as shown in Table 5.6 and Figure 5.11. The x-axis in Figure 5.11 is the difference in the CTE between the aggregate and mortar and the y-axis is the DFE. The calucaltion of 100% minus the durability factor (100-DFE) gives an indication of damage. Therefore, Figure 5.12 shows (100-DFE)/100 for 78 concrete mixtures from Callan (1952) and compared with the maximum damage calculated using the model for the mixtures presented in the previous section. Figure 5.12 shows that the model gives the correct trend for the effect of difference in CTE on damage. Since the mixtures used in the model are different than the mixtures in the

study by Callan (1952), it is not expected that the experimental damage values would match the model results. But, the trends from the model follow the trend from the experimental measurements. Callen (1952) reported that the volume of sand to the total volume of aggregate was between 0.34 and 0.42. Therefore, it is determined based on assuming reasonable values of concrete volumetrics that the volume of aggregate was in the range of 0.4 – 0.46.

$$\frac{\text{Vol}_{sa}}{\text{Vol}_{sa} + \text{Vol}_{ca}} = 0.38 \tag{5.1}$$

where Vol_{sa} is volume of sand and Vol_{ca} is volume of coarse aggregate.

$$\text{Vol}_{sa} = \frac{\text{W}_{sa}}{\gamma_w \times \text{BSG}_{sa}} \qquad \text{Vol}_{ca} = \frac{\text{W}_{ca}}{\gamma_w \times \text{BSG}_{ca}} \tag{5.2}$$

where W_{sa} is weight of sand = 1100-1300 lb/ft^3, W_{ca} is weight of coarse aggregate, BSG_{sa} is bulk specific gravity for sand = 2.6 , and BSG_{ca} is bulk specific gravity for coarse aggregate.

Volume fraction % = solid (S) % $\times$ coarse aggregate factor (CAF) (5.3)

$$\text{CAF} = \frac{\text{Loose Vol}_{ca}}{\text{Total Vol (V)}} = \frac{\text{W}_{ca}}{\text{V} \times \text{Dry rodded unit weight (DRUW)}} \tag{5.4}$$

$$\text{S\%} = \frac{\text{Dry rodded unit weight (DRUW)}}{\gamma_w \times \text{BSG}_{ca}} \tag{5.5}$$

where γ_w is unit weight of water= 62.4 lb/ft^3.

$$\text{Vol}_{sa} = 0.38\text{Vol}_{ca} + 0.38\text{Vol}_{sa} \tag{5.6}$$

$$\text{Vol}_{sa}\frac{(1-0.38)}{0.38} = \text{Vol}_{ca} = \frac{\text{W}_{ca}}{\gamma_w \times \text{BSG}_{ca}} \tag{5.7}$$

Solving Eq.(5.7) for W_{ca} as follows:

$$W_{ca} = \gamma_w \times BSG_{ca} \times Vol_{sa} \frac{(1-0.39)}{0.39} \tag{5.8}$$

By substituting Eq (5.8) in Eq (5.4), then by substituting Eqs. (5.4) and (5.5) in Eq. (5.3) yield the following:

$$\text{Volume fraction \%} = \frac{Vol_{sa} \dfrac{(1-0.39)}{0.39}}{V} = \frac{\dfrac{W_{sa}}{\gamma_w \times BSG_{sa}} \dfrac{(1-0.39)}{0.39}}{V}$$

Using W_{sa} =1100 lb/ft^3 and V standard volume = 27 ft^3, then the volume fraction equal:

$$\text{Volume fraction \%} = \frac{\dfrac{W_{sa}}{\gamma_w \times BSG_{sa}} \dfrac{(1-0.39)}{0.39}}{V} = \frac{\dfrac{1100}{62.4 \times 2.6} \dfrac{(1-0.39)}{0.39}}{27} = 0.4$$

Using W_{sa} =1300 lb/ft^3 and V standard volume = 27 ft^3, then the volume fraction equal:

$$\text{Volume fraction \%} = \frac{\dfrac{W_{sa}}{\gamma_w \times BSG_{sa}} \dfrac{(1-0.39)}{0.39}}{V} = \frac{\dfrac{1300}{62.4 \times 2.6} \dfrac{(1-0.39)}{0.39}}{27} = 0.46$$

The volume fraction for Callen (1952) concrete specimens between 0.4 - 0.46.

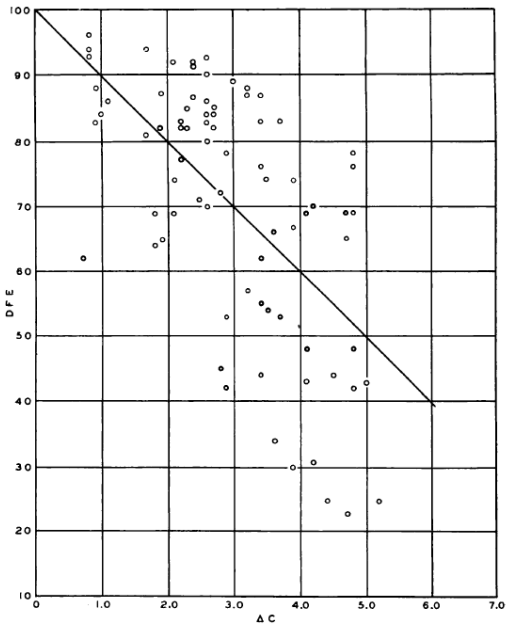

Figure 5.11 Relation between durability factors (DFE) of 78 concrete mixtures exposed to laboratory freezing and thawing and the differences between CTEs of coarse aggregate and mortar (Δc) (Callan, 1952)

Table 5.6 Aggregate combinations tested by freezing and thawing of concrete specimens (Callan, 1952).

Fine aggregate*	Coarse aggregate†	Δc‡	*DFE*	Fine aggregate*	Coarse aggregate†	Δc‡	*DFE*
a—Combinations tested in concrete after 9-day curing at 70 F							
§6. Limestone	**20. Trap rock	0.8	96	2. Limestone	10. Limestone	2.1	74
8. Limestone	20. Trap rock	0.8	94	21. Siliceous	9. Limestone	3.5	74
20. Syenite	20. Trap rock	1.7	94	23. Siliceous	6. Limestone	3.9	74
7. Limestone	20. Trap rock	0.8	93	16. Limestone	10. Limestone	2.8	72
14. Limestone	7. Limestone	2.6	93	16. Limestone	14. Limestone	2.5	71
15. Limestone	18. Limestone	2.1	92	3. Limestone	1. Limestone	2.6	70
7. Limestone	8. Limestone	2.4	92	29. Siliceous	18. Limestone	4.2	70
8. Limestone	9. Limestone	2.4	92	1. Limestone	14. Limestone	1.8	69
9. Limestone	6. Limestone	2.6	90	1. Limestone	10. Limestone	2.1	69
28. Siliceous	19. Syenite	3.0	89	27. Siliceous	12. Limestone	4.1	69
12. Limestone	20. Limestone	0.9	88	29. Siliceous	11. Limestone	4.7	69
23. Siliceous	17. Limestone	3.2	88	28. Siliceous	3. Limestone	4.8	69
20. Syenite	19. Syenite	1.9	87	26. Siliceous	7. Limestone	3.9	67
12. Limestone	12. Limestone	2.4	87	26. Siliceous	16. Limestone	3.6	66
19. Glacial	7. Limestone	3.2	87	28. Siliceous	21. Limestone	1.9	65
29. Siliceous	19. Syenite	3.4	87	29. Siliceous	12. Limestone	4.7	65
15. Limestone	20. Trap rock	1.1	86	2. Limestone	14. Limestone	1.8	64
17. Limestone	17. Limestone	2.6	86	24. Siliceous	22. Quartzite	0.7	62
6. Limestone	11. Limestone	2.3	85	18. Glacial	6. Limestone	3.4	62
10. Limestone	5. Limestone	2.7	85	18. Glacial	7. Limestone	3.2	57
22. Limestone	21. Limestone	1.0	84	21. Siliceous	11. Limestone	3.4	55
27. Siliceous	20. Trap rock	2.6	84	24. Siliceous	15. Limestone	3.5	54
18. Glacial	17. Limestone	2.7	84	18. Glacial	16. Limestone	2.9	53
10. Limestone	20. Trap rock	0.9	83	21. Siliceous	5. Limestone	3.7	53
11. Limestone	13. Limestone	2.2	83	28. Siliceous	13. Limestone	4.1	48
5. Limestone	3. Limestone	2.6	83	28. Siliceous	1. Limestone	4.8	48
19. Glacial	6. Limestone	3.4	83	28. Siliceous	20. Trap rock	2.8	45
23. Siliceous	7. Limestone	3.7	83	26. Siliceous	17. Limestone	3.4	44
21. Siliceous	20. Trap rock	1.9	82	29. Siliceous	15. Limestone	4.5	44
13. Limestone	16. Limestone	2.2	82	26. Siliceous	6. Limestone	4.1	43
25. Siliceous	20. Trap rock	2.3	82	29. Siliceous	5. Limestone	5.0	43
19. Glacial	17. Limestone	2.7	82	21. Siliceous	18. Limestone	2.9	42
29. Siliceous	22. Quartzite	1.7	81	28. Siliceous	2. Limestone	4.8	42
4. Limestone	2. Limestone	2.6	80	25. Siliceous	14. Limestone	3.6	34
19. Glacial	16. Limestone	2.9	78	24. Siliceous	4. Limestone	4.2	31
29. Siliceous	8. Limestone	4.8	78	25. Siliceous	10. Limestone	3.9	30
24. Siliceous	20. Trap rock	2.2	77	29. Siliceous	14. Limestone	4.4	25
23. Siliceous	16. Limestone	3.4	76	29. Siliceous	4. Limestone	5.2	25
29. Siliceous	9. Limestone	4.8	76	29. Siliceous	10. Limestone	4.7	23
b—Combinations tested in concrete after 21-day curing							
15. Limestone	18. Limestone	2.1	95	29. Siliceous	18. Limestone	0.8	86
7. Limestone	8. Limestone	2.4	93	29. Siliceous	9. Limestone	4.8	86
8. Limestone	20. Trap rock	0.8	93	21. Siliceous	18. Limestone	2.9	80
15. Limestone	20. Trap rock	1.1	93	21. Siliceous	9. Limestone	3.5	80
8. Limestone	9. Limestone	2.4	93	28. Siliceous	19. Syenite	3.0	79
10. Limestone	5. Limestone	2.7	93	29. Siliceous	19. Syenite	3.4	77
10. Limestone	20. Trap rock	0.9	92	20. Syenite	19. Syenite	1.9	72
7. Limestone	20. Trap rock	0.8	91	21. Siliceous	5. Limestone	3.7	70
20. Syenite	20. Trap rock	1.7	87	29. Siliceous	5. Limestone	5.0	68
11. Limestone	13. Limestone	2.2	87				

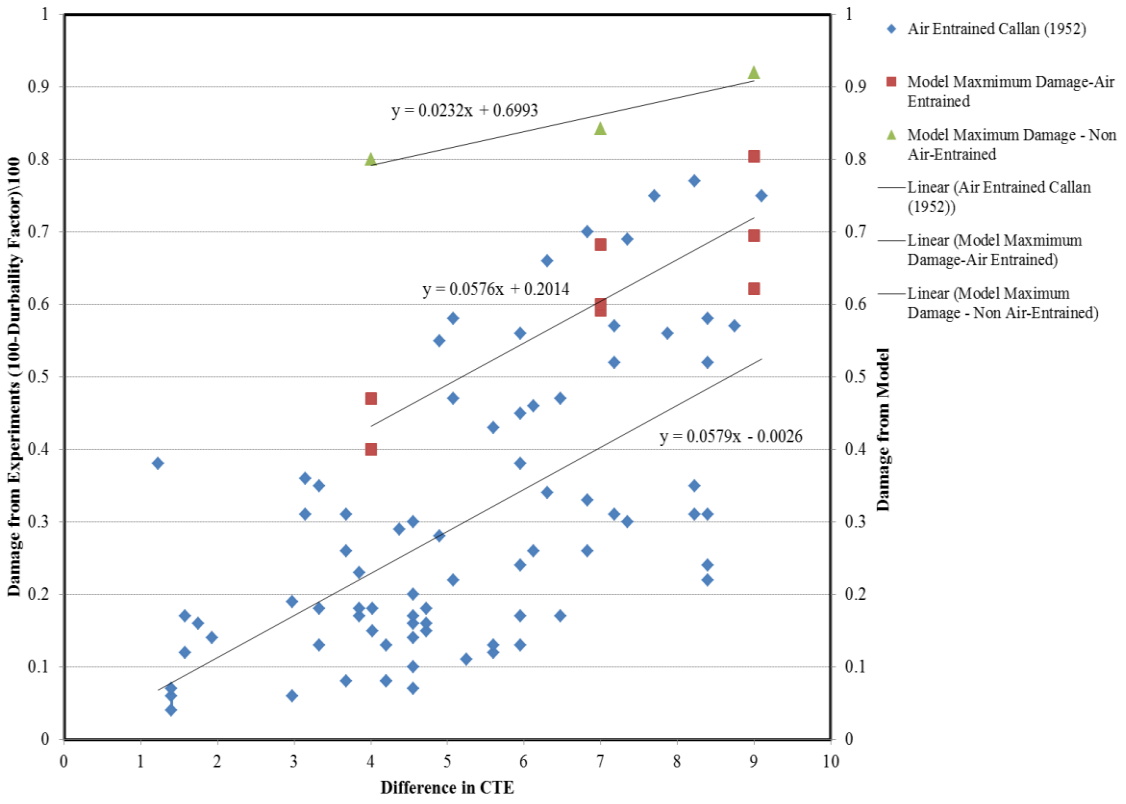

Figure 5.12 Comparison of damage calculated using the model and values measured by Callan (1952).

As discussed in Chapter II, it is well known that use of air entrainment reduce the effect of damage because of freezing (Philleo 1986; Cohen, et al., 1992). Figures 5.13 and 5.14 from Cohen et al. (1992) show the ratio of the modulus of elasticity after 300 freezing and thawing cycles to the modulus of elasticity before any freezing and thawing cycles (E_f / E_{of}). The freezing-thawing cycles were applied following ASTM C666 test, procedure A. Cohen et al. (1992) the air entrained concrete specimens passed the test requirement $E_f / E_{of} > 0.6$ (see Figure 5.13) because of the high ratio (low damage),

while the non-air entrained specimens didn't pass requirement $E_f/E_{of} \leq 0.6$ because of the low ratio (high damage). Figure 5.15 from Miura (1989) shows that the reduction in E_f/E_{of} ratio is higher for non-air entrained that cured by water than the air-entrained that cured by air. Also, the air-entrained sustain more reduction in temperature without reduction in durability factor. The model results from Figure 5.12 agree with these findings because the non ain-entrained concrete had higher damage than the air-entrained concrete.

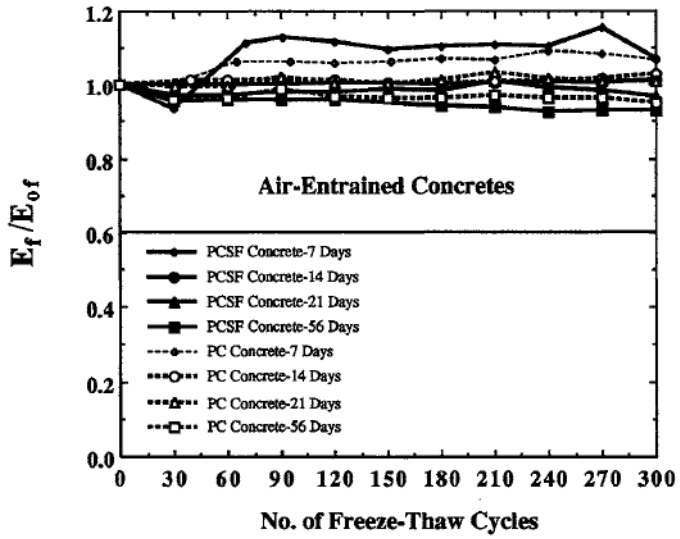

Figure 5.13 Relative resonant frequency moduli E_f/E_{of} as a function of number of freeze-thaw cycles for saturated lime-water cured air-entrained concrete mixtures (portland cement concrete with silica fume) (Cohen, et al., 1992).

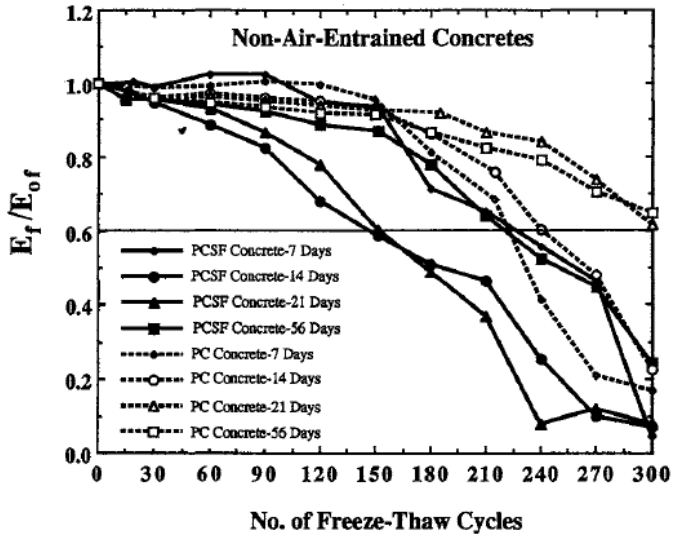

Figure 5.14 Relative resonant frequency moduli E_f/E_{of} as a function of number of freeze-thaw cycles for saturated lime-water cured non-air entrained concrete mixtures (Cohen, et al., 1992).

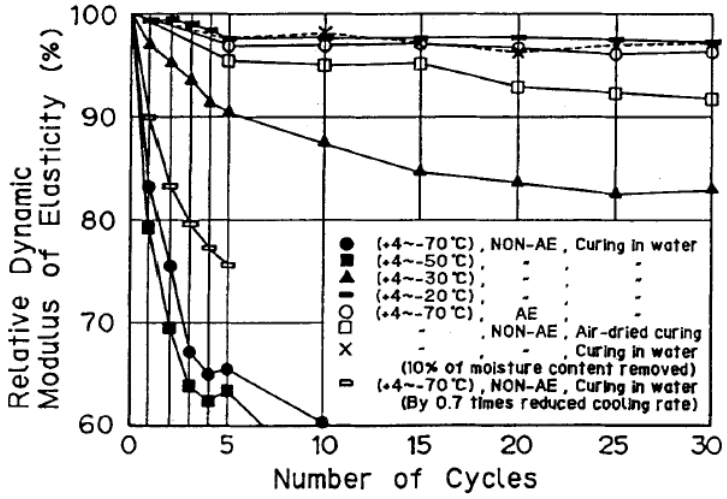

Figure 5.15 The relation between deterioration of concrete and the number of freeze-thaw cycles (Miura, 1989)

5.6 Summary

This chapter focused on the analysis and validation of the effects of coefficient of thermal expansion on concrete behavior. The meso-scale model used in this chapter resembles the concrete internal structure more than the idealized model used in Chapter IV.

The damage in the concrete meso-scale model happens earlier (at higher temperatures) than the damage in the idealized internal structure. The use of a positive CTE causes the damage to be distributed more uniformly in the mortar. However, the use of a negative value for the CTE (material expands with a decrease in temperature) causes the damage to be localized at the interface and it happens at higher temperatures. The results emphasize the importance of using air-entrained concrete (positive CTE for mortar) and also reducing the difference in CTEs of mortar and aggregate in order to reduce damage.

The damage results from the model were compared with damage values published in the literature for concrete specimens subjected to freezing temperatures. The model predicted the same trend of the effect of difference in the CTEs between mortar and aggregate as the experimental results. In addition, the model was able to predict the effect of air entrainment on reducing damage.

CHAPTER VI

CONCLUSIONS AND RECOMMENDATIONS

6.1 Conclusions

The demand for LNG has been increasing as a primary source of energy. Liquefied natural gas (LNG) should be stored at cryogenic temperatures and around the atmospheric pressure to insure safe and minimum storage volume in tanks. A typical LNG tank utilizes 9% Ni steel walls and floor for the inner containment tank; this construction method and materials are expensive. It has been proposed to use concrete as the primary containment of LNG, which means that the concrete will be in direct contact with LNG. The literature review revealed that there is a need to better understand the behavior of concrete which is in direct contact with LNG at cryogenic temperatures. More specifically the concrete behavior and potential damage are affected by the coefficient of thermal expansion values of the phases and the design of the concrete mixture.

The primary objective of this study was achieved by the development of a computational, meso-scale model to characterize and understand the potential damage growth in concrete at cryogenic temperatures down to -160°C. In this model, concrete is considered as a three-phase composite material that consists of mortar (or matrix), aggregate, and interfacial transmission zone (ITZ). The Concrete Damage Plasticity model in ABAQUS is used to represent the mortar and ITZ phases of concrete. The damage behavior of concrete was modeled using the model proposed by Abu Al-Rub

and Kim (2010). This model is suitable to represent the meso-scale behavior of the mortar and ITZ because it accounts for nonlinear change in stiffness because of damage also for permanent deformation. This model is calibrated using compressive and tensile uniaxial tests of concrete at different temperatures. Since there are no published data that describe the influence of temperatures on the post-yield or damage behavior of concrete, data were generated to represent different behavior after the damage point. The analysis involved two cases of temperature distribution:

- Case I: the whole model is initially subjected to a temperature of 20 ^{o}C and then the whole temperature is reduced to -160 ^{o}C. This case represents a rapid cooling of a concrete specimen. This analysis is referred to as the "steady state analysis".
- Case II: the model is subjected to 20 ^{o}C on the left side and -160 ^{o}C on the right side. This analysis is referred to as the "transient analysis".

The results of the idealized concrete model with circular particles showed the difference in the coefficient of thermal expansion between the aggregate and matrix was the most important factor that influences damage due to cryogenic temperatures. Aggregate size and volume fraction had much less effects on damage. The post-tensile yield or post-damage behavior had significant effect on damage density and distribution. Therefore, it is recommended to conduct experiments to better characterize this behavior and include accurate representation of it in the modeling efforts.

The analysis of Chapter V is similar to that in Chapter IV. However, the internal structure of a concrete specimen is used in the analysis. The analysis uses the steady-state temperature boundary conditions and it focuses on the effect of CTE values on concrete damage. Moreover, it examines the effects of changes in CTE as a function of temperature versus the use of a constant CTE. The change of CTE of was modeled to represent the case of non-air entrained concrete in which the CTE was modeled to change from negative to positive values with a decrease in temperature or to remain negative for the whole range of temperatures. This mortar behavior indicates expansion with further decrease in temperature.

The damage in the concrete meso-scale model happens earlier (at higher temperatures) than the damage in the idealized internal structure. The aggregate shape has significant effect on damage and the temperature values at which damage occurs. The internal structure model with circular shape particles sustains more reduction in temperature than the model with irregular shape particles before reaching the damaged state. This is attributed to the higher stress concentrations that occur at the sharp edges of angular aggregates leading to more damage at the interface. The use of a negative value for the CTE (non-air entrained mortar) causes the damage to be localized at the interface and it happens at higher temperatures.

The damage results from the model were compared with damage values published in the literature for concrete specimens subjected to freezing temperatures. The model predicted the same trend of the effect of difference in the CTEs between

mortar and aggregate as the experimental results. In addition, the model was able to predict the effect of air entrainment on reducing damage.

The model results and findings from the literature lead to the following recommendations regarding the concrete characteristics:

- The use of air-entrained concrete (positive CTE for mortar) is important in order to enhance the resistance to damage.
- Reducing the difference in CTEs between mortar and aggregate is essential in order to reduce damage. It is recommended that the difference in coefficient of thermal expansion values between aggregate and mortar should not exceed $(5-6)\times10^{-6}°C^{-1}$.
- ACI code recommend that aggregates should have a low CTE and compatible with the mortar to reduce damage associated with the tendency of volume change of aggregate and mortar. But in industry the mortar CTE value is between $(15-18)\times10^{-6}°C^{-1}$ and the aggregate CTE should be compatible with the mortar so gravel aggregates with CTE = $(10-12)\times10^{-6}°C^{-1}$ should be used.
- It is recommended to use fly ash, slag cement, and silica fume to increase durability and reduce permeability of concrete. The use of fly ash in concrete mixture reduces the potential of thermal cracking.
- Permeability for primary containment concrete in LNG tanks should not be higher than 10^{-18} m^2 .

- The use of rounded aggregates (less angular aggregates) reduces internal stresses and the potential for damage.
- Rounded lightweight aggregates are recommended for concrete used in LNG storage because it has lower permeability than normal aggregates.
- The w/c is suggested to be less than 0.45 in order to produce suitable pore structure and reduce expansion of moist concrete at transition temperature between -20 ^{o}C - -60 ^{o}C. If the w/c ration is high then the hydration rate will be high causing and produce coarse pores to form, which are not desirable.

6.2 Recommendations

The model and analyses presented in this thesis focused on comparative analysis of the performance of concrete mixtures under cryogenic temperatures. It is recommended to perform similar analysis but with different temperature gradients. Also, it is recommended to compare the results with the experimental measurements that are being conducted with the research team in College Station and Qatar.

It is also recommended to do finite element analysis of a concrete storage tank to simulate the effects of different designs and materials on potential damage.

REFERENCES

ABAQUS version 6.8.3, (2008), (computer software), Hibbitt, Karlsson and Sorensen, Providence, RI, USA.

Abu Al-Rub, R. K., and Kim, S. M. (2010). "Computational applications of a coupled plasticity-damage constitutive model for simulating plain concrete fracture." *Engineering Fracture Mechanics*, 77(10), 1577-1603.

American Concrete Institute (ACI) Committee. (2010). "Code requirements for design and construction of concrete structures for the containment of refrigerated gases (ACI 376-10) and commentary." *ACI 376*, Farmington Hills, MI, USA.

Callan, E. J. (1952). "Thermal expansion of aggregates and concrete durability." *ACI Journal Proceedings*, 48(2), 485-504.

Cicekli, U., Voyiadjis, G. Z., and Abu Al-Rub, R. K. (2007). "A plasticity and anisotropic damage model for plain concrete." *International Journal of Plasticity*, 23(10-11), 1874-1900.

Cohen, M. D., Zhou, Y., and Dolch, W. L. (1992). "Non-air-entrained high-strength concrete - is it frost resistant?." *ACI Materials Journal*, 89(2), 406-415.

Du, C. B., and Sun, L. G. (2007). "Numerical simulation of aggregate shapes of two-dimensional concrete and its application." *Journal of Aerospace Engineering*, 20(3), 172-178.

Du, X. L., Jin, L., and Ma, G. W. (2013). "Macroscopic effective mechanical properties of porous dry concrete." *Cement and Concrete Research*, 44, 87-96.

Hillerborg, A., Modeer, M., and Petersson, P., -E. (1976). "Analysis of crack formation and crack growth in concrete by means of fracture mechanics and finite elements." *Cement and Concrete Research*, 6(6), 773-781.

Inada, Y., Kinoshital, N., Ebisawa, A., and Gomi, S. (1997). "Strength and deformation characteristics of rocks after undergoing thermal hysteresis of high and low temperatures." *International Journal of Rock Mechanics and Mining Sciences*, 34(3-4), 1-14.

Kachanov, L. M. (1958). "On the creep fracture time." *Izvestiya Akademii Nauk SSSR. Otdelenie Tekhnicheskikh Nauk*, 8, 26-31.

Kogbara, R. B., Iyengar, S. R., Grasley, Z. C., Masad, E. A., and Zollinger, D. G. (2013). "A review of concrete properties at cryogenic temperatures: towards direct LNG containment." *Construction and Building Materials*, 47, 760-770.

Krstulovic-Opara, N. (2007). "Liquefied, natural gas storage: material behavior of concrete at cryogenic temperatures." *ACI Materials Journal*, 104(3), 297-306.

Lee, G. C., Shih, T. S., and Chang, K. C. (1988). "Mechanical properties of high-strength concrete at low temperature." *Journal of Cold Regions Engineering*, 2(4), 169-178.

Lee, J. H., and Fenves, G. L. (1998). "Plastic-damage model for cyclic loading of concrete structures." *Journal of Engineering Mechanics*, 124(8), 892-900.

Lemaitre, J., and Chaboche, J. L. (1978). "Phenomenological approach of damage rupture." *Journal of Applied Mechanics*, 2(3), 317-365.

Lubliner, J., Oliver, J., Oller, S., and Onate, E. (1989). "A plastic-damage model for concrete." *International Journal of Solids and Structures*, 25(3), 299-326.

Lukefahr, E., Du, L. (2010). "Coefficients of thermal expansion of concrete with different coarse aggregates - Texas data." *Journal of Testing and Evaluation*, 38(6), 1-8.

Marshall, A. L. (1982). "Cryogenic concrete." *Cryogenics*, 22(11), 555-565.

Miura, T. (1989). "The properties of concrete at very low temperatures." *Materials and Structures*, 22, 243-254.

Mukhopadhyay, A. K., and Zollinger, D. G. (2009). "Development of dilatometer test method to measure coefficient of thermal expansion of aggregates." *Journal of Materials of Civil Engineering*, 21(12), 781-788.

Philleo, R. E. (1986). Freezing and thawing resistance of high-strength concrete. Transportation Research Board, National Cooperative Highway Research Program, Washington, D.C, USA.

Prakash, A., Anandavalli, N., Madheswaran, C. K., Rajasankar, J., and Lakshmanan, N. (2011). "Three dimensional FE model of stud connected steel-concrete composite girders subjected to monotonic loading." *International Journal of Mechanics and Applications*, 1(1), 1-11.

Rahman, S., and Grasley, Z. C. (2013). "A Poromechanical model of freezing concrete to elucidate damage mechanisms associated with substandard aggregates." *Cement and Concrete Research*, in press.

Rostasy, F. S., Schneider, U., and Wiedemann, G. (1979). "Behavior of mortar and concrete at extremely low-temperatures." *Cement and Concrete Research*, 9(3), 365-376.

Taqieddin, Z. N. (2008). "Elasto-plastic and damage modeling of reinforced concrete," thesis, presented to Louisiana State University at Louisiana, in partial fulfillment of the requirements for the degree of Doctor of Philosophy.

The International Group of Liquefied Natural Gas Importers (GIIGNL). (2009). "Managing LNG risks - containment." *Rep. No 2*, The GIIGNL Technical Study Group, Paris, France.

van Breugel, K. (1982). "A designer's perspective on cryogenic storage-systems for liquefied industrial gases." *Cryogenics*, 22(7), 331-334.

Verbeck, G., and Landgren, R. (1960). "Influence of physical characteristics of aggregates on frost resistance of concrete." *Research Department Bulletin 126*, *PCA*, 60, 1063-1079.

Wang, Z. M., Kwan, A. K. H., and Chan, H. C. (1999). "Mesoscopic study of concrete I: generation of random aggregate structure and finite element mesh." *Computers and Structures*, 70(5), 533-544.

Wittmann, F. H. (1987). "Structure of concrete and crack formation." Fracture of non-metallic materials, K. P. Hermann and L.H. Larsson, eds., Springer Media B.V, Houten, AK, Netherlands, 309-340.

Yang, C. C., Lin, Y. Y., and Huang, R. (1996). "Elastic modulus of concrete affected by elastic moduli of mortar and artificial aggregate." *Journal of Marine Science and Technology*, 4(1), 43-48.

Yazdani, S., and Schreyer, H. L. (1990). "Combined plasticity and damage mechanics model for plain concrete." *Journal of Engineering Mechanics*, 116(7), 1435-1450.

Zheng, J. J., Li, C. Q., and Zhou, X. Z. (2005). "Thickness of interfacial transition zone and cement content profiles around aggregates." *Magazine of Concrete Research*, 57(7), 397-406.